ABSTRACT

Title of Dissertation: NANOSCALE LIGHT-MATTER INTERACTIONS: FUNDAMENTALS AND APPLICATIONS

Shangjie Yu, Doctor of Philosophy, 2018

Dissertation directed by: Professor, Min Ouyang

Department of Physics

Novel phenomena and promising applications have been emerging from nanoscience and nanotechnology research over recent decades. Particularly, people pursue a better understanding of how light and matter interact with each other at the nanoscale. This dissertation will present our work on the relevant topics, including ultrafast optical generation and manipulation of nanoscale phonons, metamaterials for thermal management, and cooperative chirality in inorganic nano-systems.

Through an acoustically mismatched nanoscale interface, interfacial phonon coupling may lead to a coherently modulated phonon spectrum, which however has been less studied. We have demonstrated unambiguous experimental evidences of coherent interfacial phonon coupling between the core and shell constituents by employing a well-designed nanoscale core-shell structure with a precisely tunable interface as a model system. Furthermore, the observed phonon modes can be selectively tailored in

a highly controllable manner by different ultrafast pulse control schemes. This study represents an important step towards nanoscale phonon engineering with rationally tailored nanostructures as building blocks.

Metamaterials, which are artificially patterned micro/nano-structures, are studied for thermal management. For this purpose, we propose patterned arrays in different forms, including micropillar arrays and fiber arrays. We have discovered the structural dependence of the arrays' characteristic resonance and emission properties, and how the properties are impacted in imperfect patterns which are common in real life. This study provides new perspectives on metamaterials for thermal management and the textile industry.

Lastly, chiral light-matter interaction is studied in a novel type of inorganic nanocrystals, consisting of both crystallographic and geometric chirality. We build up a general model for simulating electromagnetic response of chiral objects and extract the materials parameters from experimental data of the achiral-shape nanocrystals. By simulating nanocrystal of different geometries and comparing with experimental circular dichroism spectra, the unique spectral features from the nanocrystals' intrinsic crystallographic chirality, geometric chirality and their interplay are identified. Besides, an excellent agreement is achieved between the simulation and the experiment. This result opens up the opportunities for new chiroptical devices and chiral discrimination technology.

NANOSCALE LIGHT-MATTER INTERACTIONS:

FUNDAMENTALS AND APPLICATIONS

by

Shangjie Yu

Dissertation submitted to the Faculty of the Graduate School of the
University of Maryland, College Park, in partial fulfillment
of the requirements for the degree of
Doctor of Philosophy
2018

Advisory Committee:
Professor Jeremy Munday, Chair/Academic Advisor
Professor Min Ouyang, Co-Chair/Ph.D. Advisor
Professor Raymond Phaneuf
Professor Christopher Davis
Professor YuHuang Wang, Dean's Representative

Acknowledgements

I cannot come to the final stage of my graduate years at the University of Maryland without the support of many people. I would like to thank all of them from the bottom of my heart.

First, I'd like to thank my advisor and mentor Prof. Min Ouyang. He provides challenging and rewarding research opportunities and supports me with insightful guidance and constructive criticism. He sets a high standard and tries everything to help me develop the research and grow up as a critical thinker and a solid researcher. His strong dedication to science inspires me and helps me gain a bigger picture on scientific research. I also appreciate the tremendous support from the members of the Ouyang group: Dr. Geng Li, Dr. Peng-peng Wang, Huayu Zhang, Hanyu Liu, Nat Steinsultz, Dr. Jianxiao Gong, Dr. Lin Weng and Dr. Yanjie He. We have different backgrounds (physics, chemistry and engineering) and skill sets but come together as a great interdisciplinary team - it is really enjoyable to be one of them.

I'd like to thank Prof. YuHuang Wang for his incredible support and guidance in the Meta-Cooling Textile project. I'd also like to thank Prof. Liangbing Hu, Prof. Bao Yang and the other members of the project team, Dr. Xu Zhang, Dr. Beibei Xu, Dr. Kun Fu, Dr. Zhiwei Peng, Dr. Yongxin Wang, Dr. Min Li and Zhi Yang, for their help and advice for the program.

I’d like to thank Prof. Jeremy Munday for his long support as my academic advisor. I’d also like to thank other committee members of my defense, Prof. Raymond Phaneuf and Prof. Christopher Davis for invaluable advice.

I’d like to thank all other people for all the help: Doug Bensen and Brian Straughn for the technical support, Fadel Muci and Caroline McCue for 3D printing, Greg Jenkins and Stephan Forden for metal sputtering coating, Dr. Sz-Chian Liou and Dr. Wen-An Chiou for the SEM imaging, Mary Sutton, Margaret Lukomska, Melanie Prange, Emily Irwin and Pauline Rirksopa for the administrative support, CNAM graduates and postdocs for the intriguing talks and many others.

Finally, I cannot express enough gratitude to my partner Janet and my parents. They give me unconditional love and support and ignite my courage and confidence to overcome all the difficulties.

Table of Contents

List of Tables

List of Figures

List of Abbreviations

3D	Three Dimensional
MIR	Mid-InfraRed
FEM	Finite Element Method
FDTD	Finite-Difference Time-Domain
CD	Circular Dichroism
FT	Fourier Transform
NP	Nano-Particle
DLW	Direct Laser Writing
CNT	Carbon NanoTube
SEM	Scanning Electron Microscopy
TEM	Transmission Electron Microscopy

Chapter 1: Introduction

1.1 Overview

Although nanoscale structures, like DNA, have existed in nature for a long time, research on nanoscience and nanotechnology started only in the late 20th century, mostly benefiting from the instrumentation inventions like electron microscopes[1], scanning tunneling microscopes[2] and atomic force microscopes[3], and the material discoveries such as Fullerenes[4] and carbon nanotubes[5]. Over the past decades, nanoscience as an emerging and broad science, has been booming and involved interdisciplinary efforts from physicists, chemists, biologists, and engineers working on both fundamentally new phenomena and potentially disruptive technologies.

Light-matter interaction at the nanoscale is a branch of nanoscience where people have great interest[6]. The community are motivated to explore exotic phenomena from strong interactions confined at subwavelength scales, new nano-optical methods as a unique and sensitive probe to study nanoscale interfaces or materials, and promising applications for ultracompact optical devices (sources/sensors/processors) and clean energy (solar cells/radiative coolers). The progress has benefited from the development of instrumentation (advanced sources/microscopes/detectors), nanomaterial fabrication, and computation techniques and capability. But in many topics, it remains unclear how light and matter interact with each other at the nanoscale, because of the quantum nature of the interacting particles (like photons and electrons), the complication of condensed matter systems, and the technical challenges to measure the

interaction. Practically, it needs more efforts in gaining a good understanding of nanomaterials and the optical physics involved through rationally designed material preparation and optical studies. This dissertation will present our works on understanding light-matter interactions at extremely fine spatial scales, including ultrafast optical generation and manipulation of nanoscale phonons, metamaterials for thermal management and cooperative chirality in inorganic nano-systems. These are three great examples how we can either control the matter state by optical methods (nanoscale phonon mode manipulation in Chapter 3) or control local light by nanomaterial engineering (interfacial phonon coupling in Chapter 2, metamaterials for thermal management in Chapter 4, chiral optical interaction in Chapter 5). These studies may broaden and enrich ever-growing research areas in nano-optics, plasmonics and condensed matter physics, and may also potentially impact our future life by enabling high-speed signal processing and miniature devices[7-9].

1.1.1 Ultrafast optical generation and manipulation of nanoscale phonons

Phonons play a key role in almost every physical process in condensed matter, including for example decoherence of quantum states, electronic transport and thermal management[10,11]. The interplay between electrons and phonons in a condensed matter system determines many of matters' intrinsic physical properties including, for example, the nature of superconductivity, dephasing of electronic quantum states, electric and heat transport, and metal-insulator transition[10-14]. Precise engineering of the phonon spectrum or phonon interaction with other fundamental quantum particles

by materials design is therefore essential for an in-depth understanding of thermal, electronic, and optical phenomena as well as new technology breakthroughs governed by fundamental physical laws. Particularly, when the size of matter is smaller than the mean free path of phonons (for example in nanoparticles or nanowires), spatial confinement can create strong modification of phononic characteristics (e.g., phonon dispersion and group velocity), thus providing a unique way to engineer the phonon spectrum[15-29]. Furthermore, when phonons propagate through two different constituents, their mismatched interface can coherently modulate the phonon spectrum by redistribution of lattice vibration displacement[30-33]. For example, it has been theoretically predicted that phonon population in thin films or nanowires embedded into an acoustically softer material can be depleted with suppressed scattering rate[34]. However, a thorough understanding and precise control of such nanoscale interfacial phonon coupling has been lacking. Importantly, recent advances in the preparation of nanoscale materials enable precise control of size, composition, crystallinity and hetero-structure formation[35-39], thus opening the opportunity to sensitively monitor electron and phonon coupling processes through the interplay of confined size, fundamental length scales and interfaces.

Furthermore, controlling phonons and associated dynamics can be crucial to elucidate many underlying physical mechanisms/processes as well as to optimize device performance and create novel device concepts[23,29,40-43]. Indeed, much recent progress has been achieved towards phononic control, mainly by materials design. For example, a few state-of-the-art mesoscopic phononic devices and complex phononic structures, including phononic resonators[44,45] and thermal rectifiers[46], have drawn substantial

attentions due to their unique capability to guide phonon propagation. Particularly, by taking advantage of size confinement and shape control, phononic characteristics of one material (e.g. phonon dispersion and group velocity) can be dramatically modified at the nanoscale, thus offering a novel way to finely engineer phonon spectra that cannot be available in their bulk counterparts. This includes appearance of discrete quantized acoustic phonon modes in a nanostructure due to breaking of the translational invariance (e.g., different orders of symmetric breathing phonon modes have been extensively observed for spherical nanoparticles), whose multimodal frequencies have shown distinct dependence on their size and shape[22,26,47]. When combining with recent materials development at the nanoscale, phononic modulation through intimate interfacial coupling in a hybrid nanostructure has been achieved with potential to offer a precise control of phonon engineering in the spatial domain[30,31,48]. Nevertheless, phonon is also inherently dynamic in the time domain, and phononic excitation can be achieved on femtosecond (fs) or picosecond (ps) time scales through different mechanisms[22,47], thus providing a unique way to manipulate phonon vibrations in a coherent manner as long as the process is much faster than the characteristic quantum decoherence time. So far, while the evidence of the suppression of the fundamental breathing mode of spherical nanoparticles was observed in an ultrafast optical study[20], systematic investigation for understanding the in-depth mechanisms or more advanced phonon control has been absent.

1.1.2 Metamaterials for thermal management

Metamaterials are artificially patterned micro/nano-structures and exhibit unique features or outstanding performance, which are hardly possible to obtain in conventional materials[49,50]. Their characteristics are primarily based on their physical patterned structures, instead of just bulk material properties from their crystal structures or chemical composition. Owing to their extraordinary properties, the research on metamaterials has been vastly growing and great examples are flat metasurfaces for ultracompact visible-range lens[51], mechanical metamaterials with negative compressibility transitions[52], and invisibility cloaks[53]. There have been mechanical, acoustic, electromagnetic, and other types of metamaterials, depending on the physical nature of their working mechanism. In this dissertation, we will focus on electromagnetic metamaterials in the mid-infrared (MIR) range, where lies the thermal emission band under most of the real-life temperature conditions.

Thermal radiation is one of the fundamental heat transfer processes and has been growingly significant in researching and improving thermal management in various systems. In the last decade, there have been tremendous and ever-increasing efforts into thermal management with micro/nano-optical structures dedicated to the MIR range[54-58]. Metamaterials have been applied to obtain specific IR radiation characteristics, and thus achieve desired thermal cooling capability. Besides, a metamaterial MIR device can achieve a tunable emission by engineering the characteristic thermal band of the structure[59,60]. This functionality can potentially provide a dynamic thermal management responsive to the actual need.

1.1.3 Chiroptics in nanomaterials

Chirality is a physical property that an object cannot be superimposed by its mirror images, and is manifest in various natural forms, such as molecules, animal organisms and spiral nebula. It has fundamental importance and potential industrial applications. For example, studies on chiral interactions between molecules and biochemical species not only shed new light on biology and physiology, but also pave the way for the biomedical and pharmaceutical industries. Recently chiral inorganic nanostructures have been intensively studied and have shown unique physical properties, among which optical properties are particularly interesting[61-64].

Chiroptical phenomena, which happens when materials with different handedness interact with polarized light, are very attractive to people, especially at the nanoscale[65-67]. The differential absorption of left and right-handed circularly polarized light, defined as circular dichroism (CD), is a widely applied method to characterize the chiroptical activity[68]. People have tried different ways to enhance or control the chiroptical phenomena from the materials, such as molecular functionalization of achiral nanoparticles (NPs)[69-74], shaping materials into chiral forms[75-78] or attaching metal NPs onto helical scaffolds[79-83]. Most of these cases take advantage of the plasmonic effect that originates from the localized surface plasmon resonance of metal nanostructures[77,84-88]. Others also show mirror image CD features induced by distorted shells or chiral ligand on the surface of colloidal semiconductor quantum dots[62,89].

In inorganic systems, the crystal lattice can be a great intrinsic source of chirality, and there is an ever-increasing interest from both academia and industry in fabricating atomically chiral NPs, which should have considerable chiroptical response compared

to small chiral molecules or chiral geometries with an achiral lattice. We have known there are various kinds of inorganic chiral crystals available such as SiO_2, $AgGaS_2$ and TeO_2. The smallest chiral units (atoms or molecules) can be further assembled into mesoscopic particles of either achiral or chiral shapes. In this manner, chiroptical responses can be tuned by either changing chiral units (materials) or shaping intrinsically chiral nanocrystals. A recent study has demonstrated the enantioselective synthesis of α-HgS chiral nanocrystals induced by chiral surfactant molecules[90], which excluded the surface effects – either the electronic induction by the capping ligands or the surface distortion. Another work shows the intrinsic chirality of semiconductor quantum dots by the enantioselective phase transfer technique[91]. But both of them only show achiral shapes without extending to mesoscopically chiral forms. People have also tried to make nano/micro-scale chiral structures with small chiral units by supramolecular assembly[92], or top-down fabricated chiral meta-structures[67,93]. However, in inorganic NPs, two levels of chirality, from crystal and geometry, have not been clearly demonstrated. In a recent paper[94], tellurium nanocrystals of lattice and shape chirality are reported. Although they claim shape chirality is much more significant than lattice chirality, only the shape chirality was clearly shown in either experimental study or theoretical calculation of the chiroptical response. For example, they only show a geometry dependent CD activity in the experiment, and their modeling does not involve any chiral medium parameter. Thus, the result cannot distinguish them from previous studies on chiroptical phenomena merely induced by the mesoscopic shape. In our work, we unambiguously demonstrate chirality of a

mesoscopic structure at both crystal and shape level at the same time, which will be discussed in Chapter 5.

1.2 Experimental methods

In this section, we will introduce ultrafast optical spectroscopy for the experimental study of nanoscale phonons in Chapter 2 and 3, and direct laser writing (DLW) 3D printing for metamaterials fabrication in Chapter 4.

1.2.1 Ultrafast optical spectroscopy

Ultrafast optical spectroscopy uses ultrashort pulse lasers for the studies of physical dynamics on the ultrashort time scales (ranging from attoseconds to nanoseconds)[95]. This experimental method has been widely-employed in different scientific areas, because there are various physical, chemical and biological processes occur on the extremely short time scales like quantum state evolution[96,97], photochemical reactions[98], and molecular energy transfer[99,100]. This is a powerful experimental technique to study the light-matter interactions since the high peak intensity of the ultrafast pulses can efficiently pump the sample to excited states and the short pulse width helps to understand how matter states evolve under the optical perturbation in a short time scale.

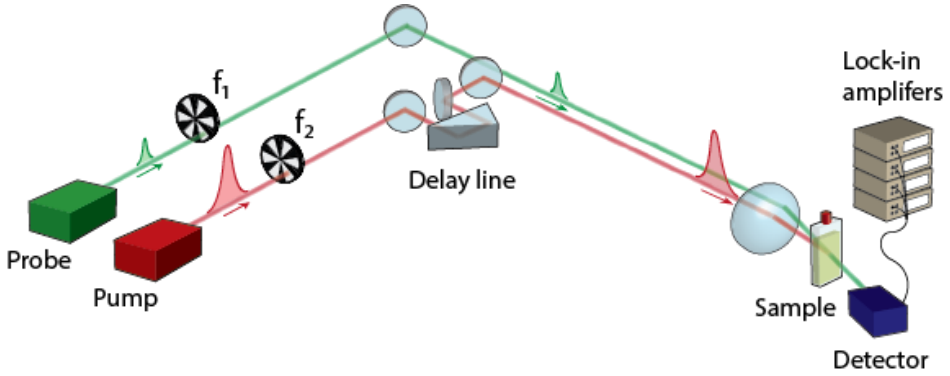

Figure 1. Schematic of the experimental setup of the pump-probe measurement. The beams modulated by the optical choppers can be detected by lock-in amplifier. The delay line produces a time delay between pump and probe pulses.

For ultrafast optical studies, usually a sequence of ultrashort light pulses are applied to initiate a process and measure the following dynamics. A basic form of ultrafast optical spectroscopy is pump-probe spectroscopy. In a typical pump-probe measurement, two optical beams (containing two synchronized series of ultrashort pulses) are used, shown in Figure 1. One is a pump beam (with relatively strong-intensity pulses) used to initialize the excited state by sample excitation. And the other is a probe beam (with relatively low-intensity pulses) used to detect evolution of the excited state by measuring the dynamical optical property changes of the sample, like transmission or reflection. Since pump and probe pulses are electrically synchronized, by finely scanning the time interval between them, the dynamics of the excited state of interest can be monitored.

In our study, we employ ultrafast optical spectroscopy to generate and measure the ultrafast phonon modes at the nanoscale. We further extend pump-probe to pump-

control(s)-probe for ultrafast optical manipulation. The details are discussed in Chapter 2 and 3.

1.2.2 Direct laser writing 3D printing

Photolithography is a well-developed micro/nano-fabrication technique by which photoresists are patterned by optical illumination at a specific wavelength to which the photoresists are sensitive. However, it is not easy to create an arbitrary three-dimensional (3D) structure with the standard photolithography since it can barely cure photoresists at a very local volume. To resolve this, 3D direct laser writing (DLW) is developed based on two-photon absorption[101-103]. Two-photon absorption is a second-order nonlinear optical process by absorbing two incident photons and radiating a single photon of a doubled frequency. In 3D DLW, a laser beam is tightly focused to a diffraction-limited spot within the photoresist film. Due to the nonlinear nature, two-photon absorption only occur at the center of focal spot and effectively exposed volume can be restricted to the focal region leading to a volume element, the "voxel"[101]. By proper choice of the photoresist (transparent to the pump light but sensitive to double-frequency light) and careful scanning the focal spot, 3D laser printing can be achieved. Owing to the weak nonlinear conversion and confined spot, a printing resolution much smaller than the pump light wavelength can be achieved. For example, with a 780nm pump laser, lateral linewidths below 100 nm are achieved[101]. The nonlinear conversion requires very high optical intensity, and thus, pulsed laser sources are preferred for the

purpose. They can deliver high-intensity pulses while maintaining a relatively low average power on the photoresists.

In our study, we employ 3D DLW on a commercial printer for sample fabrication. The details are discussed in Chapter 4.

1.3 Computational methods

In this section, we will introduce finite element method (FEM) for the computation study in Chapter 2, 3 and 5, and finite-difference time-domain (FDTD) for metamaterial design in Chapter 4.

People have developed elegant electromagnetic theories since James C. Maxell proposed the early form of governing equations of classical electromagnetism, which are afterwards named Maxwell's equations[104]. However, it is generally difficult to analytically solve Maxwell's equations for an arbitrarily shaped object with complex material components, in which case the system cannot simplified by symmetry. Instead, it is much easier to set up the object numerically and simulate its electromagnetic response. There are a few computational methods with their own advantages to simulate electromagnetic response, such as finite element method (FEM), finite-difference time-domain (FDTD), discrete-dipole approximation and boundary element methods. We have employed FEM and FDTD in our research and will introduce them in the following part. However, we do not intend to provide a very detailed review on the methods and there is dedicated literature for more specific discussion on these methods[105-108].

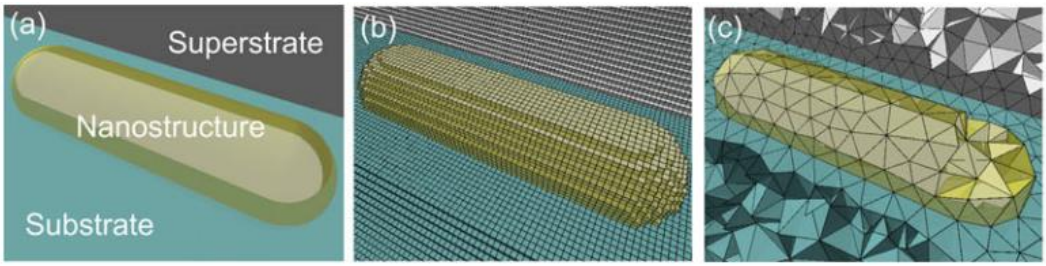

Figure 2. Spatial discretization for computational modeling of a nanostructure. (a) Schematic of the nanostructure sandwiched between a substrate. (b) FDTD with a Cartesian discretization. (c) FEM with a tetrahedral discretization. The figure is from the paper[108].

FEM is a general numerical method to solve partial differential equations. Since the physics for space- and time-dependent problems can often be described in terms of partial differential equations, FEM has been widely applied in many areas such as structural analysis, heat transfer, fluid flow and electromagnetism. FEM-based computation involves several essential steps[109]: discretization of the computational domain, selection of the interpolating functions, derivation and assembly of characteristic matrices and vectors and solving the matrix problem **Ax** = **b**. For the discretization, FEM uses an adaptive tetrahedral mesh for the FEM simulation (see Figure 2c), which allows for a more accurate computation of curved surfaces or other complicated geometries. This offers FEM a huge advantage over some other methods (like FDTD), which cannot apply an adaptive tetrahedral mesh and may introduce large numerical error in simulating complex structures. As introduced above, it can solve different types of partial differential equations, enabling multi-physics simulation. In our research, we use the commercial FEM package COMSOL for our solid structure and electromagnetic simulation. FEM simulation often requires relatively large computational resources, mostly central processing unit (CPU) and memory, but it is

not our concern since the models involved in our work do not involve a very large number of degrees of freedom (<= 1 million), which can be handled by a dual-CPU workstation.

	Advantage	Disadvantage
FDTD	Broadband response in the frequency domain by a single simulation	1. Regular Cartesian mesh 2. Only applied to electromagnetic problems
FEM	1. Non-regular tetrahedral adaptive mesh 2. Able to couple with multi-physics	Complicated algorithms

Table 1. Comparison between FDTD and FEM methods

The other method we would like to introduce is FDTD that simulates electromagnetic response in the time domain. FDTD is first proposed by Yee dedicated to solving Maxwell's equations in isotropic media[110] and have developed over the past decades[106]. Basically, a FDTD algorithm approximates the differential form of the time-dependent Maxwell's equations into the difference form by discretizing space and time into a lattice with a spatial step *a* and temporal step *t*. Then it sets up the sources and boundary conditions, and it can solve the discretized fields in space and time step by step. The principle makes it relatively easy to implement FDTD but limits the spatial grid to be Cartesian (see Figure 2b). Thus, it is difficult to accurately simulate complicated boundary configurations with FDTD. Although FDTD is a time-domain based method, a frequency domain spectrum can be easily calculated by Fourier transform (FT) of a single time-domain result, rather than multiple single-frequency simulations in the frequency domain. This means it can be very fast for small scale configurations. In our

research, we use the commercial FDTD package Lumerical for our electromagnetic simulation. In Lumerical, a time-domain pulse is usually set as excitation source and the spectral bandwidth of interest can be conveniently defined by the pulse width.

Figure 2 shows the comparison of spatial discretization for modeling a nanostructure, and the key difference is Cartesian discretization (FDTD) and tetrahedral discretization (FEM). Table 1 is a brief comparison between FDTD and FEM. This comparison table outlines the key points that concern our research instead of presenting a very comprehensive comparison, because the advantage/disadvantage of a computation method largely depends on the type of a specific problem. For example, neither FDTD nor FEM is ideal for nano-optical scattering problems[108].

1.4 Overall structure

The rest of the dissertation is organized as follows.

Chapter 2 presents our work on acoustic phonons and electron–phonon coupling in nano-heterostructures (published[48]). We simulate the fundamental breathing modes in the bimetallic heterostructures and reveal that the interfacial coupling leads to the unique features in the evolution of phonon spectra. Based on the simulation, we experimentally demonstrate the ultrafast optical generation of coherent phonons and study interfacial phonon interaction at the nanoscale. Electron-phonon coupling is also discussed in a complex core-shell nanostructure.

Chapter 3 proposes an all-optical method to coherently manipulate acoustic phonons in nanoscale samples (published[111]). We first examine the feasibility of different coherent manipulation schemes with FEM simulation and demonstrate that sequential application of impulsive excitations of acoustic phonons can be used to control phonon modes in a coherent and highly selective manner. Then we experimentally demonstrate clear modulation of the fundamental phonon modes in a single-pulse control scheme and more selective control of different higher-order phonon modes in a dual-pulse control scheme, agreeing well with the FEM simulations.

Chapter 4 introduces applications of metamaterials to thermal management, particularly in the context of textiles and passive cooling of a human body. We consider the structural dependence of the mid-infrared (MIR) emission properties of simple micro-arrays computationally and experimentally. And we further study the emission properties of the patterned fiber arrays in a fabric yarn and the round-cross-section yarn arrays consisting of patterned fiber arrays. To obtain a more comprehensive understanding of the metamaterial-based textile in real life, imperfect arrays are also studied by introducing randomness into the structures.

Chapter 5 presents our work on cooperative chirality in an inorganic system incorporating crystallographic and geometric chirality (published[112]). In the beginning, a general model is introduced about the cooperative chirality originating from the chiral interaction at different levels in a hierarchical system. Meanwhile, our synthesis efforts on various α-HgS-based chiral nanomaterials will also be briefly discussed. Then we present the basic electromagnetic theory of chiral materials and show how to calculate

the response of a chiral object in the FEM package. Eventually we study the cooperative chirality in α-HgS nanoparticles by experimental CD spectroscopy and simulation.

Chapter 6 summarizes the dissertation and outlines some future research.

Chapter 2: Coherent phonon generation and interfacial phonon interaction at the nanoscale

2.1 Introduction

Precise engineering of phonon-phonon (ph-ph) and electron-phonon (e-ph) interactions by materials design is essential for an in-depth understanding of thermal, electrical and optical phenomena as well as new technology breakthroughs governed by fundamental physical laws. Due to their characteristic length scale, the ph-ph and e-ph interactions can be dramatically modified by nanoscale spatial confinement, thus opening up opportunities to finely maneuver underlying coupling processes through the interplay of confined size, fundamental length scale and interface. We have combined ultrafast optical spectroscopy with a series of well-designed nanoscale core-shell structures with precisely tunable interface to demonstrate for the first time unambiguous experimental evidences of coherent interfacial phonon coupling between the core and shell constituents. Such interfacially coupled phonons can be impulsively excited through the e-ph interaction, in which the critical e-ph coupling constant is further shown to be monotonically controlled by tuning the configuration and constituent of core-shell nanostructure. Precise tunability of elemental physics processes through nanoscale materials engineering should not only offer fundamental insights into different materials properties but also facilitate design of devices

possessing desirable functionality and property with rationally tailored nanostructures as building blocks.

2.2 Simulation of phonon modes

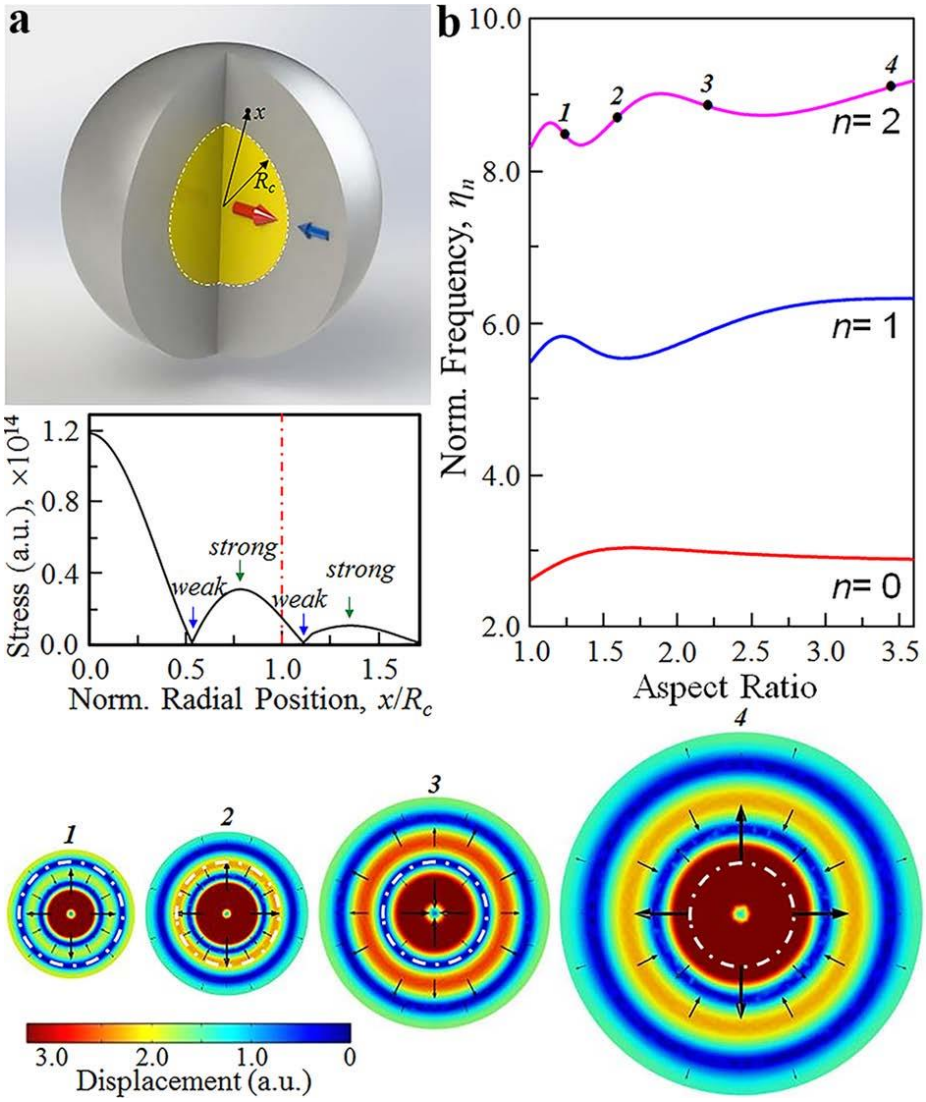

Figure 3. FEM computation of phonon modulation through acoustically mismatched interface in an Au-Ag core-shell nanostructure. (a) (Top) Schematic core-shell model with interface highlighted by a white dash-dot curve. Red and blue arrows represent lattice vibrations of the core and shell, respectively. The R_C represents the radius of the core, and x is the radial coordinate. (Bottom) Computed radial stress field distribution of the $n = 0$ phonon mode in a core-shell nanostructure consisting of 3.8 nm-diameter

Au core and six monolayers of Ag shell. The core-shell interfacial position is highlighted by a red dash-dot line. When the aspect ratio of a core-shell nanostructure is varied, its interface will evolve through weak and strong stress field. (b) (Top) Dependence of the computed η_n on the aspect ratio of an Au-Ag core-shell for the $n = 0$, 1 and 2 phonon modes. In this computation, the Au core size remains the same, while the Ag shell thickness is varied to tune its aspect ratio. For the $n = 2$ mode, four selected aspect ratios at the crossing points of 1, 2, 3 and 4 are highlighted to feature the oscillatory behavior of the η_2. (Bottom) Corresponding two-dimensional lattice displacement at the crossing points of 1, 2, 3 and 4. The white dash-dot circle represents the core-shell interface.

Figure 3a shows one schematic core-shell model with highlighting the role of the interface between two different nanoscale constituents. In particular, we have employed a complex concentric Au-Ag-Pt core-shell-shell system with precisely tailored structural parameters as a model system to explore nanoscale interfacial phonon modulation and its intrinsic e-ph coupling. The Au-Ag-Pt core-shell-shell is chosen based on the following considerations: (1) Au, Ag and Pt exhibit identical lattice structure (face-centered cubic) with similar lattice constants, which can significantly reduce structural mismatch during the growth[113]; (2) The acoustic impedance mismatch among these three elements can be up to 50%, which can strongly modulate acoustic phonon spectra and modify corresponding e-ph and ph-ph interactions within a heterostructure[114]; (3) while bulk Au and Ag possess a moderate difference in the e-ph coupling constant (*G*), the *G* value of bulk Pt is about two-orders of magnitude larger due to the very high density of electrons at the Fermi level (E_f) with almost full *d* bands[115,116]; and (4) Experimentally a universal synthetic strategy has been recently achieved to allow a uniform growth of the concentric core-shell nanostructures with precise control of the shell thickness at the monolayer level[25]. We would like to lay emphasis on the fact that even though there exist a few optical studies on acoustic

phonon features of bimetallic core-shell nanostructures (including various Au-Ag nanostructures)[117-121], none of the existing reports so far has provided explicit evidence of interfacial phonon coupling, and part of the reasons might be due to a lack of meticulous materials control as well as low-noise optical measurement that can allow to reveal features of higher order phonons. To that end, precise materials engineering should be a prerequisite for accurate tailoring of intrinsic physics property with unambiguous interpretation of experimental results.

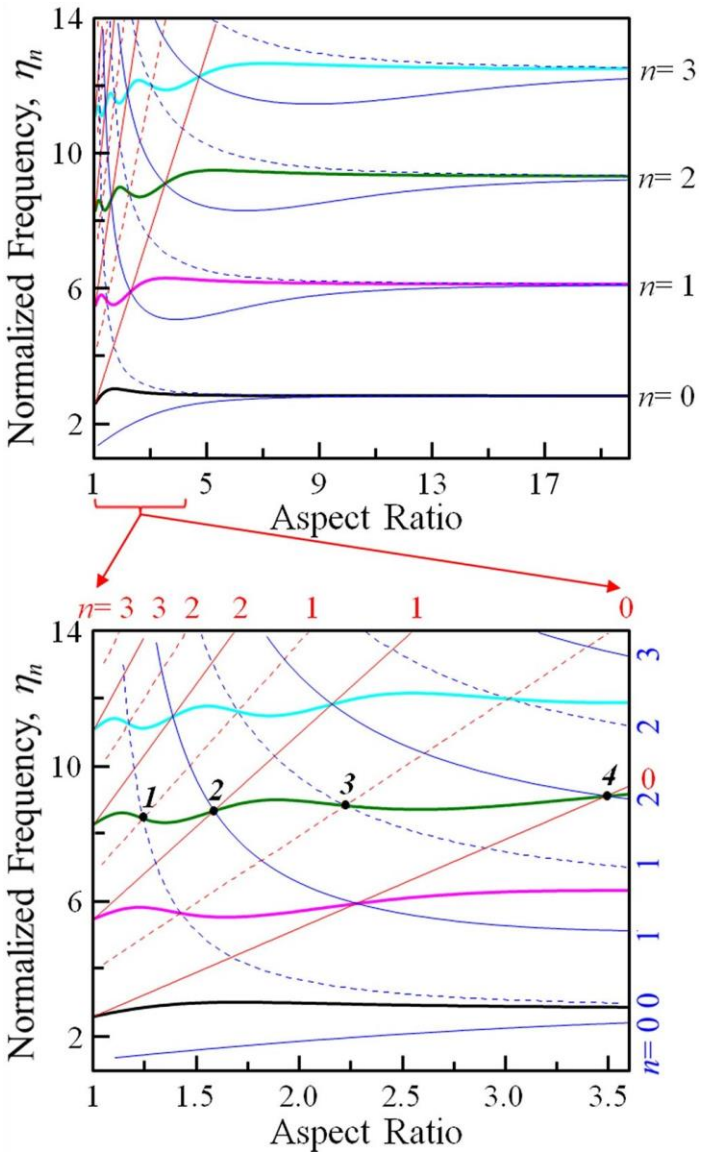

Figure 4. Dependence of normalized frequencies η_n of Au-Ag core-shell on its aspect ratio. The normalized frequencies, η_n of the nth-order radial modes of the Au-Ag core-shell nanoparticles (thick solid color curves: $n = 0$ (black), 1 (magenta), 2 (olive) and 3 (cyan)), solid Au nanoparticles with zero-stress boundary condition (thin red solid lines), solid Au nanoparticles with zero-displacement boundary condition (thin red dashed lines), Ag nanoshells with zero-stress boundary condition (thin blue solid curves), and Ag nanoshells with zero-displacement boundary condition (thin blue dashed curves).

Figure 3a shows an exemplary lattice stress field distribution in a core-shell nanostructure with highlighting the relative location of the interface. This plot is computed under excitation of the n=2 acoustic phonon mode of a core-shell structure consisting of 3.8nm-diameter Au core and six monolayer Ag shell by employing finite element method (FEM). Two local stress minima and maxima along the radial direction can be identified for the n=2 phonon mode, whose placements evolve with the composition and configuration of a core-shell structure. As a result, when the core-shell configuration is varied by for example increasing the shell thickness while maintaining constant core diameter (i.e., the core-shell interface remains the same), the stress minimum and maximum will evolve through its interface continuously, leading to weak and strong interfacial phonon coupling between the core and shell's acoustic phonons, respectively (see also Figure 4 and Figure 5). For example, the core nanoparticles can be fully engaged to the lattice vibration of the shell if the maximum stress occurs at the interface. The intriguing phonon coupling between the core and shell modes is thus expected depending on the stress field at the interface, which can result in novel phonon features absent in the single component plain solid nanoparticles or nanoshells on the disengaged core nanoparticles[122-124]. Figure 3b shows evolution of normalized phonon frequencies of n= 0 to 2 modes of the Au-Ag core-shell with its aspect ratio, which is defined as the ratio of its overall size (R_0) to the core size (R_c). The normalized frequency η_n of the nth-order phonon mode is defined as $\eta_n=(2\pi f_n R_0)/c_{l,shell}$, where f_n and $c_{l,shell}$ are the vibrational eigen-frequency and the longitudinal sound speed of the shell, respectively. One unique feature immediately arising in the computed phonon spectra is that for higher order nth phonon mode (n>1), the η_n manifests oscillatory

behavior when the aspect ratio is varied, that can be attributed to the radial evolution of the interfacial stress field by the lattice vibration, as depicted in the Figure 3b. Figure 3b also illustrates radial lattice displacement of the Au-Ag core-shell under excitation of n=2 phonon mode at the four different aspect ratios of 1.24, 1.58, 2.22 and 3.46, respectively. It can be seen that the points *1* and *3* possess zero lattice displacement at the interface, while the points *2* and *4* correspond to continuous interfacial lattice motion (see also Figure 5). Therefore, investigation of higher order (n>1) phonon modes as well as their dependence on the aspect ratio in a core-shell geometry should be critical in order to provide unambiguous evidence of interfacial phonon coupling, but typically requiring extreme detection sensitivity of phonons due to their weak vibration intensity. Correspondingly, this nanoscale interfacial engineering can thus offer an opportunity to tailor the phonon spectrum but requiring sophistic materials design to precisely tailor relative position of the core-shell interface in a desirable manner.

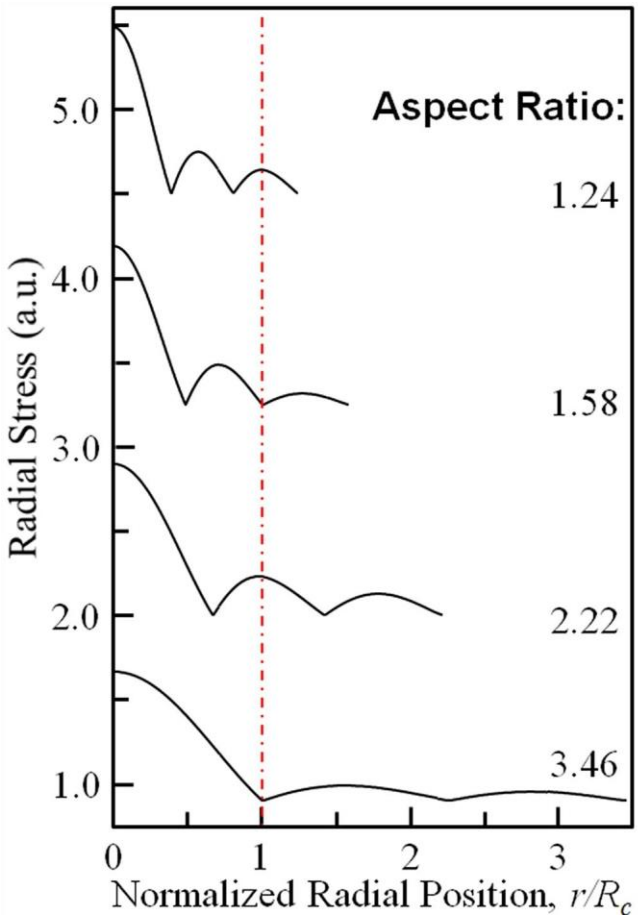

Figure 5. Computed stress field distribution along radial direction of the core-shell nanostructures for the n=2 phonon mode. The core-shell structures presented here correspond to the crossing points 1, 2, 3 and 4 in Figure 3b and Figure 4, in which the size of core remains the same (3.8 nm) while the shell thickness is varied for different aspect ratio. The curves are vertically shifted for clarity. The red dash-dot line highlights the interface position of the core-shell nanostructures.

2.3 Experiment

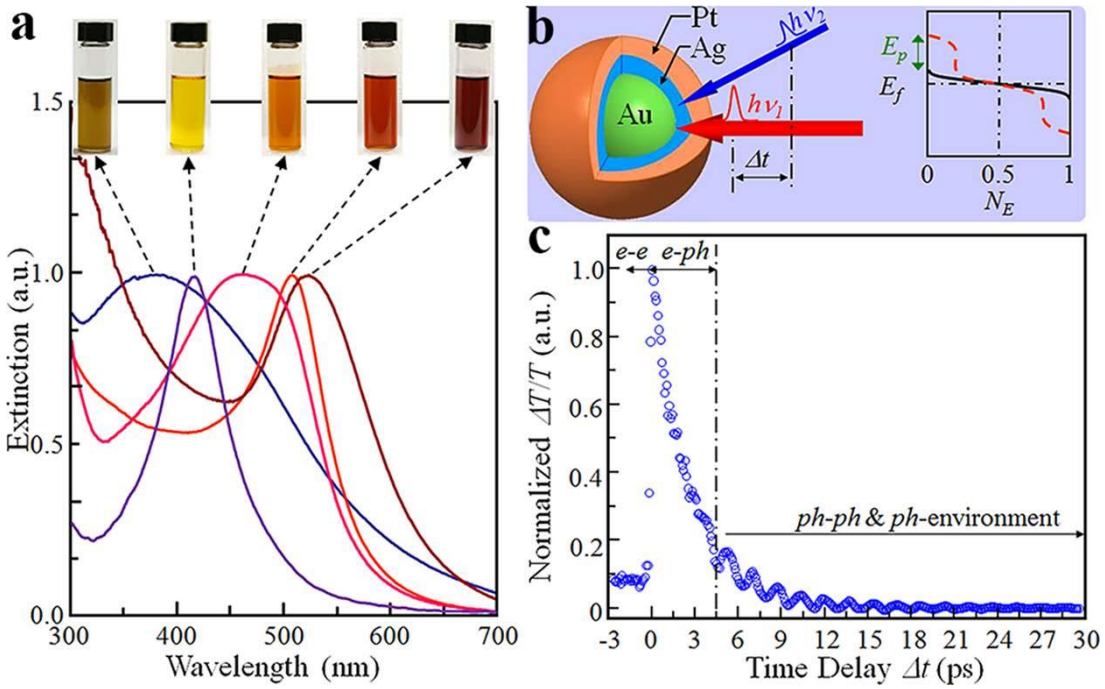

Figure 6. Static and time-resolved optical spectra of Au-Ag-Pt core-shell-shell nanostructures. (a) Evolution of optical spectroscopy of Au-Ag-Pt samples with same Au core size (3.8 ± 0.2 nm in diameter) but variation of Ag and Pt shells. Dark red for plain Au core nanoparticles; orange for one monolayer of Ag shell; pink for two monolayers of Ag shell; purple for six monolayers of Ag shell; blue for nine monolayers of Ag shell and one monolayer of Pt shell. The surface plasmon resonance peak intensity is normalized to the unit for comparing peak position. Such shell-dependent optical property of Au-Ag-Pt core-shell-shell can also be visually identified from corresponding solution color. (b) Schematics of pump-probe experiment with core-shell nanostructure. Right diagram shows equilibrium electron distribution of nanostructures (black line) and the perturbed one after absorption of pump pulse (E_p) (red dashed line). (c) A typical normalized experimental time-resolved spectrum showing the optical transmission change ($\Delta T/T$) as a function of time delay of the probe pulse (Δt_{probe}) in the Au core (3.8 nm)- Ag shell (6 monolayers). The data was recorded at laser energy density of 2.54×10^6 Jm^{-3}.

Recent advancement of bottom-up synthetic approaches has allowed precise engineering of various concentric core-shell nanostructures at the accuracy of a monolayer level (for example, layer-by-layer silver growth on top of gold

nanoparticles)[39], thus making such structure ideal for exploring coherent modulation of phonon spectra, as predicted in Figure 3. Figure 6a presents a layer-by-layer evolution of optical property of Au-Ag-Pt core-shell-shell nanostructures, highlighting precise monolayer control of shell components in our samples (see Figure 7). While the plain Au core nanoparticles show a clear surface plasmon resonance feature in the visible regime, a gradual blue shift of this optical resonant peak occurs upon the growth of Ag shell due to the synergistic effect, and the surface plasmon resonance feature of core-shell becomes dominantly contributed from the silver shell once the shell reaches six monolayers. Moreover, we observe that continual growth of outmost Pt shell can lead to even more dramatic effect on the overall optical property by showing considerable blue shift of the surface plasmon resonance energy with broader linewidth. To ensure sample quality in our measurement as well as to interpret our data unambiguously, we have also carried out TEM characterization after every ultrafast laser spectroscopy measurements. We confirm that under our experimental condition, we have not observed any sample change due to laser-induced annealing/alloying[117]. The high sample quality as well as precise monolayer tunability of structural configuration makes it feasible to explore interfacial coherent phonon coupling in a systematic manner.

To explore dynamic fundamental coupling interactions involving electron and phonon, we have employed femtosecond time-resolved spectroscopy with temporal resolution of ~70fs that can impulsively excite electron and phonon on a time scale shorter than the related energy redistribution (typically in the range of ps) and represents an ideal tool for direct time domain investigations of related elementary scattering

processes[17,22,23]. Figure 6b illustrates a schematic two-color time-resolved spectroscopy measurement with core-shell nanostructure, with a typical experimental trace of time-resolved optical transmission change ($\Delta T/T$) shown in Figure 6c. Because the size of the core-shell nanostructures is much smaller than the laser focus volume (50 μm in diameter), the excitation of the core-shell structures should be considered uniform in our experiment[42]. As shown in Figure 6c, the inter-correlated energy transfer processes with different scattering interactions can therefore be identified according to their characteristic time scales: For the short time delay (Δt_{probe} < 0.2ps), behavior of $\Delta T/T$ (i.e., a rapid increase of the signal) is mainly dominated by the electron-electron (e-e) scattering mechanism to equalize the temperature of the non-equilibrium conduction electrons after the pump excitation; this process is followed by a fast exponential decay (0.2 < Δt_{probe} < 5ps) that can be attributed to the energy exchange between electrons and phonons (lattice vibration) mainly through the e-ph coupling interaction with a certain decay constant; the impulsive excitation of phonon from the e-ph coupling thus contributes to a longer time scale decay characteristics (Δt_{probe} > 5ps) based on the ph-ph interaction as well as the energy dissipation from the nanostructures to the local environment.

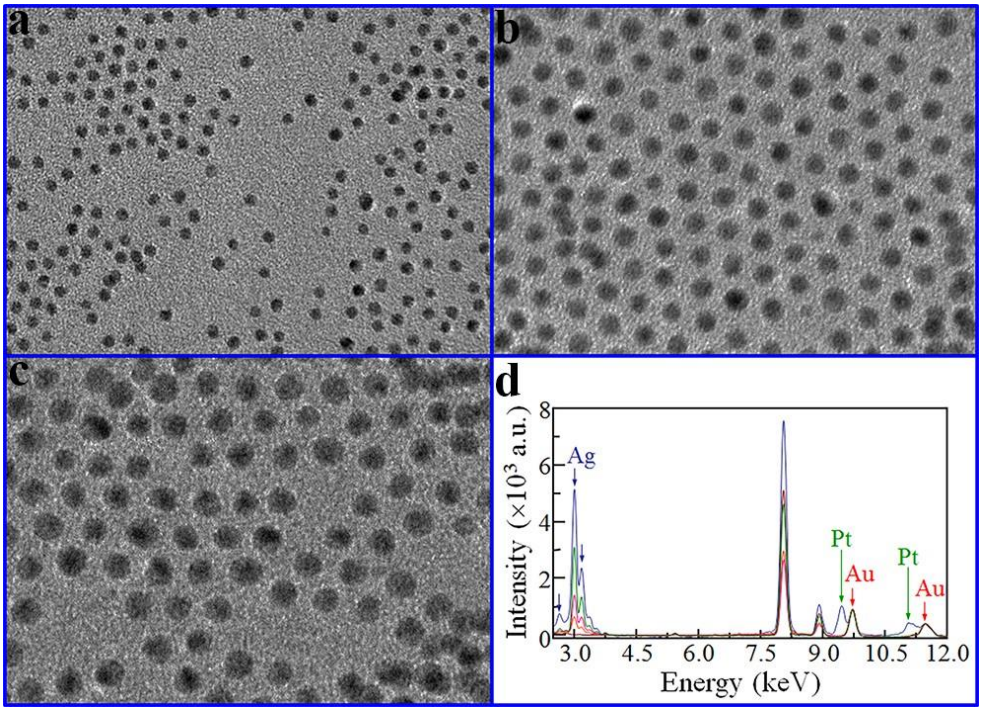

Figure 7. Layer-by-layer engineering of Au-Ag-Pt core-shell-shell structures. TEM image of (a) pure 3.8nm-Au nanoparticles. (b) Au-Ag (6 layers) core-shell nanoparticles. (c) Au-Ag (9 layers)-Pt (2 layers) core-shell-shell nanoparticles. (d) Ensemble EDS spectra of the Au-Ag-Pt core-shell-shell nanostructures shown in Figure 6a. To compare relative intensity of Ag (blue arrows), Au peaks (red arrow) are normalized to possess the same intensity for all shell thickness due to constant core size in experiment.

A clear oscillatory component at a longer time delay can be seen in Figure 6c, which is due to impulsively launched the acoustic phonon modes via the e-ph coupling interaction as described above. Because of the isotropic morphology of the core-shell nanostructures as well as the homogeneous laser excitation, these low-frequency phonon vibrations can be assigned to a symmetric radial expansion and contraction of lattice after gaining energy from electron excitation. The optical property of the core-shell nanoparticle can therefore be modulated by the mechanical motion of the lattice, offering the detection mechanism of acoustic phonon modes in a time-resolved optical

spectroscopy. This provides valuable insights of the fundamental breathing modes of acoustic phonon vibration[17,22,23].

2.4 Analysis and discussion

To explore interfacial phonon coupling as demonstrated in Figure 3, we have synthesized a series of the Au-Ag core-shell nanostructures with tunable aspect ratios (and thus tailored relative position of the core-shell interface) by maintaining the size of the Au core constant while varying the thickness of the Ag shell layer-by-layer. The evolution of phonon dynamics with the aspect ratio of the Au-Ag core-shell is summarized in Figure 8a. We have also carried out control experiments with plain solid Au and Ag nanoparticles, and presented the results on the top and bottom of the color map, respectively, for comparison with the core-shell structures. A few key features of the acoustic phonon dynamics of the core-shell nanostructures can be identified: (1) The oscillation frequencies of the Au-Ag show dependency on its aspect ratio. The frequencies increase layer-by-layer as the aspect ratio of sample increases; (2) The frequency of fundamental breathing modes manifested in the Au-Ag core-shell nanostructures is much higher than those of both plain solid Au and Ag nanoparticles in the whole range of aspect ratio that we have investigated, suggesting existence of interfacial phonon coupling between the core and shell constituents; and (3) The recorded oscillatory pattern from one single Au-Ag core-shell shows beating characteristics, which suggests that more than one phonon mode might be present.

Accordingly, the observed oscillation trace can be fit well with a phenomenological response function[125]:

$$D(t) = \sum_{n=0}^{2} D_n e^{-\frac{t}{\tau_n}} \cos(\frac{2\pi}{T_n} t + \phi_n)$$

where D_n, τ_n, ϕ_n, and T_n are amplitude, decay time, phase and oscillation period of the *n*th-order radial phonon mode, respectively. We have observed that for most of the Au-Ag core-shell samples more than one frequency is typically required for a good fitting to the experimental data (Figure 8a). The existence of multiple radial phonon modes as well as their evolution with aspect ratio can be further revealed by the Fourier transform (FT) spectra of time-resolved data, as presented in Figure 8b. Three distinct phonon vibration frequencies can be identified for most of the Au-Ag core-shell structures, and be attributed to the n= 0, 1 and 2 radial phonon modes, respectively. To compare with our FEM simulation, we have normalized as-measured phonon frequencies for different phonon modes in Figure 8c.

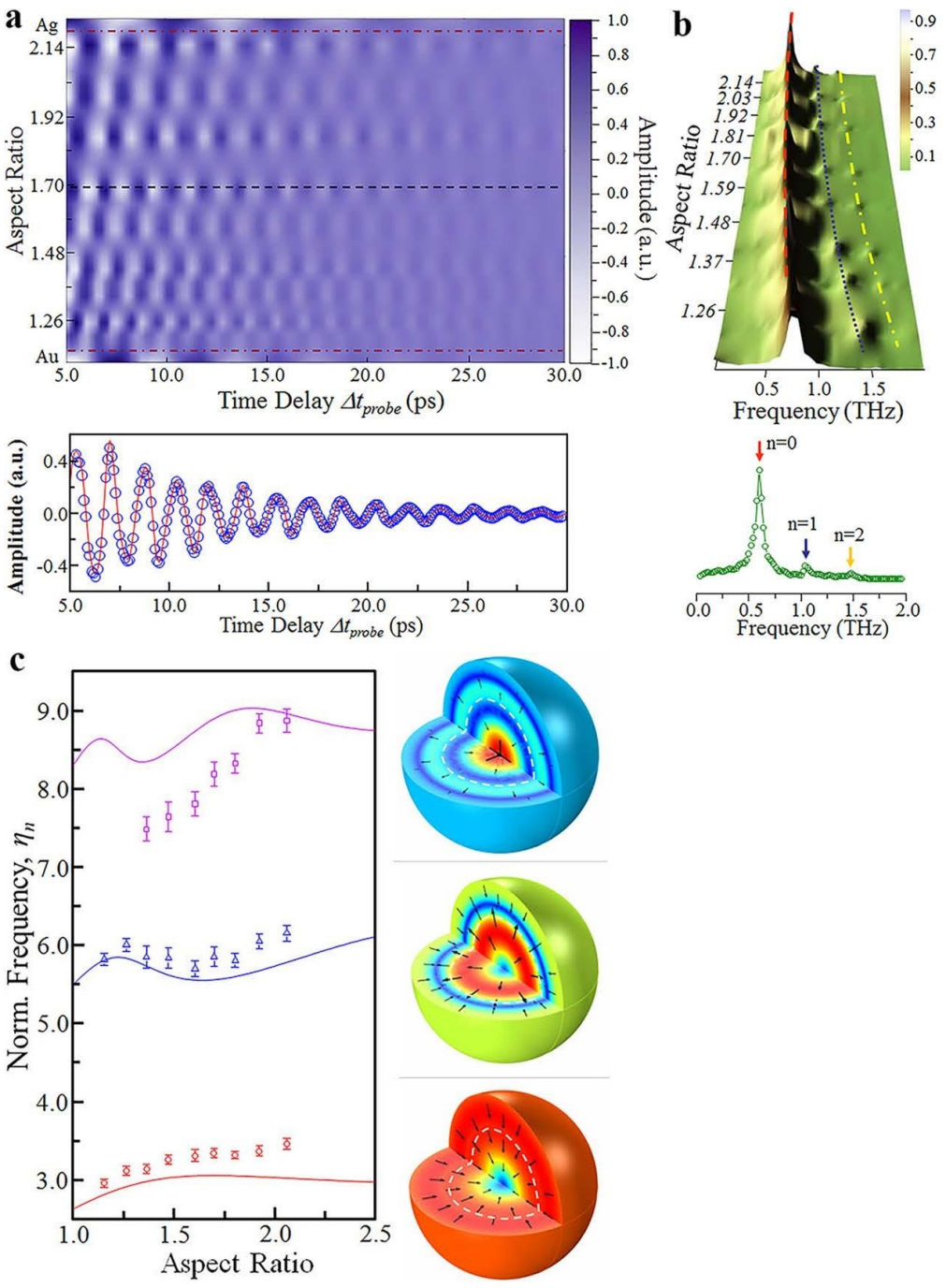

Figure 8. Observation of the interfacially coupled acoustic phonon modes in the Au-Ag core-shell nanostructures. (a) (Top) Color map of the phonon oscillation modulation in the recorded ($\Delta T/T$) data, showing its dependence on the aspect ratio of a core-shell nanostructure. For comparison, the results of 3.8nm diameter plain solid Au nanoparticles and 9.5nm- diameter plain solid Ag nanoparticles are also presented in the bottom (below the red dash-dot line) and top (above the red dash-dot line) of the color map, respectively. All data are processed and presented by removing residual

exponential background contributed from the e-ph scattering process. (Bottom) The time-resolved data acquired from the sample with six layers of the Ag shell is shown (blue circle), which corresponds to the black dashed cross section in the two-dimensional color map. The red solid line is a fit ($D(t)$) to this experimental data. (b) (Top) Color map of the FT spectra of the time-resolved data shown in (a), highlighting the presence of three distinct phonon frequencies as well as their dependence of the aspect ratio of a core-shell nanostructure. The red dashed, blue dot and yellow dash-dot lines are guides to eye for three distinct frequencies assigned to the n=0, 1, and 2 modes, respectively. (Bottom) A typical FT spectrum of the time-resolved trace presented in the bottom of (a). (c) Comparison of experimental η_n with the computed values presented in the Figure 3b (the data in the Figure 3b are re-plotted here for the comparison purpose). The red, blue and magenta symbols are experimental values of the n=0, 1, 2 radial acoustic phonon modes, respectively. The error bar of experimental data is determined by Lorentzian fitting to the FT peak at different phonon frequencies. Computed three-dimensional lattice motion of the core-shell structures under excitation of different phonon modes are also illustrated on the side with the core-shell interface highlighted by a white dashed curve. The black arrow highlights lattice displacement direction.

Importantly, the dependence of the experimental normalized phonon frequencies on the aspect ratio follows our FEM simulation and manifests oscillatory characteristics for n=1 and 2 modes as predicted. This provides for the first time a clear evidence of existence of coherent interfacial phonon coupling between the core and shell constituents and reveals how the spatial confinement and the nanoscale interfacial coupling of phonons can be utilized to engineer the phonon spectrum. We have also noticed that there exists a small deviation between our measured values of phonon frequencies and the computed ones. While more experiments and modeling are needed to fully elucidate such deviation, there exist a couple of possibilities: (1) Bulk mechanical parameters are employed in our FEM calculation. However, it has been shown that nanoscale structures possess modified mechanical properties, including Young's modulus and Poisson's ratio[126,127]. (2) The surface/interfacial tension in such small-sized particles due to the non-coordinating atoms and the mismatched interface

may also contribute to the deviation[128]. (3) Classical continuum mechanics model is employed in our FEM simulation. While this classical model has been demonstrated to be sufficient for large-size nanostructures, correction at the very small length scale might be necessary to elucidate full phononic features[129,130]. Particularly, in our experiment the core-shell nanostructures with a thinner shell manifest a larger deviation from the theoretical values, as compared with that from samples with the thicker shells. This becomes more prominent for the n=2 mode. Overall, the agreement between our experiment and simulation as demonstrated in Figure 8c suggest that our modeling has addressed the essence of the nanoscale interfacial phonon coupling. Because the acoustic phonon vibrations bear a unique signature of their structural and mechanical characteristics, more thorough systematic study in the future should offer valuable insight of extreme quantum limit of mechanical and phononic interactions at the nanoscale that could be challenging to study otherwise.

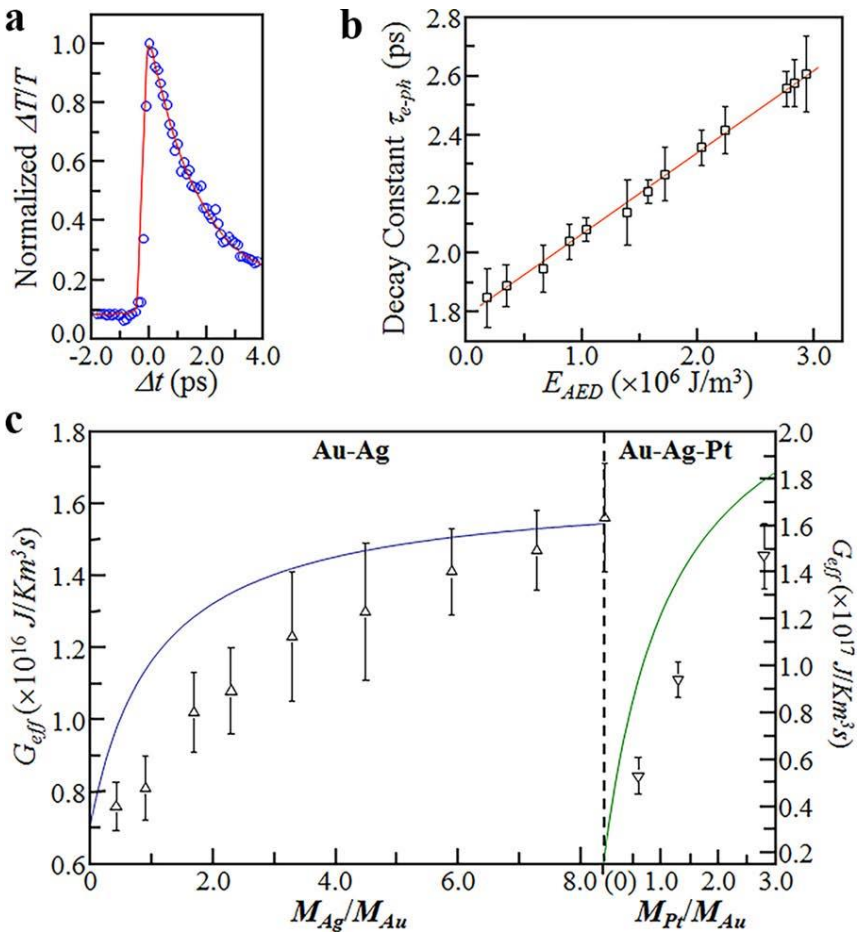

Figure 9. Layer-by-layer tuning of e-ph coupling constant in the Au-Ag-Pt core-shell-shell nanostructures. (a) Data (below 5 ps) from sample with six layers of silver shell (blue circle). Red solid line: theoretical fitting with two-temperature model. From fitting, $\tau_{e\text{-}ph}$ can be determined. (b) Experimental E_{AED} dependence of $\tau_{e\text{-}ph}$. Red line is a linear fit to data. (c) Dependence of G_{eff} on molar ratio of shell and core. Molar ratio is determined from EDS measurement as shown in Figure 7c. Up and down triangles are experimental data, and blue and green solid lines are calculated G_{eff}.

As shown in the Figure 6c, the observed interfacial phonons are impulsively launched via the e-ph coupling process. We have further quantized this process based on the framework of a two-temperature model, and if only conduction electrons near E_f are excited (i.e., under weak perturbation regime as illustrated in the Figure 6b) that

typically occurs in our experiments (see Methods) the e-e and e-ph scattering processes can be quantized as follows[116]:

$$\Delta T/T(t) = A\int_{-\infty}^{\infty} H(t)\left(1 - e^{-\frac{t}{t_{e\text{-}e}}}\right) e^{-\frac{t}{t_{e\text{-}ph}}} e^{-\frac{(t-t)^2}{t_0^2}}\, dt + B\int_{-\infty}^{\infty} H(t)\left(1 - e^{-\frac{t}{t_{e\text{-}ph}}}\right) e^{-\frac{(t-t)^2}{t_0^2}}\, dt \quad ,$$

where $H(t)$ is the Heaviside function, A and B are fitting parameters that represent contributions from different scattering processes, $\tau_{e\text{-}e}$ is the decay time constant due to the e-e scattering and τ_0 is cross correlation width of pump and probe laser pulses. The first term in the equation describes purely electronic response which rises with time constant $\tau_{e\text{-}e}$ and decays by electron energy transfer to phonon with effective e-ph coupling time constant $\tau_{e\text{-}ph}$; and the second term describes the energy gain of phonon rising with $\tau_{e\text{-}ph}$. The $\tau_{e\text{-}ph}$ can be further found to be related to absorbed pump-laser energy density (E_{AED}) with a linear relationship as[23]: $\tau_{e-ph} = \left(\frac{\gamma T_0}{G}\right) + \left(\frac{1}{T_0 G}\right) E_{AED}$, where γ is the electron heat capacity coefficient and T_0 represents room temperature. Our experimental data in Figure 9a shows excellent agreement with the two-temperature model, and importantly $\tau_{e\text{-}ph}$ obtained from fitting of $\Delta T/T$ shows predicted linear dependence on E_{AED}, yielding the effective G value (G_{eff}) of core-shell structure (Figure 9b). We summarize experimental results of G_{eff} from different shell layers in Figure 9c. A few features can be immediately addressed: (1) the G_{eff} shows monotonic increase as the Ag shell thickness increases; (2) the outgrowth of Pt shell can significantly enhance the G_{eff} factor (one-order larger) as compared with the values of Au-Ag core-shell; and (3) the G_{eff} of Au-Ag-Pt also shows monotonic increase as the molar ratio of Pt increases. In order to gain insights of observed tendency of G_{eff} in

artificial core-shell nanostructures, we assume that relative contribution of different component to the G_{eff} mainly depends on the number of available electronic states at the E_f [115,116], and we find that under first order approximation G_{eff} can be expressed as: $G_{eff} = \sum_i \alpha_i G_i$, where G_i, $\alpha_i = \frac{M_i(N_E)_i}{\sum_j [M_j(N_E)_j]}$, $(N_E)_i$ and M_i represent e-ph coupling constant, fraction of electronic states at E_f, density of state at E_f, and molar ratio of ith-component in an artificial core-shell-shell nanostructure, respectively. Because M_i can be experimental determined from EDS measurement (see Figure 7), theoretical G_{eff} can thus be calculated and compared with our experimental data, as shown in Figure 9c. Qualitatively, our observed tunability of G_{eff} in artificial Au-Ag-Pt nanostructures follows theoretical prediction, suggesting that the desired G constant of a nanostructure should be able to be achieved by judiciously tailoring its architecture and composition.

2.5 Conclusion

In summary, we have demonstrated interfacial acoustic phonon coupling by investigating a well-defined concentric core-shell nanostructure, and the unique oscillatory modulation of higher order phonon spectra ($n \geq 1$) due to the core and shell ph-ph interaction has been unambiguously confirmed for the first time. Furthermore, fundamental e-ph coupling constant of complex core-shell nanostructures can be measured, and is found to be monotonically tailored by layer-by-layer engineering of shell thickness and constituent. All these results together have important implications in several fronts.

First, phonon engineering is the basis for understanding material properties and for designing nanostructures to address specific need. By combining with recent materials advances in fine synthetic control of various complex hybrid hetero-nanostructures[37,38], nanoscale interface can be tailored in a highly controllable manner through different combination of acoustic characteristics, which might lead to phonon spectrum by design.

Second, our experimental approach for probing interfacially modulated e-ph and ph-ph scattering processes is based on ultrafast spectroscopy with very fine temporal resolution. This should allow combining recent advance in shaped ultrafast optical laser pulses and multiple coherent optical excitation scheme to achieve fully optical control of interfacial quantum states and dynamic process at the nanoscale[131].

Lastly, precisely tailored multimodal nanostructures represent a class of important building blocks for various functional device applications involving electron and phonon interactions. This may lead to optimum phononic devices with rationally designed nanostructures in photothermal therapy[132], chemical reactions[133], thermal energy management[12], and ultrasensitive molecular and biological sensing[23,134].

Chapter 3: Coherent discriminatory modal manipulation of acoustic phonons at the nanoscale

3.1 Introduction

Understanding and controlling phononic characteristics in solids is crucial in order to elucidate many physical phenomena and to develop new phononic devices with optimum performance. While substantial progress on spatial control of phonons by materials design has been achieved in the past, manipulation of phonons in the time-domain has been less studied, which can enable in-depth insight into various phonon-coupling processes.

Herein, we have utilized a recently developed bimetallic core-shell nanostructures whose phonon modes can be precisely tailored through acoustically mismatched core-shell interface[39,48], as a model system to demonstrate feasibility of discriminatory multimodal manipulation of phonons at the nanoscale. We have first demonstrated by FEM simulation that sequential application of impulsive excitations of acoustic phonons can be employed to control phonon modes in a coherent and highly selective manner. From the classical perspective, such phononic control schemes can be understood as the constructive and destructive interference of multiple impulsively excited phononic waves, with prediction of monotonic modulation of phonon vibrational amplitude by varying time interval between them. Importantly, when a dual control pulse scheme is employed, different phonon modes can be selectively enhanced

or annihilated by controlling combination of two sequential control pulses. Experimentally, such coherent discriminatory multimodal phonon manipulations should be achievable by designing and employing a set of femtosecond optical pulses in an ultrafast optical study.

In our current work, we have further demonstrated in experiment both monotonic modulation of fundamental phonon mode in the simple single control pulse scheme and more selective control of different higher-order phonon modes in a complex dual control pulse scheme, agreeing well with the FEM simulations. This work highlights the feasibility of in-situ ultrafast phonon control in a highly selective manner in the time domain, thus opening up new exciting avenue to understand and even manipulate phonon-mediated physical and chemical processes with penetrating insight of roles of specific phonon modes, when integrating with other experimental techniques[135-138], which will be very challenging otherwise.

3.2 Simulation

Figure 10a shows schematic coherent phonon control in the time domain, from the wave perspective. Phonon vibrations can be impulsively launched in a nanoscale atomic lattice with broadly distributed modes (denoted by n = 0, 1, 2..., where n is the quantization mode number), possessing distinct frequencies, phases and amplitudes. Typically, the fundamental mode (n= 0) possesses large vibrational strength as compared with higher-order modes (n> 0) in a broadband phonon excitation. Following this initial phonon excitation, a second short pulse (termed "control pulse") can be

introduced to coherently interact with the existing phonon vibrations, leading to a redistribution of the mode energy. When the width of the excitation and control phonon pulses is short enough, the relative phase of specific phonon mode under sequential excitations can be precisely tuned, leading to modal enhancement or annihilation. This wave perspective and phase control concept can in principle be further extended to a more complex and selective phonon manipulation by designing an advanced sequence of independent phonon pulses.

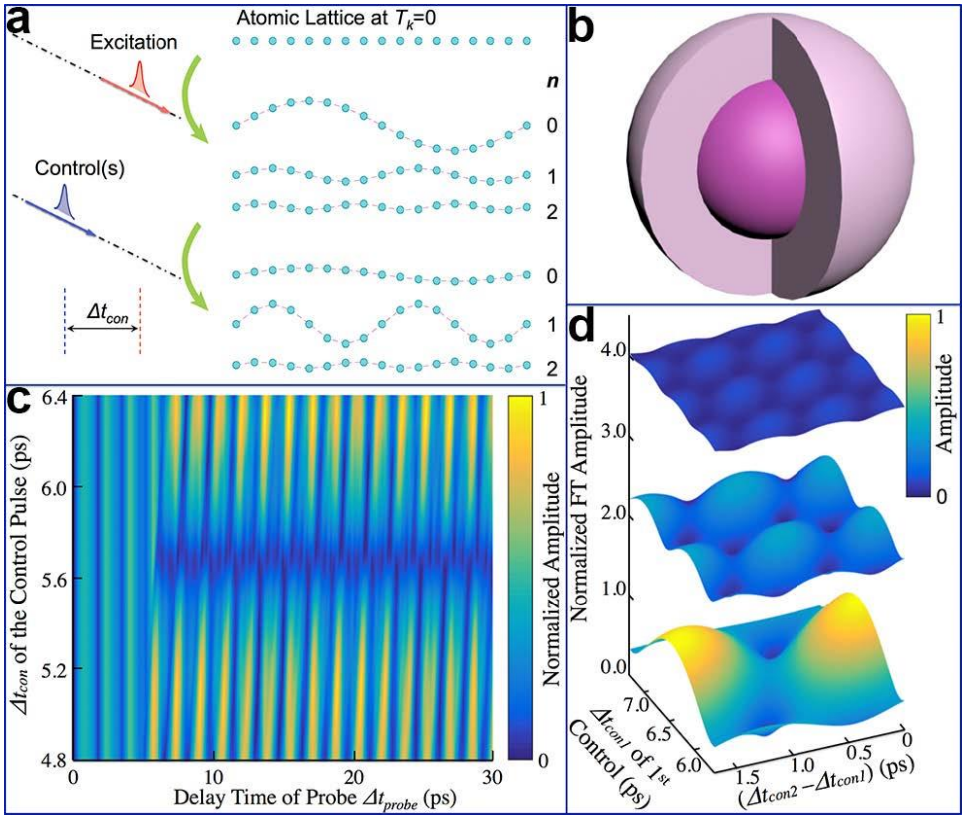

Figure 10. FEM simulation of discriminatory modal phonon manipulation. (a) Schematic of coherent discriminatory phonon manipulation by impulsive phonon excitation. (b) Model of a core-shell nanostructure to allow precisely engineered phonon spectrum that can be desirable for phonon manipulation. (c) FEM computed phonon control via the single control pulse scheme. Two-dimensional map of phonon vibrational dynamics is plotted by varying Δt_{con} of control pulse with respect to the initial phonon excitation at t= 0. The color bar is the normalized phonon intensity (to maximum phonon amplitude). (d) FEM computed phonon control via a dual control

pulse scheme. Two-dimensional FT amplitude maps of FEM computed phonon dynamics after application of two sequential control pulses are plotted for three distinct phonon modes, respectively. For clarity purpose, the FT amplitude maps of $n = 1$ and $n = 2$ modes are shifted up vertically by two and four units, respectively.

It has been shown that classical continuum mechanics with FEM simulation can be applied to nanoscale structures to understand their acoustic phonon characteristics, showing good agreement with experimental results[48,139,140]. Therefore, we have employed time-domain FEM simulation to implement and evaluate proposed phonon manipulation schemes illustrated in Figure 10a. Briefly, in our simulation, a uniform impulsive force with fs-pulse width is applied onto the nanoparticle with an isotropic elasticity to excite acoustic phonons, and its time-dependent surface displacement is computed and recorded as a signal of phonon vibrations. We have particularly chosen an Au-Ag core-shell nanostructure as a model system (Figure 10b) for our current work because prior work has demonstrated that this type of nanostructures can allow a precise engineering of a series of phonon modes via tailoring interfacial acoustic coupling[48], thus representing an ideal system to demonstrate multimodal phonon manipulation as illustrated in Figure 10a. Figure 10c presents a computed two-dimensional map of time-dependent phonon oscillation under the single control pulse scheme, in which a second impulsive phonon excitation (as control) is applied after initial excitation with a time interval of Δt_{con}. By sweeping Δt_{con}, a clear suppression and enhancement of phonon vibration can be observed, depending on the specific value of Δt_{con}. The Fourier transform (FT) analysis of computed time-dependent phonon dynamics has shown that the fundamental mode is dominant under such impulsive excitation, and a clear and strong modulation of this specific phonon mode is revealed,

while variation of higher-order modes is relatively weak under the single control pulse scheme (Figure 11).

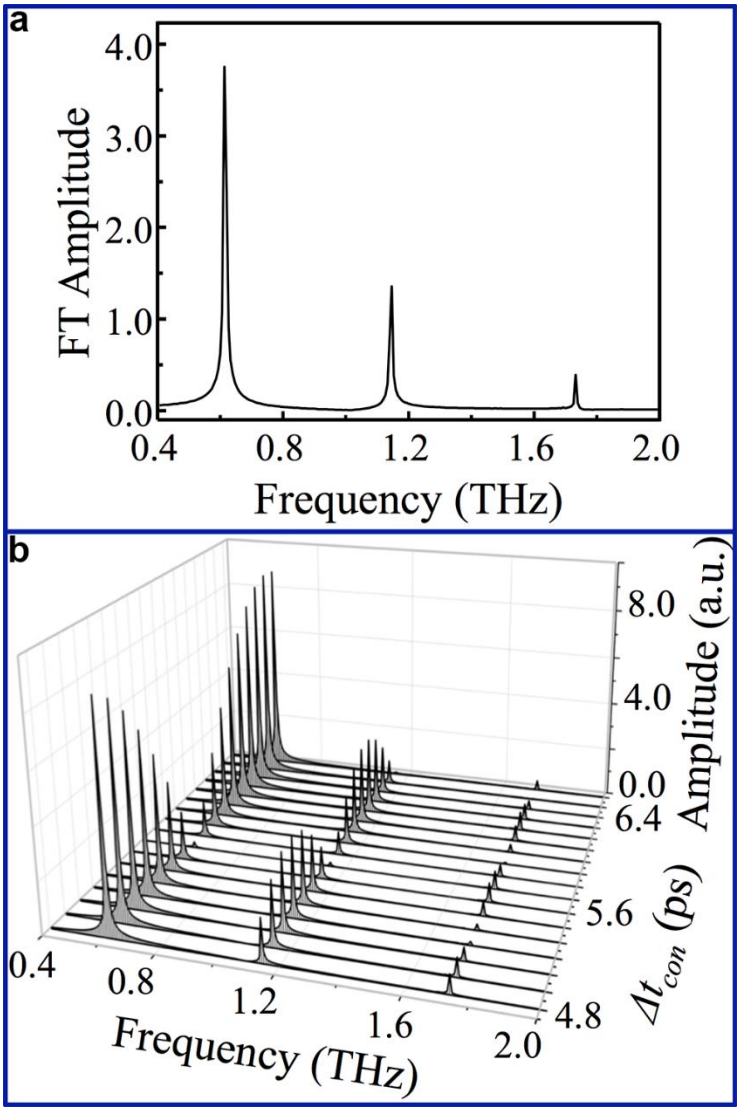

Figure 11. FT spectra of simulated phonon dynamics of Au-Ag core-shell nanoparticle in the single control pulse scheme. (a) A typical FT spectrum without application of control pulses. Phonons are launched by applying an impulsive force to nanoparticle; (b) Evolution of FT spectrum with Δt_{con} in the single control pulse scheme. Between plot curve and baseline (FT amplitude = 0), gray color is filled to enhance the visibility.

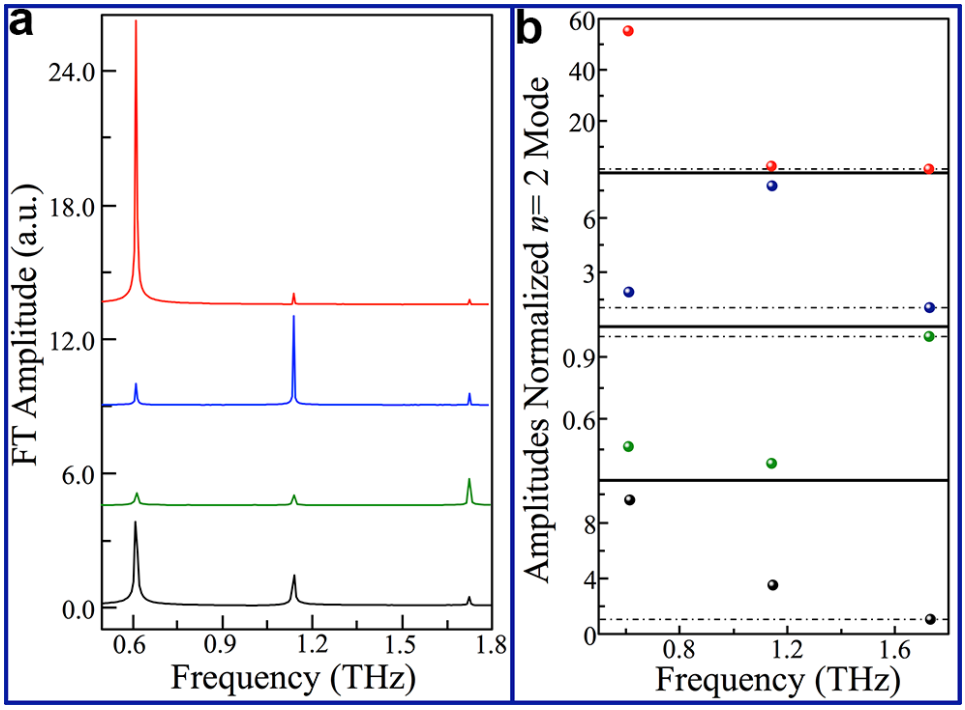

Figure 12. FT spectra of simulated phonon dynamics of Au-Ag core-shell nanoparticle in a double control pulses scheme. (a) Selected FT spectra of phonon dynamics with different combinations of Δt_{con1} and Δt_{con2}. Black: No control pulses. Green: Δt_{con1}= 0.56 ps and Δt_{con2}= 1.12 ps. Blue: Δt_{con1}= 6.0 ps and Δt_{con2}= 7.1 ps. Red: Δt_{con1}= 6.7 ps and Δt_{con2}= 8.2 ps; (b) Modulation of the interplay among three different phonon modes (n= 0, 1 and 2). FT peak amplitudes of different phonon modes are normalized to that of n=2 mode in order to highlight and compare different modulation of distinct phonon modes under different experimental conditions. Assignment of color code is the same as that in (a). Comparison among three control conditions and absence of control pulse confirms that amplification of specific phonon modes by selecting different manipulation conditions in a double control pulses scheme can be uniquely achieved.

We have further evaluated a more complex control scheme consisting of dual control pulses while the time interval of each control pulse relative to the initial excitation pulse (i.e., Δt_{con1} and Δt_{con2}) can be independently tuned. A few exemplary maps of computed phonon dynamics under different combination of Δt_{con1} and Δt_{con2} are presented in Figure 12, showing more complicated phonon dynamic features in such a dual control pulse scheme. To evaluate effects on different phonon modes in this manipulation

process, we have computed and compared vibrational amplitudes of different phonon modes (n = 0, 1, 2) as a function of Δt_{con1} and Δt_{con2}, and presented the results in Figure 10d. For each phonon mode n, a periodic modulation of phonon vibration amplitude as a function of Δt_{con1} and Δt_{con2} exists, originating from the harmonic nature of the acoustic vibrations, but the modulation pattern shows a clear dependence on the phonon mode because of the difference in their inherent phonon frequencies. As compared with the computational results from the single control pulse scheme, one immediate implication of Figure 10d is that by judiciously selecting a combination of Δt_{con1} and Δt_{con2} one specific phonon mode can be enhanced or suppressed, leading to discriminatory modal control of phonons, or more general design of the phonon modal spectra consisting of merely desirable modes. Figure 13 shows a few examples to highlight such discriminatory modal control of n= 0, 1 and 2 modes, respectively, that can be enabled by choosing different combination of Δt_{con1} and Δt_{con2}.

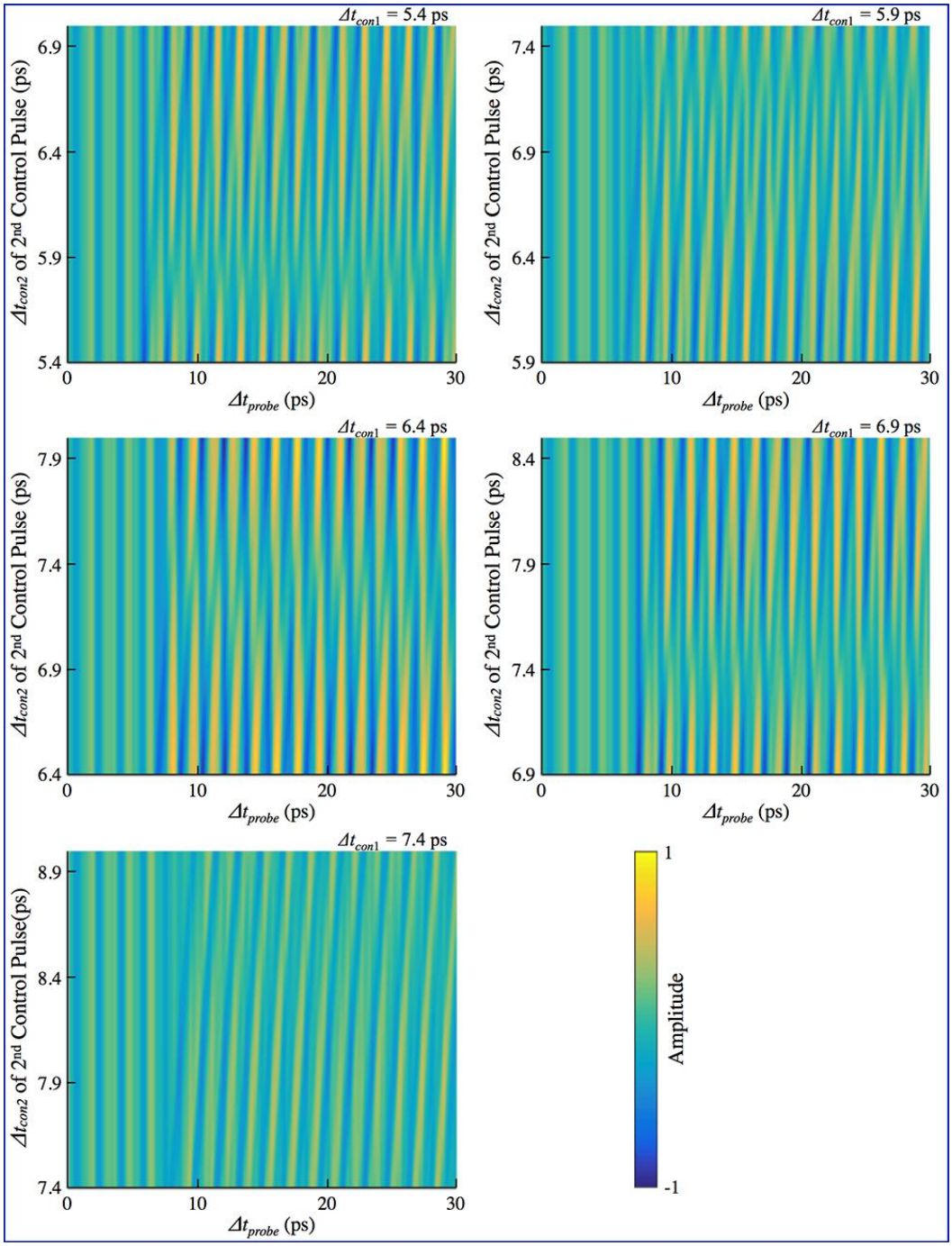

Figure 13. Simulated phonon dynamics of Au-Ag core-shell nanoparticle in a double control pulses scheme with different combination of Δt_{con1} and Δt_{con2}

3.3 Experiment

Experimentally, there exist a few challenges in order to realize phonon control as illustrated and predicted in Figure 10: First, it requires an impulsive mechanism to excite phonons in a time scale much shorter than the related energy redistribution; Second, availability of multiple pulses with precise control of relative time separation is desirable in order to achieve tunability and gain understanding of the manipulation process; Third, an extremely sensitive and in-situ technique for probing variation of phonon dynamics in the time domain should be crucial while performing phonon manipulation; And last but not the least, from a materials standpoint it requires exceptional sample quality in order to achieve long enough phonon coherence time and suitable vibrational frequency to allow application of a pulse sequence before the occurrence of phononic decoherence.

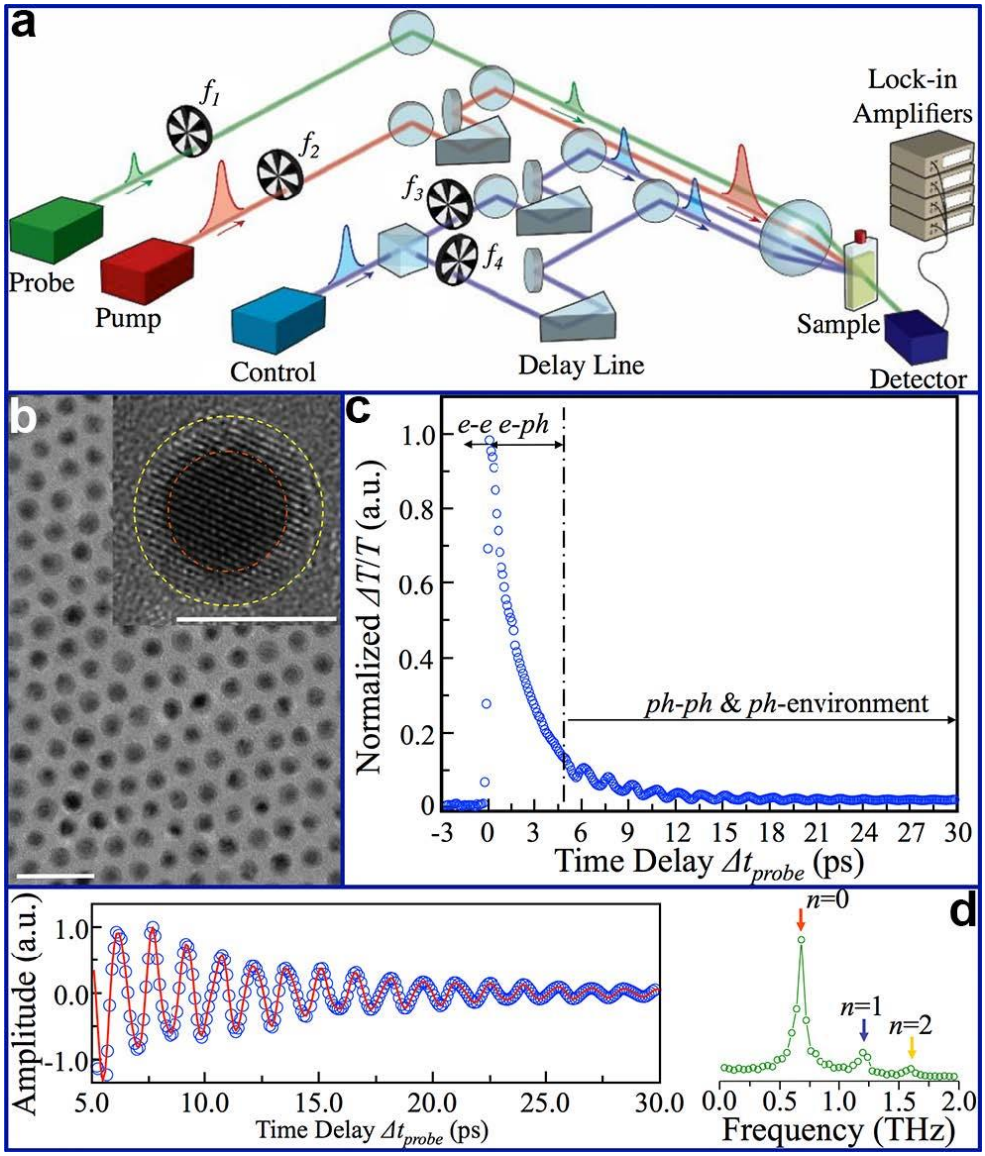

Figure 14. Experimental all-optical setup and Au-Ag core-shell nanostructures for coherent phonon manipulation. (a) Schematic of all-optical experimental setup consisting of up to four sequential optical pulses in the time domain. In order to probe weak phonon signal, lock-in detection technique is applied by modulating different optical paths with different frequencies, f_i (i= 1, 2, 3 and 4). (b) A typical TEM image of Au-Ag core-shell nanostructures consisting of Au core (3.8 ± 0.2 nm) and four monolayers of Ag shell (0.9 ± 0.2 nm). Scale bar, 20 nm. (Inset) High resolution TEM image highlighting the core and shell configuration. The red and yellow dashed lines are guides for the core- and shell- boundaries, respectively. Scale bar, 5 nm. (c) Typical normalized experimental differential optical transmission ($\Delta T/T$) as a function of time delay of probe (Δt_{probe}) that is acquired from the sample presented in (b). Impulsive phonon excitation and relaxation with characteristic time scale can be identified. (d) (Left) Experimental signal of phonon dynamics after 5 ps by subtracting data in (c) from exponential damping background. The red solid line is a fit with a damped

sinusoidal function of amplitude to this experimental data. (Right) The FT spectra of phonon oscillation traces presented on the left, showing the presence of three detected phonon modes highlighted by arrows.

Figure 14a shows a schematic of experimental pump-control(s)-probe setup based on femtosecond time-resolved spectroscopy. It has been demonstrated that the broadband impulsive excitation of phonons can be uniquely achieved by utilizing an ultrafast laser with extremely short pulse width through optical excitation of electrons at the Fermi energy followed by electron-phonon (e-ph) coupling process[22,23,48,141]. In our apparatus, up to four ultrafast coherent optical pulses with pulse width of ~70 fs can be sequentially delivered to the sample with independent control of their arrival time, and photon intensity and energy to undertake different roles as phonon excitation (pump pulse), phonon manipulation (control pulse(s)) and phonon detection (probe pulse), respectively. While pump and control pulses are always set to possess the same photon energy but with independently tunable power, photon energy of pump and probe pulses can be controlled to maximize phonon detection signal. Briefly, electronic temperature of sample is substantially increased and equalized shortly (less than 0.5 ps) after absorption of ultrafast photon pulse due to electron-electron (e-e) scattering. The energy of hot electrons can be redistributed and exchanged to atomic lattice typically within a few ps through e-ph coupling, leading to an impulsive excitation process of phonons. Furthermore, the coherently excited vibrational motion of lattice periodically oscillates the volume of nanostructures, modulating electronic and optical properties that can be detected by monitoring transient absorption/transmission trace and thus offering a detection mechanism of phonons in the time domain. The detection sensitivity can be dramatically improved by utilizing a lock-in technique with

differential frequency modulation of optical pulses. All these together can meet experimental requirement for phonon manipulation schemes presented in Figure 10.

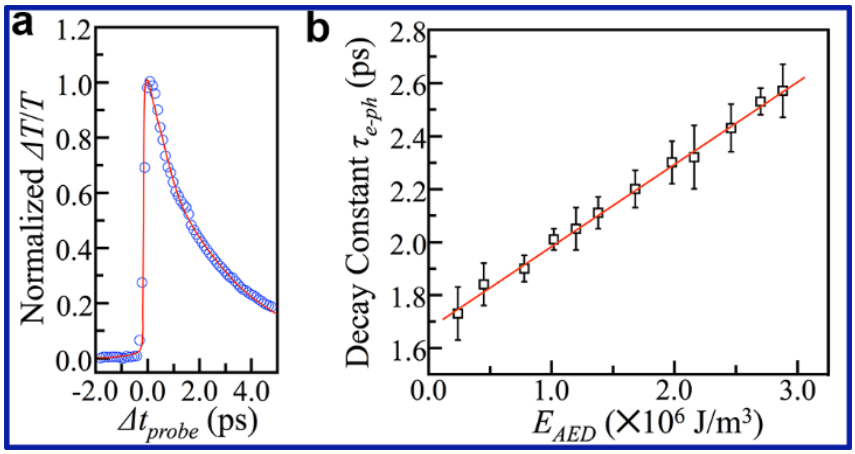

Figure 15. Impulsive optical excitation of acoustic phonons via e-ph coupling. (a) Typical time-resolved pump-probe data (below 5 ps). Blue circle: experimental data. Red solid line: theoretical fitting by using a two-temperature model: $\left(\frac{\Delta T}{T}\right)_t = A\int_{-\infty}^{\infty} H(t)\left(1-e^{-t/t_{e\text{-}e}}\right)e^{-t/t_{e\text{-}ph}}e^{-(t-t)^2/t_0^2}dt + B\int_{-\infty}^{\infty} H(t)\left(1-e^{-t/t_{e\text{-}ph}}\right)e^{-(t-t)^2/t_0^2}dt$, where $H(t)$ is the Heaviside function, A and B are fitting parameters that represent contributions from different scattering processes, τ_0, $\tau_{e\text{-}e}$ and $\tau_{e\text{-}ph}$ are cross correlation width of pump and probe laser pulses, decay time constants due to e-e scattering and e-ph scattering, respectively. (b) Experimental dependence of the $\tau_{e\text{-}ph}$ on the absorbed pump-laser energy density (E_{AED}). The $\tau_{e\text{-}ph}$ is acquired from fitting as the example presented in (a). The red line is a linear fit to data based on two-temperature model. Our experimental observation agrees well with the proposed impulsive phonon excitation mechanism.

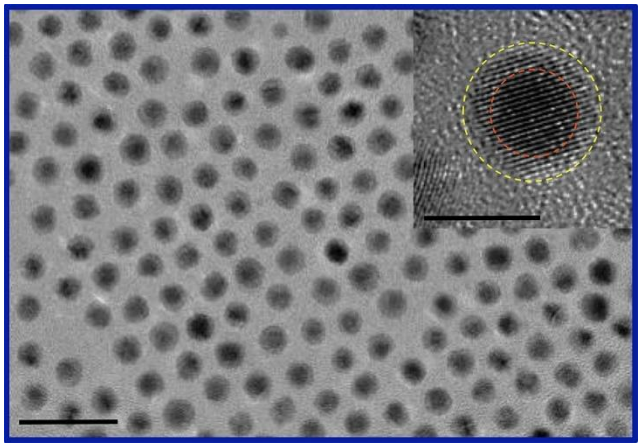

Figure 16. Characterization of sample after extensive optical measurement. Typical TEM image at the large scale. Scale bar, 20 nm. (Inset) High resolution TEM image. Scale bar, 5 nm. By comparing with Figure 14b, no sample damage (both sample distribution and core-shell structure) was observed after optical experiment.

We have employed the optical scheme in Figure 14a to Au-Ag core-shell nanoparticles that can possess intrinsic acoustic phonons with multiple modal frequencies in the regime accessible by optical method. Figure 14b shows a typical electron microscopy characterization of Au-Ag core-shell nanoparticles studied in current work, highlighting its size uniformity that is a prerequisite for optical generation and manipulation of multimodal phonons. Because the size of core-shell nanostructures is very uniform and much smaller than laser focus spot size (~50 μm in our experiment), the impulsive optical excitation of nanostructures can be considered as uniform even under the far-field and ensemble measurement condition. Figure 14c shows a typical time-resolved differential optical transmission spectrum ($\Delta T/T$) with absence of control pulses, clearly highlighting the inter-correlated energy coupling process with different characteristic time scales suitable for the impulsive phonon excitation and phonon detection in the time domain. More detailed analysis of

impulsive phonon excitation through the e-ph coupling mechanism can be found in Figure 15. A clear oscillatory behavior after 5 ps can be identified after removing the fitted background signal with an exponential function (Figure 14d), and its corresponding FT spectrum unambiguously reveals existence of three detected phonon modes that can be assigned as the breathing phonon vibrations with n= 0, 1 and 2 (the even higher-order modes can barely be identified since their modal strength is extremely weak). This agrees well with the FEM simulation (Figure 11a), thus substantiating our modeling in Figure 10. To ensure that our optical observations and manipulations (as presented below) are not caused by photon induced damages due to optical heating or sample degradation, we have also checked sample quality regularly after optical measurements by TEM, and confirmed that we have not yet observed any evidence of sample change after current optical study (Figure 16).

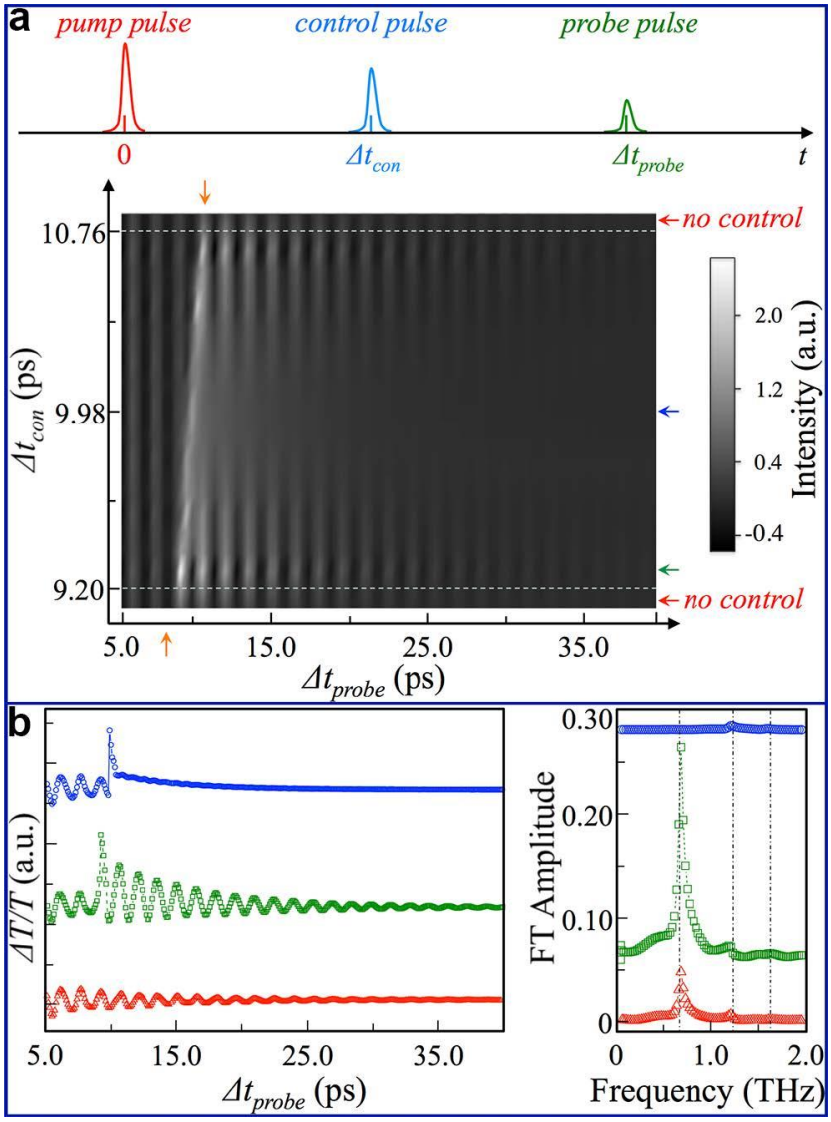

Figure 17. Experimental phonon manipulation via the single control pulse scheme. (a) (Top) Schematic sequence of three optical pluses (pump-control-probe) in the time domain. (Bottom) Experimental two-dimensional map of time-resolved phonon dynamics (after 5 ps) as a function of Δt_{con}. For comparison, two phonon dynamics spectra acquired before and after application of control pulse are also plotted on the top and bottom of map, respectively. Two orange vertical arrows show the tuning range of Δt_{con} of the control pulse in this measurement. (b) (Left) Three selected traces from the map in (a) are presented: Red, no control pulse; Green, Δt_{con}= 9.25 ps; Blue, Δt_{con}= 9.87 ps. Their corresponding positions in the two-dimensional map in (a) are also highlighted by arrows with same assignment of color code. (Right) Corresponding FT spectra of the three phonon dynamic traces shown on the left. For clarity purpose, the green and blue spectra are shifted up vertically by 0.06 and 0.28, respectively. However, scale of each spectrum remains unchanged in order to compare their peak amplitude. Three vertical dash-dot lines highlight the frequencies of n= 0, 1, 2 phonon modes.

Figure 17 summarizes experimental results of implementation of one single control pulse scheme. Figure 17a is a two-dimensional map of phonon dynamics, when only the relative time separation between the control and pump pulses (Δt_{con}) is varied while other experimental parameters, such as pulse intensity, remain unchanged. A strong monotonic modulation of phonon oscillations as a manifestation of enhanced and reduced phonon amplitude can be clearly observed when Δt_{con} is swept through one apparent oscillatory period, which qualitatively agrees well with the FEM simulation result (Figure 10b). It is worth noting that while suppression of the fundamental phonon mode of spherical metal nanoparticles was reported earlier[18], dependence of phonon manipulation on Δt_{con} has not yet been achieved, but is crucial in order for the in-depth understanding of phonon manipulation. In order to show experimental relationship among different phonon modes under such single control pulse scheme, three selected time-domain spectra from Figure 17a and their corresponding FT spectra are compared in Figure 17b. By comparing with phonon dynamics in the absence of control pulse (red curve), phonon oscillation can be increased by about four times (green curve) or reduced to be almost untraceable (blue curve), depending explicitly on the pre-selected value of Δt_{con}. Further comparison of their corresponding FT spectra uncovers fine difference among these three different phonon modes in the single control pulse scheme, in which the fundamental n= 0 mode is most dramatically modulated but not higher-order ones (see also Figure 18). This suggests that our single control pulse scheme can be applied to selectively amplify or suppress the fundamental phonon mode in a highly control manner without substantial perturbation of other higher-order phonon modes.

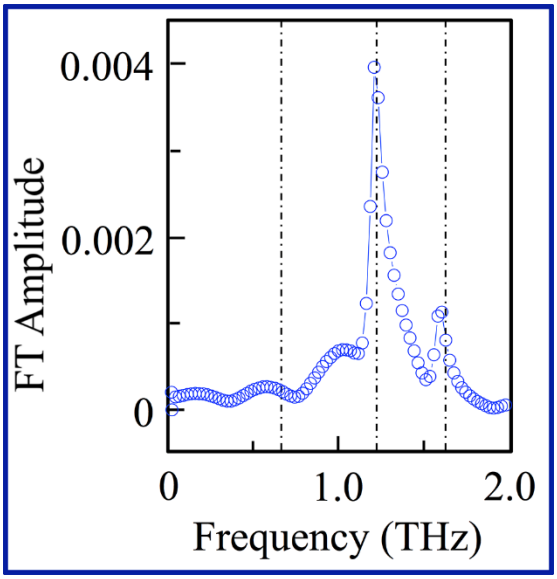

Figure 18. The autoscale plot of the blue colored FT spectrum presented in the Figure 17b (right). The data confirms the complete suppression of n= 0 mode while both n= 1 and n= 2 modes remain under the optical phonon manipulation with the single control pulse.

Because different phonon modes have different characteristics and roles in a phonon associated physical process, it would be necessary to manipulate not only the fundamental mode but also fine interplay between higher-order modes. To achieve coherent control of the finer interplay among different phonon modes, we have further developed a complex dual control pulses scheme as proposed in Figure 10d, with the results shown in Figure 19. The inter-pulse separations of the two control pulses, Δt_{con1} and Δt_{con2}, can be independently controlled relative to the initial pump pulse. The modulation of the phonon dynamics under such control scheme is much more complicated, and intuitively depends on the temporal combination of Δt_{con1} and Δt_{con2}. While a thorough experimental understanding of synergistic interactions among such multiple optical excitations is still under investigation, a clear control of the fine interplay among different phonon modes can be evident from a few selective results

presented in Figure 19. The figure particularly highlights one example showing that in this series of phonon control, while the intensity of $n = 0$ phonon mode is continuously reduced, the intensity of $n = 1$ mode is enhanced in an opposite tendency. This is different from our observation of the single control pulse scheme, in which the fundamental $n = 0$ mode is dominantly modulated, thus showing the promising control of the fine interplay among phonon vibrations achievable in a dual control pulse configuration. By combining with prediction from Figure 10d, our experimental apparatus in Figure 14a should allow considerably flexible control of different phonon modes, that cannot be achieved otherwise.

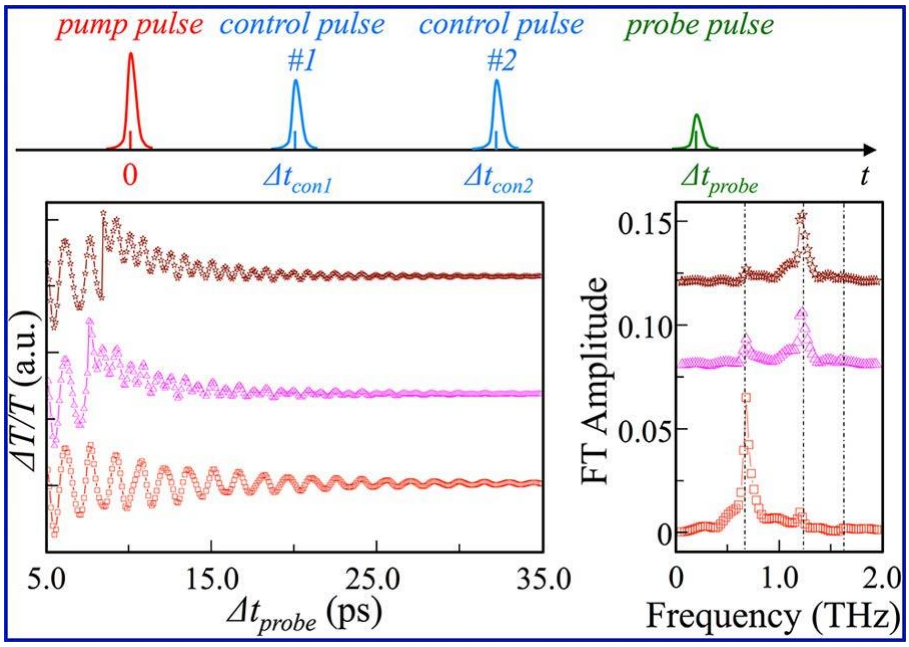

Figure 19. Experimental phonon manipulation via dual control pulse scheme. (Top) Schematic sequence of four optical pluses (pump-control-control-probe) in the time domain. (Bottom left) Three selected phonon dynamics spectra showing the effect of different combination of Δt_{con1} and Δt_{con2}. Red: no control pulse. Magenta: Δt_{con1}= 7.56 ps and Δt_{con2}= 7.68 ps. Wine: Δt_{con1}= 8.47 ps and Δt_{con2}= 8.74 ps. (Bottom right) Corresponding FT spectra of three data presented in the bottom left with same assignment of color code. For clarity purpose, the magenta and wine FT spectra are shifted up vertically by 0.08 and 0.12, respectively. However, the scale of each

spectrum remains unchanged to compare their peak amplitude. Three vertical dash-dot lines highlight the frequencies of n= 0, 1, 2 phonon modes.

3.4 Conclusion

In conclusion, we have performed FEM simulation to evaluate different phonon manipulation schemes and show that distinct phonon modes of nanostructures can be manipulated in a coherent and highly selective manner by the judicious design of a sequence of impulsive phonon excitation. Experimentally, such impulsive phonon excitation sequence can be realized by a train of femtosecond optical pulses, and we have further designed and achieved different all optical coherent phonon manipulations with results qualitatively agreeing well with the FEM simulation. Importantly, we have revealed for the first time that the manipulation scheme consisting of dual control pulses should be enough to allow flexible control of phonon modes in a highly selective manner. Such all-optical phonon manipulation method is universal and can be readily applied to other materials, as long as their phonon decoherence time is long enough to allow application of pulse sequence.

Future work by fine control of a few other experimental parameters, including phase, photon energy, and intensity of control pulses should enrich such all-optical phonon control scheme. Our current simulation and experimental results of discriminatory modal manipulation of nanoscale phonons have immediately opened up a few exciting research opportunities.

First, phonon vibration is one of the most important subjects in the field of condensed matter physics. Coherent manipulation of phonons in the time domain allows elucidation of different phonon relaxation and decoherence mechanisms in real time.

Second, while understanding roles of phonons in various processes has been intensively studied from both theoretical and experimental points of view, differentiation of distinct phonon modes specifically in the relevant process has been lacking mainly because of the absence of efficient experimental approach to manipulate phonon modes in a highly selective manner. Therefore, discriminatory modal manipulation of phonons enabled in our current work should shed the light to differentiate distinct roles of phonon modes. In particular, our phonon manipulation schemes are based on ultrafast all-optical approach. Ultrafast optical spectroscopy has also been employed to study a wide range of physical phenomena, including spin and exciton dynamics[97,142-145], thus offering a seamless integration with all optical phonon manipulation in our current work to uncover roles of phonons and even control diverse phonon-assisted physical processes.

Lastly but not the least importantly, recent materials advance has allowed refined control of nanostructures with precisely engineered phonon characteristics[23,37,38]. Therefore, combining fundamental understanding of phonon modes with materials advances should lead to new design guideline of nanostructures to possess optimized property and functionality.

Chapter 4: Metamaterials for thermal management

4.1 Introduction

Many species in nature have evolved elegant strategies to manipulate thermal radiation for heating and cooling purposes. For instance, Saharan silver ants possess triangular shaped hairs that can reflect near-infrared rays according to the position of the sun to efficiently dissipate heat[56]. Although a few artificial structures, including photonic crystals[55], composite architectures[57], and nanoporous polyethylene films[54], have recently been designed and demonstrated to achieve radiative cooling, the integration of these approaches into practical textiles is challenging. Another limitation of these technologies is that they are non-responsive to environmental changes, lacking an effective mechanism to allow bidirectional heating and cooling regulation[146-148]. An approach that would allow the optical channels in textiles to be adaptively tuned in response to thermal discomfort without any additional power or device management could fundamentally improve the functionality of our clothing systems.

From the viewpoint of physics, the electromagnetic spectrum and wave propagation of thermal radiation can be engineered by controlling the interactions between conductive elements at length scales that are smaller than or comparable to the desired wavelength[49,50,60]. In the following sections, patterned pillar arrays at the micro-scale will be built up to show how the thermal emission properties of the metastructures can be tuned under the structural variation. Based on the idea, we further design fiber arrays that paves the way for tunable textiles with dynamic cooling in real life.

4.2 Micro-pillar structure as a mid-IR emitter

4.2.1 Fabrication and measurement

To illustrate the proposed mechanism for regulating the emissivity of a textile, we fabricate a series of patterned arrays of carbon-coated polymer pillars with different inter-pillar pitch and investigate their IR response (Figure 20). The pillar arrays are 3D-printed on a glass substrate from a negative-tone photoresist (IP-Dip) by DLW lithography (Nanoscribe Photonic Professional GT). A basal layer is printed beneath the array to improve adherence of the pillars to the glass. Each array is 135×135 μm^2 in size and each pillar was 4 μm in height and 1 μm in diameter, with varied pillar pitches. The printing is programmed to fit all arrays into the same field of view of the thermal imaging system used here. Each array is printed by scanning the laser beam in the galvo mode for a fast printing. The pillars are coated with a thin layer of gold or gold followed by carbon (both 200 nm in thickness) by sputtering.

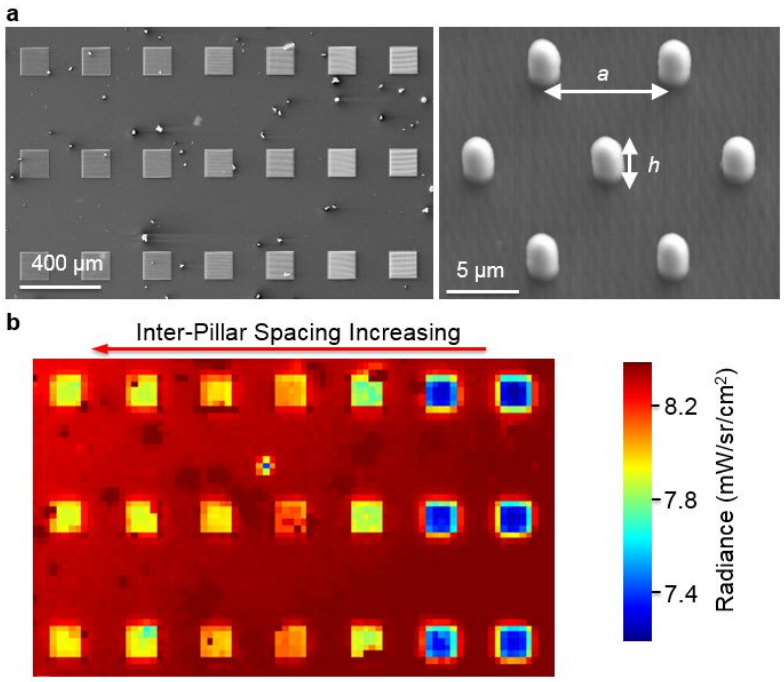

Figure 20. Experimental demonstration of the pitch dependence of the emissivity for each pillar array. (a) SEM images of the fabricated pillar arrays. Left – SEM image of the array with varied pitch from left to right: 3.5, 4, 4.5, 5, 6, 7, and 8 μm. Right – a zoom-in SEM image of the array with a tilted view. (b) Measured radiance of the pillar arrays in (a) at 50 ºC using an infrared camera and a sample heating stage. Different colors indicate varied emissivity.

The pitch dependence of the emissivity is directly visualized using a microbolometer IR camera equipped with a 1.5× close-up IR lens. The sample is placed on a heating stage (T95-PE, Linkam Scientific Instruments Ltd.) to maintain a fixed temperature. and the camera is calibrated against standard blackbody sources. At a sample temperature of 150 °C, the thermal radiation from a series of carbon-coated pillar arrays shows a strong, non-linear dependence on the pitch between pillars (Figure 20b). The radiance is low for small-pitch arrays, maximizes at a pitch of ~6 μm, and then starts to drop as the pitch increases. This dependence remains consistent in the three replicate

rows and for different sample temperatures that are studied, although the absolute intensity changes with temperature as expected for blackbody radiators.

Meanwhile, Fourier-transform infrared (FTIR) spectroscopy in reflection mode is done to obtain the absorption spectra of the samples. The FTIR measurements are performed over a 7–22 μm wavelength range with a Bruker Vertex 70 FTIR spectrometer coupled with a Hyperion 1000 IR microscope, using a liquid N_2-cooled mercury cadmium telluride detector. A Schwarzschild reflective objective (15×, NA=0.4) is used to focus the incident light and collect the reflected light. Since the sample has a gold coating, there is no transmission through the sample, we have absorptance $A = A(\lambda, T) = 1 - R$, where $R = R(\lambda, T)$ is the reflectance and λ is the wavelength and T is the sample temperature. Kirchhoff's law of thermal radiation states that an object's emissivity $\varepsilon_\lambda = \varepsilon_\lambda(\lambda, T)$ equals to its frequency-dependent absorptivity, i.e. $\varepsilon_\lambda = A = 1 - R$[58]. Then the total emissivity can be obtained by numerical integration, $\varepsilon(T) = \frac{E(T)}{E_b(T)} = \frac{\int_0^\infty \varepsilon_\lambda(\lambda,T)E_b(T)}{E_b(T)}$. $E_b(T)$ is the blackbody radiation only depending on the temperature and it can be determined by Planck's law $E_b(T) = \frac{2hc^2}{\lambda^5}\frac{1}{e^{hc/(\lambda kT)}-1}$. Figure 21a shows the total emissivity of each carbon pillar array evolves with the pitch of the pillars.

We also experimentally evaluate gold-coated pillars and compare their performance with that of the carbon-coated ones (Figure 21c). While the gold-coated pillar arrays also offer tunable emissivity, the resonant emissivity and tuning range are much smaller than for carbon-coated arrays. Hence, both thermal imaging and FTIR spectroscopy consistently reveal a strong nonlinear optical coupling effect among the carbon pillars

within an array. These sets of data provide a direct evidence that the pillar arrays' property of radiative emission can be tuned by simply changing the pitch of the array. It suggests that structurally tunable patterned arrays can be utilized to improve thermal management by integrating the arrays into a cooling-demanding system. In the Section 4.3, it will be discussed how fiber arrays (as in functional textiles) can utilized to improve passive cooling of a human body.

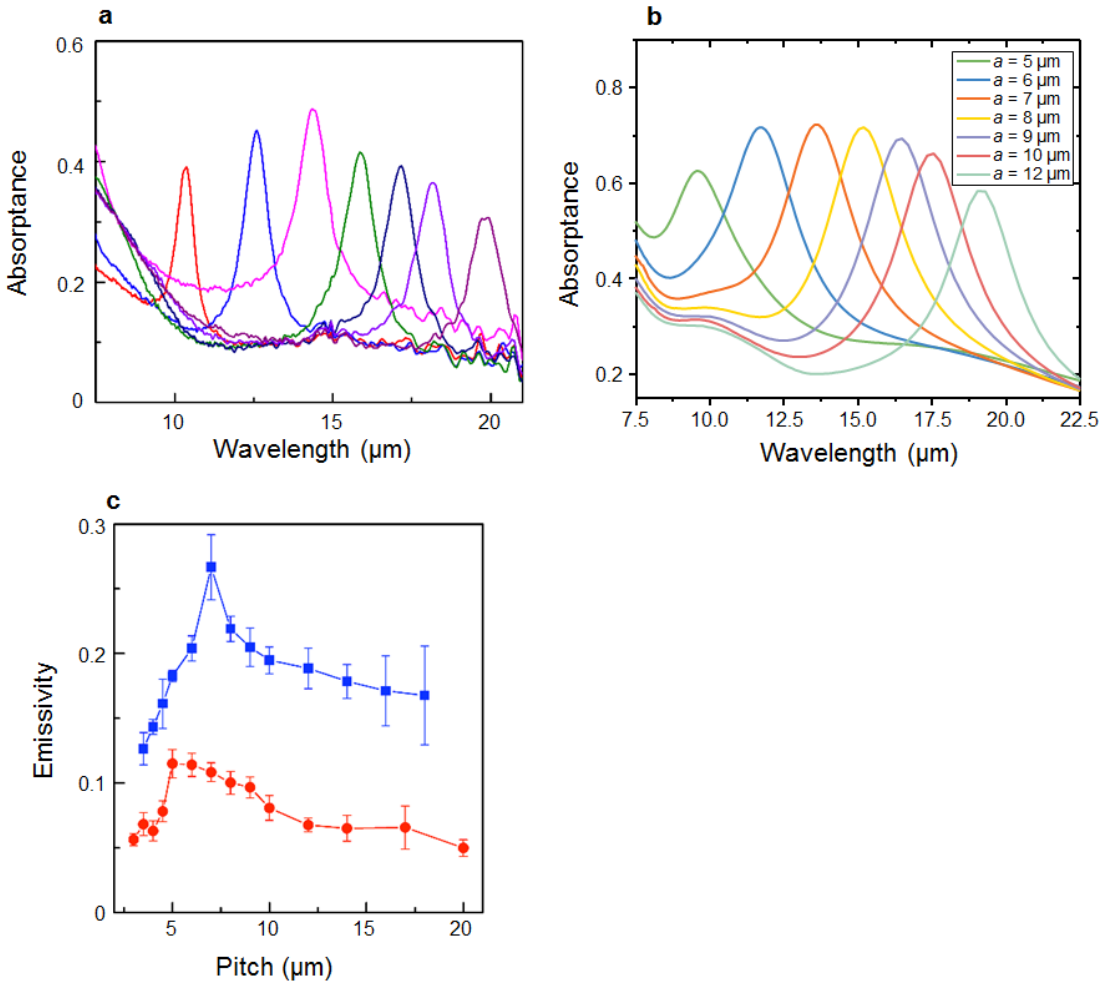

Figure 21. Experimental measurements and FDTD simulation of the pitch dependence of pillar array absorption. (a) Experimentally measured FTIR absorptance spectra from each 3D printed array taken in reflection mode on a FTIR microscope. Note that for

both sets of curves, the center-to-center pillar distances, from left to right, are 5, 6, 7, 8, 9, 10, and 12 μm, respectively. (b) Simulation results of the IR absorption of the carbon-coated pillar arrays. (c) Pitch dependence of emissivity of carbon/gold (blue dots and curve) and gold (red dots and curve) coated pillar array from FTIR absorptance spectra.

4.2.2 Electromagnetic simulation

To confirm that the observed tunability of emissivity is indeed due to electromagnetic interactions among the carbon-coated pillars (as the meta-elements), we further perform finite-difference time-domain (FDTD) simulations based on structural parameters directly from the fabricated carbon pillar arrays.

The numerical simulations of the IR response of the pillar array and meta-textiles are implemented with a commercial FDTD package (Lumerical FDTD Solutions) that models the full-wave electromagnetic response of a specific object by discretizing and solving Maxwell's equations. For the pillar arrays, a unit cell of the structure with periodic boundary conditions is simulated with a plane wave source in the transverse magnetic mode. The k-vector direction is 15º oblique with respect to the sample plane to fully simulate the focused beam under the objective in the FTIR microscope system. The pillar structure is 1 μm in diameter and 4 μm in height. The pillars were set with a constant refractive index of 1.5, and gold and carbon coatings were 200 nm thick each, with dispersive refractive indices[149,150]. The wavelength range of the simulation is 3.0–25.0 μm. Our FDTD simulation results confirm that the IR absorption spectra follow a strong dependence on inter-pillar spacing, in an excellent agreement with the experimental measurements (Figure 21b), suggesting that the observed nonlinear

dependence of the thermal emissivity indeed arises from the electromagnetic coupling between the carbon coatings.

4.3 Metamaterials for thermal management in textiles

In the above section, the emissivity tuning has been demonstrated based on structure-dependent electromagnetic coupling. If such electromagnetic coupling can be controlled at the fiber level it should be possible to achieve a smart meta-textile with dynamically adaptive IR optical properties. Herein, we propose a conceptual design of an IR adaptive textile by integrating metamaterial physics and nanotechnology in textiles to directly regulate their infrared emissivity for personal thermal management. Briefly, a meta-fiber functions via two key components: (1) a meta-element (typically conductive materials) that can be coated onto polymer textile fibers; and (2) an actuation mechanism that can respond directly to changes in temperature and/or the relative humidity of skin.

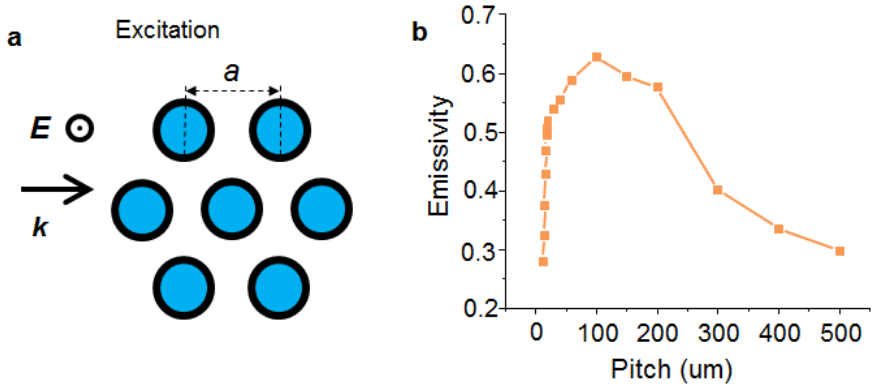

Figure 22. FDTD simulation of the CNT coated fiber array in the close packing pattern. (a) Schematic setup for FDTD simulation of infrared absorption of a hexagonal array of fibers. The left part shows the excitation conditions (polarization and k-vector direction) and the right part shows six pillars of the array structure, in which the blue

core is PET fiber and the black shell is carbon coating. (b) Simulation results of the pitch, *a*, dependence of the emissivity.

In this section, we will focus on how much emissivity tunability it can achieve theoretically. More specifically, we set up FDTD models of the infinitely long carbon-coated fiber arrays (Figure 22a) and consider light scattering and absorption among them. In this case, we simulate the optical response of a periodic array of parallel fibers with the incident light from the side (incident k-vector perpendicular to the fibers). The absorbing boundary conditions are applied for the direction of the incident field. For the two directions perpendicular to the light incidence, periodic boundary conditions are applied. The fibers have a 10 μm-diameter polyethylene terephthalate (PET) core and 200 nm-thickness carbon coating. In Figure 22b, when the fiber pitch is very small, the emissivity is very small, since the light wave is difficult to couple into the system. As the pitch (center to center distance of the fibers in the array) grows, the emissivity quickly increases to a high level. After the pitch extends, the emissivity starts to drop and becomes small when it comes to very large (> 300 μm) scale. Comparing Figure 22b and Figure 21c, there are similar peaks in the plots of emissivity dependence on the fiber pitch, which provides the emissivity tunability.

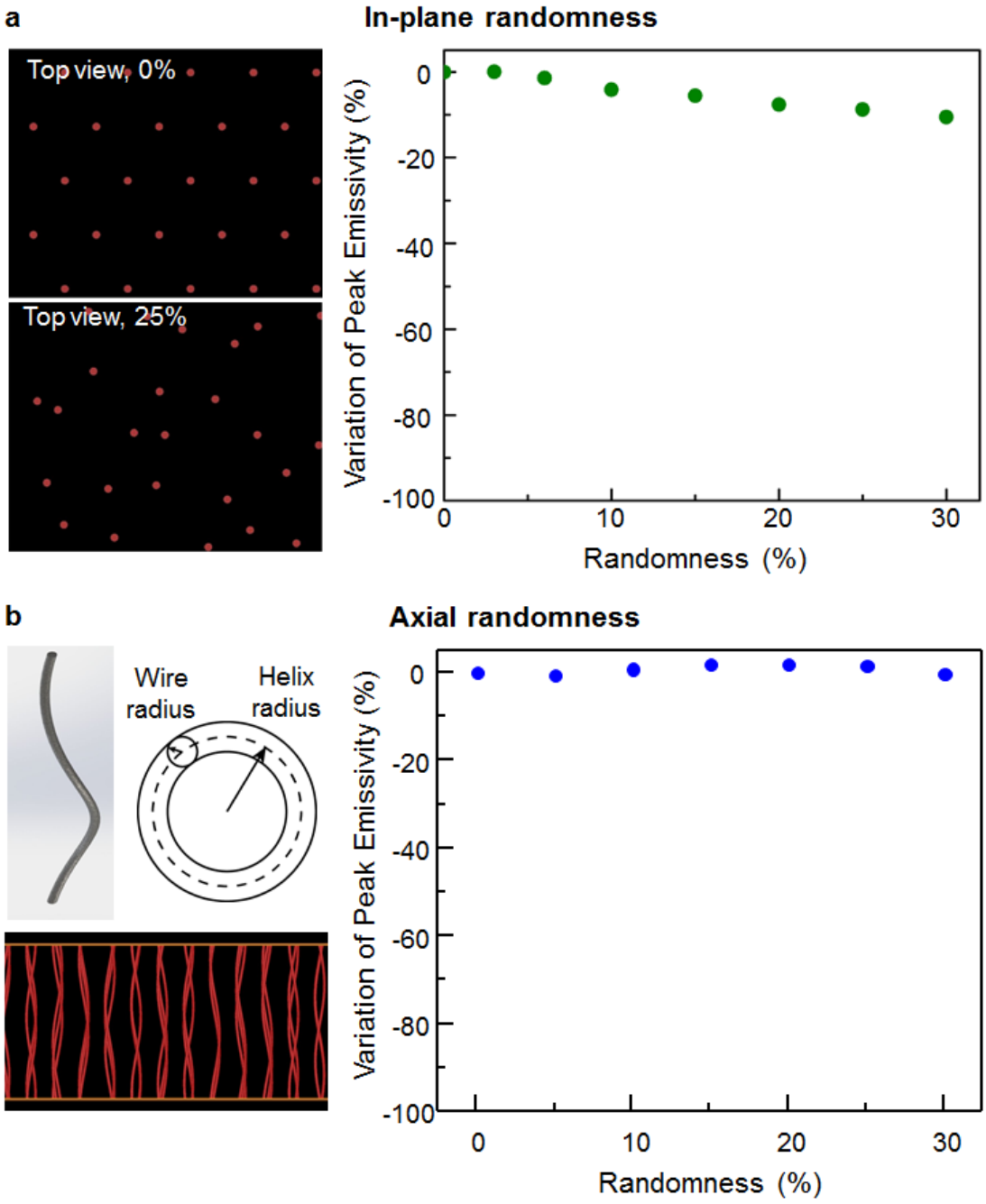

Figure 23. FDTD simulation of the randomness effect on emissivity. (a) Left - Schematic of the pillar array from top view, under 0% (top) or 25% (bottom) randomness. Array with 0% randomness is a perfect array as in Figure 22. Right - variation of peak emissivity under in-plane randomness from 0% to 30%. Peak emissivity shows less than 10% variation with randomness. (b) Left - A helically twisted fiber (top) and schematic of the pillar array under axial randomness (bottom). Right - variation of peak emissivity under axial randomness from 0% to 30%. Peak emissivity varies for less than 2% with randomness.

In real life, the fibers may be patterned but they can hardly be perfectly periodic, and we wonder how imperfection would impact the emissivity. Therefore, here we consider the randomness effect by adding random displacement to each fiber of the perfect array as in Figure 22a. The randomness is quantified as the standard deviation of the random displacement (Gaussian distributed) divided by the pitch. A randomness of 10% mean that the standard deviation of the random displacement is 10% of the array pitch. Figure 23a shows the array becomes visually messy when it comes to a randomness of 25%. We simulate the array under in-plane randomness from 0% to 30% with a fixed fiber pitch that corresponds to the peak emissivity. It is found that the variation of peak emissivity is less than 10%. We also consider the axial randomness effect by helically twisting the fiber (Figure 22b). The helix radius is fixed for all the fibers, but the twisting angle is random. In this case, the variation of peak emissivity is less than 2%.

In the above simulation on patterned fiber arrays, it has demonstrated a large emissivity tuning range. To obtain a better understanding, we simulate fabric consisting of two structural levels: it has six layers of yarns and each yarn is identical with a patterned fiber array, which is closer to the realistic fabric structure. Although the patterned fiber array is not perfectly periodic within the yarns, it is designed to be nearly a close-packed structure. Figure 24a is the FDTD simulation area, and the shown six yarns with periodic boundary conditions on the two sides (top and bottom) can simulate six layers of yarns. Figure 24b shows a clear emissivity dependence in the fabric, which is similar as discussed above.

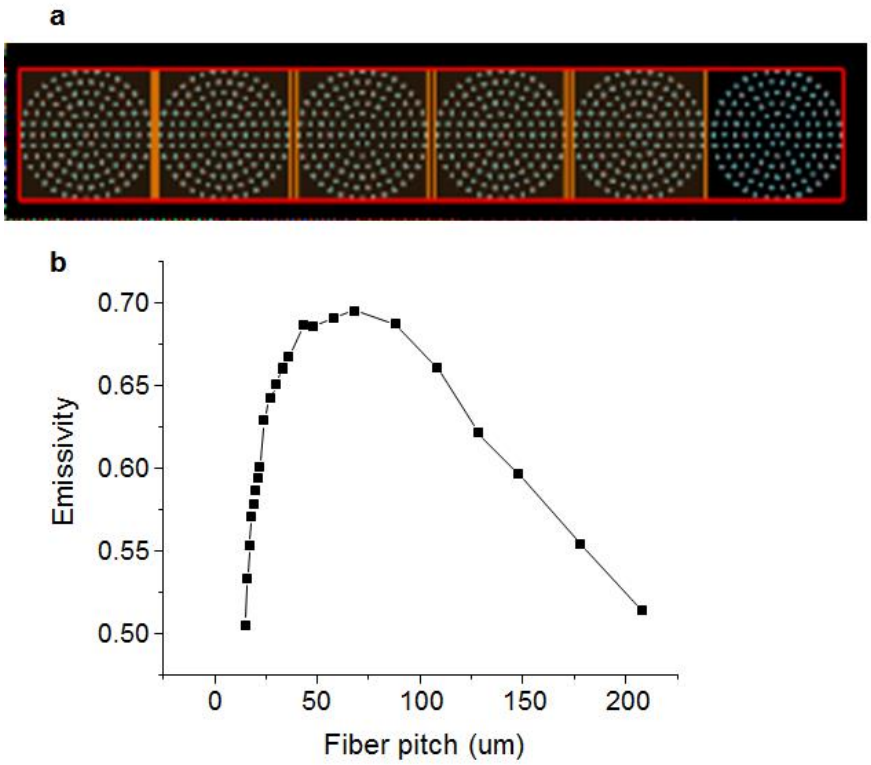

Figure 24. FDTD simulation of six layers of yarns consisting of CNT coated fibers. (a) the setup of FDTD simulation area. Six yarns with periodic boundary conditions on the top and bottom sides can simulate six layers of yarns. (b) Emissivity dependence on the fiber pitch.

4.4 Conclusion

In summary, we have proposed patterned arrays as metamaterials for thermal management. Micropillar patterned arrays have been demonstrated experimentally by 3D laser printing, and with FTIR spectroscopy and thermal imaging, we have discovered the structural dependence of the arrays' characteristic resonance and emission properties. Our FDTD simulation shows a good agreement with the experimental results. Further based on the idea, we numerically study the fiber arrays that is a typical form in textile. There is a similar structural dependence of the arrays' characteristic resonance and we also find the arrays' properties will not be largely

compromised even in the imperfect patterns which are common in real life. This study provides new perspectives on metamaterials for thermal management and the textile industry[57,151,152].

Chapter 5: Chiroptics in inorganic nanocrystals

5.1 Introduction

5.1.1 Background

Chirality, or handedness, is an important geometric attribute of nature that is observed in its various forms with lack of mirror symmetry[153,154]. The significance of chirality of matter has been addressed in various fields, ranging from understanding the evolution of life processes, to enantioselectivity in chemical reactions, to the recent discovery of unusual large spin polarization through chiral organic molecules for spin chemistry and devices[155-157]. The most common examples of chiral entities studied so far are small organic molecules that possess, for example, an asymmetrically substituted carbon atom in an sp^3-hybridized carbon skeleton. When these microscopic monomeric organic chiral units are assembled as building blocks to form higher-order meso-, or macroscopic aggregates, chirality can be expressed as observables at various length scales via a cooperative effect due to intra- and inter-molecular chirality interactions among primary chiral units[92,158].

While such cooperative chirality phenomena extensively exist in the biomolecular world, related studies in inorganic systems have been lacking. As compared with biological and organic systems, inorganic materials can often offer much better control of periodicity and morphology[159], thus representing unique test beds to understand and

tailor cooperative chirality at different length scales. A series of inorganic crystals have been found to possess helical atomic arrangement along certain crystallographic directions, leading to crystallographic chirality in a periodic lattice[160-164]. Therefore, achieving independent control of critical chiral parameters of both lattice and morphology in an inorganic structure should be the key to understanding and controlling its cooperative chirality, but has posed significant challenges because it requires synthetic control at different length scales. For example, recent attempts to control both lattice and morphology chirality in one-pot synthesis of colloidal selenium and tellurium nanostructures have only led to observation of optical activity dominated by chiral shape with an absence of chiral lattice contribution in both theoretical modeling and experiments[94].

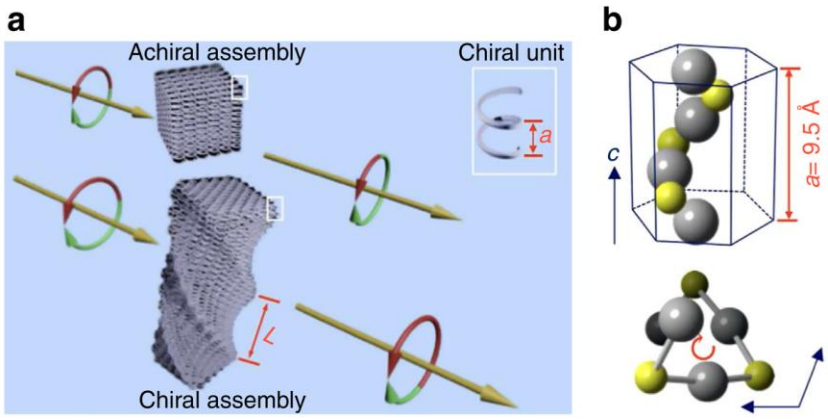

Figure 25. Cooperative chirality at different length scales. (a) Schematic model of nanoscale assembly of chiral units with characteristic length *a* (highlighted by white rectangle). Such assemblies can possess either achiral or chiral morphology with characteristic length *L*, leading to different chiroptical response. (b) Atomic model of cinnabar HgS lattice along crystallographic *c*-axis, showing helical arrangement of atoms. (Top) Side view. (Bottom) Top view. Gray sphere, Hg atom. Yellow sphere, S atom.

5.1.2 Cooperative chirality and synthetical efforts

A schematic of chirality expressed at different length scales is shown in Figure 25a, and can be omnipresent in diverse systems (biological, biomimetic and inorganic systems). The primary chiral units can be chiral molecules or chiral unit cells in solid state, and the overall chirality beyond atomic and molecular scale should be considered as various cooperative chiral interactions among primary chiral units. Figure 25b shows one example of cinnabar α-HgS lattice with a space group of $P3_221$, in which Hg and S atoms are arranged in a helical form along crystallographic *c*-axis[165]. This offers a natural atomic scale primary chiral unit, and the assembly of such atomic scale chiral entity (that is, periodic lattice in solid) is analogous to higher-order biological system and should manifest cooperative chirality.

We have developed a novel epitaxy-based two-step synthetic scheme to achieve independent control of crystallographic and geometric chirality in an inorganic nanostructure, and we employ cinnabar α-HgS as an example to demonstrate versatile control and to explore enabled chirality interplay originating from primary atomic lattice and higher-order morphology with in-depth structural and optical characterization. This synthetic paradigm can allow precise tailoring of chirality at different length scales with a high degree of freedom of control by versatile combination of crystallographic and geometric handedness, thus opening up exciting opportunities to study and gain insight into unique cooperative chirality in an inorganic system.

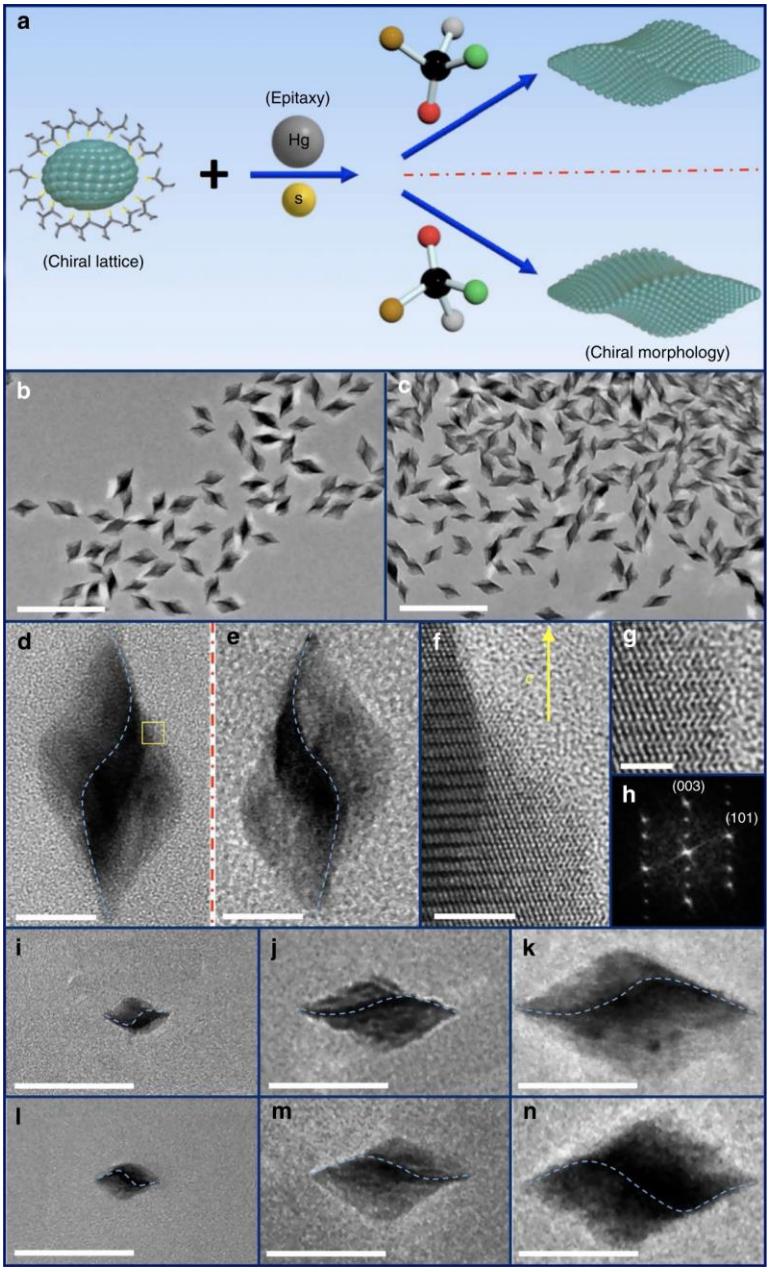

Figure 26. Two-step synthesis for controlling crystallographic and geometric handedness. (a) Schematic of the growth process based on epitaxial principle with involvement of chiral molecule to tailor the chirality of morphology. (b and c) Large-scale TEM image of as-synthesized α-HgS nanostructures with $(+)_C$-P and $(+)_C$-M nanostructures by following synthetic route in a, respectively. Scale bar, 200 nm. (d and e) Typical TEM images of prevailing individual nanostructures from b and c, respectively. Blue dashed curves are added to guide the eyes for different twisting orientation in a nanostructure. Scale bar, 20 nm. (f) High resolution TEM image of selected yellow area in d. Helical atomic arrangement along crystallographic *c*- axis can be unambiguously identified, as illustrated in Figure 25b. Scale bar, 5 nm. (g) Better resolution to reveal feature of helical atomic arrangement. Scale bar, 2 nm. (h)

Fourier transform of TEM image, confirming assignment of crystallographic axis. (i-n) TEM images of $(+)_C$-M (i-k) and $(+)_C$-P (l-n) α-HgS nanostructures with different size. Blue dashed curve is added to guide the eyes for different twisting orientation in a nanostructure. Scale bar, 100 nm.

Experimentally, while there exist a number of studies on control of either crystallographic or geometric chirality[75,78,83,90,94,166-168], simultaneous and independent control of both chiral factors in a nanostructure has posed intimidating synthetic challenges, but represents a prerequisite in order to understand and even control their interplay. We have developed a solution phase two-step synthetic method by combining homo-epitaxial growth with atomic scale regulation of morphology through a chiral molecular modifier, with the key steps of our synthetic control scheme illustrated in Figure 26a. The chemical synthesis is developed by Dr. Peng-peng Wang in our group and the details are revealed in the published work[112].

Briefly, small single crystalline α-HgS nanocrystals with well-defined crystallographic handedness are applied as seeds in the synthesis, followed by slow co-addition of Hg and S precursors to enable successive ion layer adsorption and reaction onto the seeds at the presence of excess enantiopure molecules as chiral molecular modifiers of morphology[169]. Because of the epitaxial synthetic condition, the seed nanoparticle acts as a chiral lattice template, in which the addition of precursor atoms follows the existing chiral lattice structure defined by the seeds, therefore determining the crystallographic chirality of epitaxially grown nanostructures. However, the addition of surrounding chiral molecules (such as *D*- or *L*- penicillamine molecules) in solution can play a pivotal role in surface reconstruction/reshaping, by acting as

molecular chiral modifier through the interaction with surface atoms during the epitaxial growth to transmit their handedness into the morphology of nanostructures and to allow independent geometric control at larger length scale.

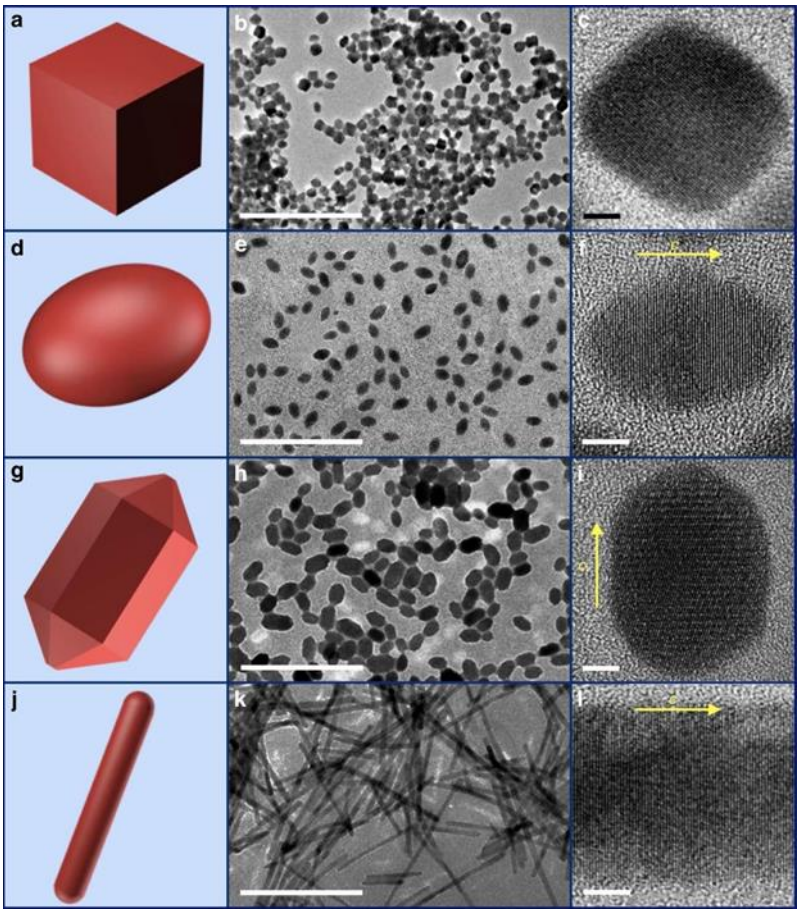

Figure 27. The α-HgS nanostructures with chiral lattice ($(+)_C$) but various achiral morphology. (a, b and c) Model, typical large- scale TEM image and high- resolution TEM image of nanocubes, respectively. (d, e and f) Model, typical large- scale TEM image and high- resolution TEM image of nanoellipsoids, respectively. (g, h and i) Model, typical large- scale TEM image and high- resolution TEM image of nanorods, respectively. (j, k and l) Model, typical large- scale TEM image and high- resolution TEM image of nanowires (denoted as "Nanowires 1"), respectively. More nanowires with different aspect ratio are provided in Figure 36. The yellow arrow in f, i and l represents crystallographic *c*-axis of α-HgS. Scale bar for large-scale TEM images, 200 nm. Scale bar for high- resolution TEM images, 5 nm.

Following the synthetic scheme illustrated in Figure 26a, we have started with small α-HgS nanocrystals as seeds by a modified enantioselective synthesis[90]. The α-HgS seeds from this enantioselective synthesis can possess different lattice chirality with the same achiral morphology, which show a mirrored circular dichroism (CD) response (see Figure 28), and are denoted as $(+)_C$ and $(-)_C$ based on their CD features for the rest of discussion to represent the two different crystallographic handedness, respectively. In the succeeding epitaxial growth process, we have utilized *D*- and *L*- penicillamine molecules as exemplary molecular chiral modifiers to demonstrate control of morphological chirality, but different chiral molecules can also be available and employed to maximize such synthetic control. Figure 26b and c show two typical large-scale TEM images of epitaxially grown α-HgS nanostructures, which are grown from the same seed nanoparticles possessing crystallographic lattice chirality of $(+)_C$, but with the incorporation of two penicillamine enantiomers as chiral morphology modifiers during the epitaxial growth process, respectively. Both results show that the addition of penicillamine molecules in the epitaxial growth process has unanimously led to twisted triangular bipyramid nanostructures with narrow size distribution (average length and aspect ratio of nanostructures in both samples are 76.9 ± 5.8 nm and 1.90 ± 0.15, respectively). However, the prevailing handedness of twisting in morphology from both samples is different. Two high-resolution TEM images are presented and compared in Figure 26d and e to highlight dominant morphology from the samples in Figure 26b and c, respectively.

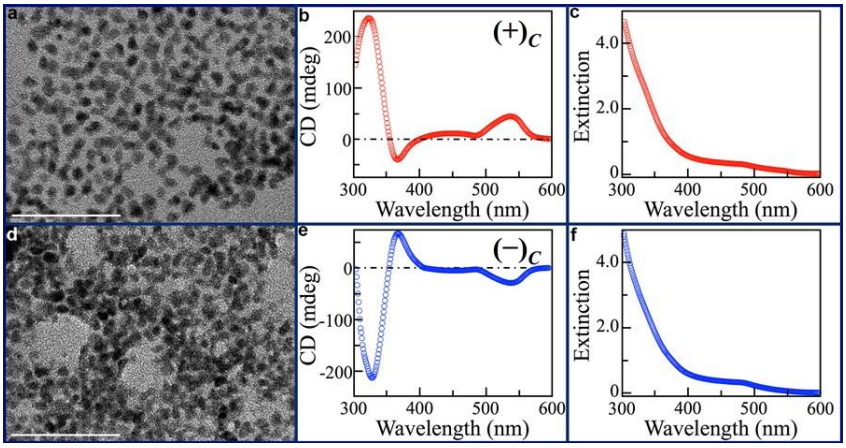

Figure 28. Seed α-Hg nanoparticles possessing crystallographic handedness. (a-c) Typical large- scale TEM image, CD spectroscopy and extinction spectroscopy of $(+)_C$-seed nanoparticles, respectively. Scale bar, 100 nm. (d-f) Typical large scale TEM image, CD spectroscopy and extinction spectroscopy of $(-)_C$- seed nanoparticles, respectively. Scale bar, 100 nm.

A few features can be immediately identified. First, both samples show twisted triangular bipyramid morphology. To further confirm such triangular bipyramid structures, we have performed three-dimensional (3D) tomographic imaging and reconstruction in TEM with side and top views, respectively[112]. A clear three-fold symmetry and twisted structure can be identified. By comparing with structural modeling, the twisting angle can be determined to be $\theta = 65.3 \pm 3.5°$ (Figure 29). Second, even though these two samples were grown from the same chiral $(+)_C$ -seed nanoparticles, their twisting orientations (i.e. geometric handedness) are prevailingly different, and their morphologies show non-superimposable 3D mirror relationship (Figure 26d and e). Based on the twisting direction relative to the c-axis, we can assign the geometric handedness of structures in Figure 26d and e as P and M, respectively. Third, our XRD characterization confirms the as-synthesized nanostructures possess cinnabar lattice structures. Figure 26f and g show atomic resolution images and its

corresponding Fourier Transform image (Figure 26h), determining the long axis of twisted nanoparticles is along c-axis of cinnabar structure and, importantly, the helical lattice arrangement as schematically shown in Figure 25b is unambiguously revealed by HRTEM for the cinnabar lattice. And last, we have also performed similar epitaxial synthesis with $(-)_C$-seed nanoparticles possessing opposite crystallographic chirality (i.e., $(-)_C$-M and $(-)_C$-P. We have found that the prevailing morphology from similar epitaxial synthesis is indeed determined by the chiral molecules utilized during the epitaxial growth and is independent of the crystallographic chirality of the seed nanoparticles. Our synthetic scheme in a can therefore allow independent control of crystallographic and geometric handedness, by controlling the seeds and the follow-up epitaxial growth in a two-step solution process.

To illustrate the effect of geometric morphology on cooperative chirality, we have also synthesized a series of α-HgS nanostructures possessing crystallographic chirality but different achiral morphology, with four examples (nanocubes, nanoellipsoids, nanorods and nanowires) highlighted in Figure 27. All the nanostructures summarized in Figure 27 possess uniform size and well-defined achiral morphology without twisting, which are different from those in Figure 26. Together with the chiral morphologies presented in Figure 26, all our synthetic controls achieved so far can allow systematic study of the evolution of cooperative CD with critical structural parameters and can facilitate our understanding of the interplay between crystallographic and geometric handedness in the chiroptical properties of inorganic nanostructures.

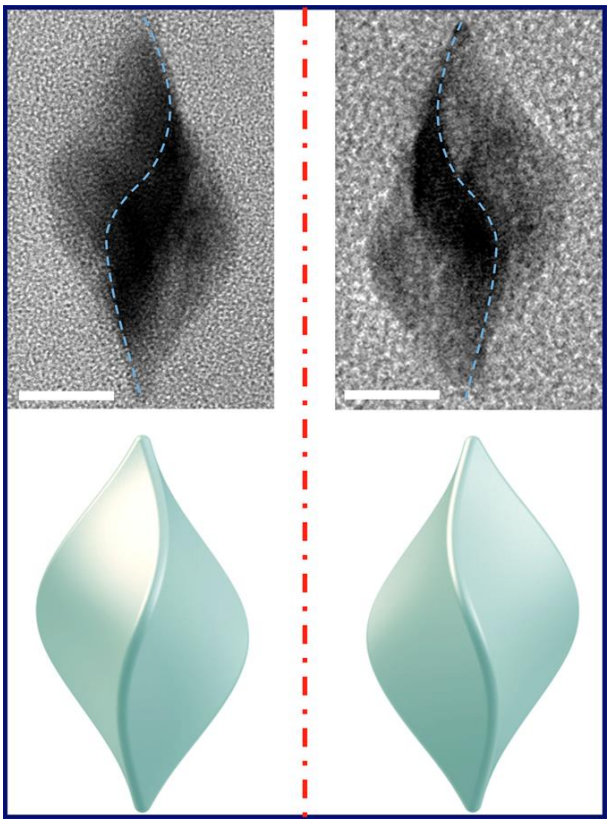

Figure 29. Structural models of two mirrored α-HgS nanostructures in Figure 26d and e. TEM images are the same as presented in Figure 26d and e, respectively. Scale bar, 30 nm.

By performing systematic circular dichroism (CD) measurements on samples with different combinations of crystallographic and geometric chirality, evolution of cooperative chirality can be revealed at multiple levels of inorganic nanostructures. We further adopt an electromagnetic core-shell model with the finite element method (FEM) that can allow computation and prediction of cooperative chirality, showing excellent agreement with our experimental results and clear elucidation of nanoscale chirality interplay. Importantly, both the synthetic scheme and theoretical model in our

current work are universal for exploring cooperative chirality and can be readily applied for other inorganic materials that possess a chiral symmetry group. This work can therefore enable an emerging class of inorganic nanostructures with pre-designed cooperative chirality that not only allows fundamental understanding and control of chirality at different length scales, but also provides functional building blocks with engineered handedness to achieve chirality-dependent chemical and physical processes as well as large-scale meta-devices with new chiroptical effects[170-173].

5.2 Basic theory

Optical response of a matter that possesses both crystallographic chirality and morphological chirality can be described by the combination of Maxwell's equations and constitutive equations[104,174]. The Gaussian (CGS) units are applied in our model and computation.

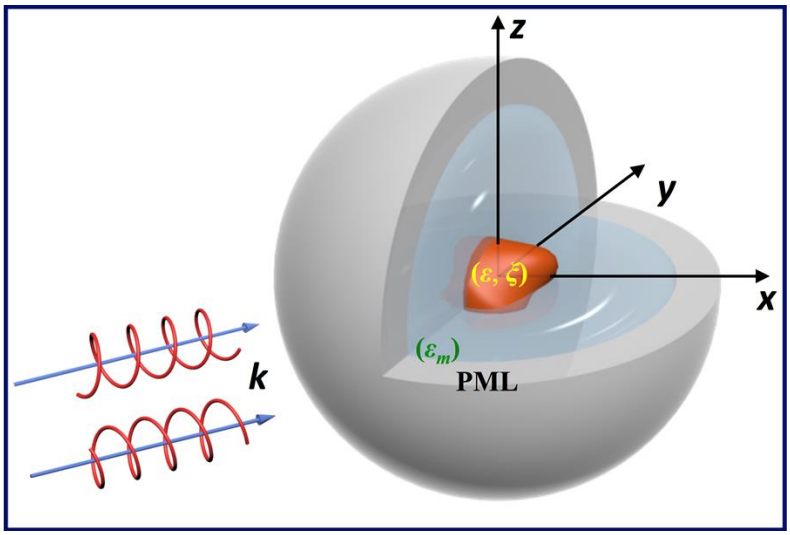

Figure 30. Electromagnetic core-shell model for computing chiroptical response of a chiral nanostructure with arbitrary morphology. A chiral nanostructure with arbitrary morphology and parameters of (ε, ξ) is placed in the origin as core. The chiral

nanostructure is encapsulated by an achiral spherical shell with dielectric constant of ε_m, whose size is much bigger than chiral core to simulate the environmental medium. Since our circular dichroism (CD) measurement is always performed in an achiral solvent (such as water), chiral parameter ξ_m of media is always set to be zero. A perfectly matching layer (PML) boundary condition is applied to the outermost surface of environmental shell in a finite element method (FEM) simulation. Optical response of chiral nanostructure in the model is computed under illumination of left and right-circularly polarized plane waves with incident wave vector k. To compare with our experiment, computed CD spectra are averaged over all k directions.

Our core-shell model (see Figure 30) incorporates a crystalline lattice with arbitrary geometric shape (either chiral or achiral) as core particle, which is embedded in a spherical non-chiral dielectric environmental matrix shell. The dimension of non-chiral dielectric matrix is typically much larger than that of chiral nanostructure to account for the environmental media for CD measurement. In general, the interaction between electromagnetic wave and matter is describable in terms of a set of parameters, (ξ, ε, μ)that relate the fields $\vec{D}$ to $\vec{E}$ and $\vec{B}$ to $\vec{H}$ via the constitutive relations, where χ is chiral parameter that quantifies chiral asymmetry (that is, rotation of the plane of polarization when monochromatic electromagnetic wave passes through chiral media), e is dielectric function, and n is relative permeability. The system is excited by the external monochromatic electromagnetic wave with frequency w, in which the electric and magnetic field components, $\vec{E}$ and $\vec{H}$ at location $\vec{r}$ have a time dependence given by the factor $\exp(-i\omega t)$:

$$\begin{cases} \vec{E}\left(\vec{r}\right) = \vec{E}_0 e^{i(\vec{k}\cdot\vec{r}-\omega t)} \\ \vec{H}\left(\vec{r}\right) = \vec{H}_0 e^{i(\vec{k}\cdot\vec{r}-\omega t)} \end{cases}$$

where $\vec{k}$ is incident wave vector, $\left|\vec{E}_0\right|$ and $\left|\vec{H}_0\right|$ are maximum amplitude of electric and magnetic fields, respectively. To perform a FEM simulation, a perfectly matched layer (PML) is also added in our model as the outermost shell to absorb the launched waves at the boundary of the dielectric medium, which simulates an infinite environment and helps truncate computational domains.

In our current model, we treat all our nanostructures as isotropic non-magnetic chiral media, in which the constitutive equations can be given by[175,176]:

$$\begin{cases} \vec{D} = \varepsilon_{BPE}\vec{E} + i\xi\vec{B} \\ \vec{H} = \mu_{BPE}^{-1}\vec{H} + i\xi\vec{E} \end{cases}$$

where ε_{BPE} is the Bassiri-Papas-Engheta dielectric function and is related to $\varepsilon_{BPE} = \varepsilon - \xi^2\mu$, and $\mu_{BPE} = \mu$. In our model, we therefore adopt above constitutive relations with ε and n independent of the chiral parameter χ. This can allow us to evaluate chirality originating from crystallographic and geometric effects independently. Furthermore, we consider only isotropic chiral lattice, that is, the χ is isotropic. While in principle the χ should be anisotropic depending on symmetry group of a lattice, as a first order approximation, assumption of isotropy can simplify calculation as well as determination of parameters, and allow us to address basic physics behind, but in the future, more accurate description of anisotropic χ should further improve modeling. Since materials of interest in our current study are non-magnetic, we can have n for both chiral media and dielectric matrix as the constant of 1 [85,175,177]. For the achiral dielectric matrix surrounding the chiral media, we also have $\xi_m = 0$ and $\varepsilon_m = \sqrt{n_m}$,

where n_m is its refractive index. In our computation, the thickness of PML shell is set to be λ/n_m to absorb the launched electromagnetic wave at the boundary of environmental dielectric matrix, where λ is the wavelength of incident electromagnetic wave.

The time-averaged Poynting vector (energy flux density) is given by[6,104]:

$$\left\langle \vec{S} \right\rangle = \frac{1}{2}\mathrm{Re}\left[\vec{E}\left(\vec{r},\omega\right) \times \vec{H}^{*}\left(\vec{r},\omega\right) \right]$$

Thus the energy flux density of scattered field through a given surface with a normal unit vector $\vec{n}$ is given by:

$$\left\langle S_{scat} \right\rangle = \left\langle \vec{S}_{scat} \right\rangle \bullet \vec{n} = \sum_{i=x,y,z} n_i \left\langle S_{i,scat} \right\rangle$$

Therefore, the absorption, scattering and extinction cross sections can be determined by[178]:

$$\sigma_{abs} = \frac{1}{\langle S_0 \rangle} \iiint_V Q dV$$

$$\sigma_{scat} = \frac{1}{\langle S_0 \rangle} \iint_S \langle S_{scat} \rangle dS$$

$$\sigma_{ext} = \sigma_{abs} + \sigma_{scat}$$

where Q is the dissipative loss density, the integral volume V is the whole physical region (by summing volume of environmental matrix and central chiral media), the integral surface S is the interface between physical region and PML, $\langle S_0 \rangle$ is the time-averaged energy flux density of background plane wave that is equal to $\left\langle S_0 \right\rangle = \frac{1}{2}\frac{n_m \left|\vec{E}_0\right|^2}{Z_0}$, where n_m is the refractive index of core and Z_0 is the characteristic impedance of vacuum.

In order to evaluate frequency-dependent CD response, the extinction cross sections of the chiral media under illumination of left and right-handed circularly polarized plane waves, σ_{ext}^{+} and σ_{ext}^{-}, are computed independently, and then the CD spectrum can be evaluated by $CD(\omega) = \sigma_{ext}^{+} - \sigma_{ext}^{-}$. Since our optical measurement is an ensemble measurement, the CD resulted from all directions of $\vec{k}$ needs to be averaged around the chiral media when comparing with experimental results.

5.3 Parametric modeling

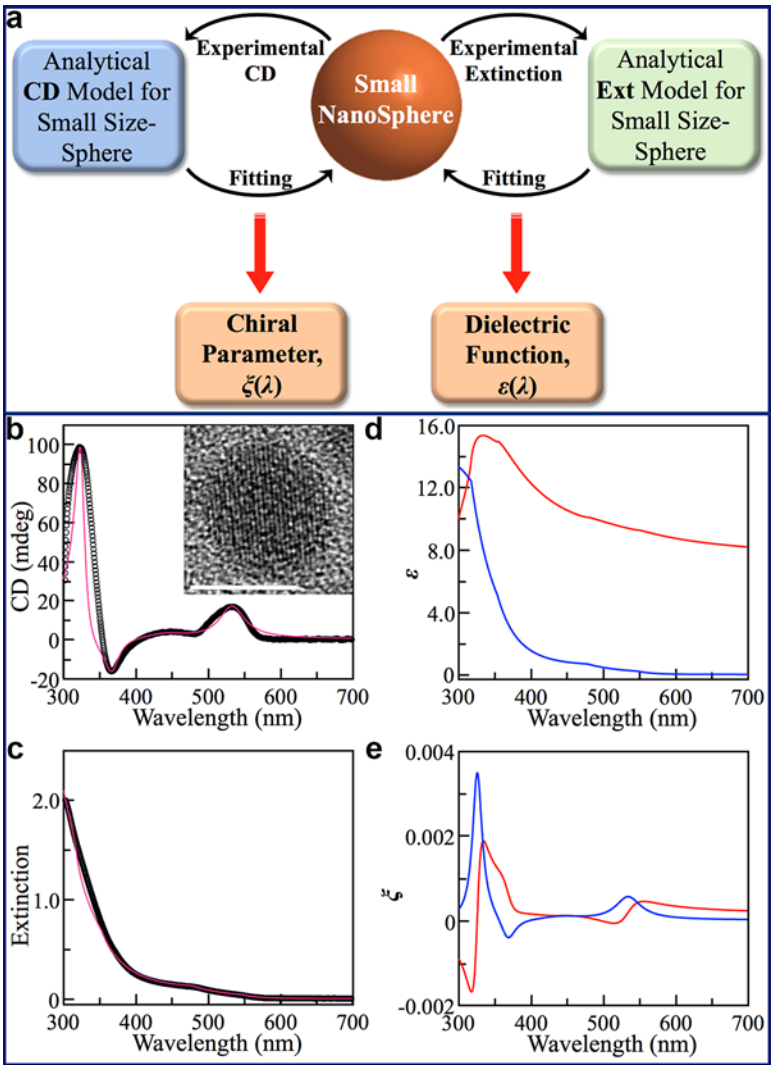

Figure 31. Parametric modeling of materials parameters (ε, ξ) of a chiral nanostructure. (a) Schematic of parametric modeling. The key is to acquire CD and absorption spectra of small sized spherical chiral nanoparticles and fit with corresponding analytical solution to extract parameters (ε, ξ). (b) and (c), Experimental (black sphere) and fit (pink curve) spectra of CD and absorption of 12 nm- sized HgS nanoparticles, respectively. (Inset) of b, A typical transmission electron microscopy (TEM) image of a single α-HgS nanoparticle for acquiring experimental data, showing quasi- spherical morphology. Scale bar, 10 nm. d and e, Imaginary (blue) and real (red) parts of parameters ε and ξ of α-HgS, respectively, which are obtained based on fits in b and c.

One of the keys for computation with the model described is to determine parameters set for chiral nanostructures, which might not be always available. Figure 31a shows a

general self-consistent approach to determine (ξ, ε) of a non-magnetic chiral material ($\mu = 1$) from experimental results. This approach is based on the fact that analytical solution of absorption and CD spectrum for nanoparticles with small size and spherical morphology can be available to compare with related experimental results for parameter fitting. For example, for a small sized spherical particle, theoretical absorption cross section can be given by[85,179]:

$$\sigma_{abs} = B\omega \mathrm{Im}(\varepsilon_r(\omega)) \left| \frac{3\varepsilon_m}{2\varepsilon_m + \varepsilon_r(\omega)} \right|^2$$

where $B = \frac{V}{c\sqrt{\varepsilon_m}}$ is a constant (c is speed of light). The dielectric function of chiral nanoparticles ε_r, is a complex number given by $\varepsilon_m = \varepsilon_1 + \varepsilon_2$. The imaginary part can be described by a modified Tauc-Lorentz model (that is, combination of Tauc joint density of states with the Lorentz oscillator)[180,181]. When only a single inter-band transition is considered:

$$\varepsilon_2(E) = \begin{cases} \left(\frac{e_0}{E}\right) \cdot \frac{F(E-e_t)^2 \Gamma}{(E^2 - e_0^2)^2 + \Gamma^2 E^2}, & (E > e_t) \\ \left(\frac{C_1}{E}\right) \cdot \exp\left(\frac{E-e_t}{e_u}\right), & (E \le e_t) \end{cases}$$

where e_t is demarcation energy between the Urbach tail transition and the inter-band transition, e_u is the Urbach width describing absorption tail associated with inter-band transition, e_0 is the resonant energy of chiral nanoparticles, F and Γ are Lorentz oscillator amplitude and width, respectively. C_1 is a fitting parameter to ensure

continuity of dielectric function at $E = e_t$. This modified Tauc-Lorentz model can be extended for the scenario of multiple oscillators, with the example discussed below.

Once the imaginary part of dielectric function can be available, the real part ε_1 can be acquired based on the Kramers-Kronig relation[104,182]:

$$\varepsilon_1 = 1 + \frac{1}{\pi}\beta \int_{-\infty}^{\infty} \frac{\varepsilon_2(\omega')}{\omega' - \omega} d\omega' = 1 + \frac{2}{\pi}\beta \int_{0}^{\infty} \frac{\omega'\varepsilon_2(\omega')}{\omega'^2 - \omega^2} d\omega'$$

where b denotes the principal value of the integral. By comparing experimental data acquired from small sized spherical nanoparticles with analytical solution of σ_{abs}, a materials-dependent dielectric function parameter ε_r can thus be determined.

In addition to the absorption, the CD response of a very small size chiral nanoparticles with spherical shape in a dielectric matrix (ε_m) can be expressed as[5,9]: $CD = CD_\xi + CD_\varepsilon$. The CD_ξ and CD_ε can be determined by

$$CD_\xi = A * \mathrm{Im}(\xi) \frac{\mathrm{Re}(2\varepsilon_m + \varepsilon_r)}{|2\varepsilon_m + \varepsilon_r|^2}$$

$$CD_\varepsilon = -A * \mathrm{Im}(\varepsilon_r) \frac{\mathrm{Re}(\xi)}{|2\varepsilon_m + \varepsilon_r|^2}$$

where $A = 8\omega\left|\bar{E}_0\right|^2 \varepsilon_m^{3/2} R^3$ is a constant and *R* is the radius of the nanoparticle. Here, we setup a multi-oscillator model for fitting:

$$\xi(\omega) = \sum_j \frac{a_j}{E - e_j + i\Gamma_j}$$

Therefore, by comparing theoretical CD with experimental result of small sized chiral nanoparticle, chiral parameter, χ can be therefore determined.

The parametric model as described above can be used to determine material-dependent parameters of optical function in a general manner. We use HgS as an example to illustrate our approach step-by-step to determine all parameters for computation of nanoparticles with achiral and chiral shape in current study, and we have also compared results from our approach with other techniques to substantiate our approach. To validate our approach, we have synthesized small size α-HgS nanoparticles with quasi-spherical nanoparticles and measured their absorption and CD spectra to compare with analytical expressions (see Figure 31b and c). According to Tauc-Lorentz model, the fitting imaginary part of dielectric function of HgS is modeled by two oscillators and expressed as following:

$$\varepsilon_2(E)=\begin{cases}\dfrac{e_0}{E}\dfrac{F\left(E-E_g\right)^2\Gamma}{\left(E^2-e_0^2\right)^2+\Gamma^2E^2}, & \left(E\geq e_{t1}\right)\\ \dfrac{e_1}{E}\exp\left(\dfrac{E-e_{t1}}{E_{u1}}\right), & \left(e_{t2}\leq E\leq e_{t1}\right)\\ \dfrac{e_2}{E}\left[0.93\exp\left(\dfrac{E-e_{t2}}{e_{u2}}\right)+0.07\right], & \left(e_{t3}\leq E< e_{t2}\right)\\ \dfrac{e_3}{E}\exp\left(\dfrac{E-e_{t3}}{e_{u3}}\right), & \left(e_{t4}\leq E< e_{t3}\right)\\ \dfrac{e_4}{E}\exp\left(\dfrac{E-e_{t4}}{e_{u4}}\right), & \left(0< E\leq e_{t4}\right)\end{cases}$$

The fit parameters from the Tauc-Lorentz model are shown in Table 2. We also present our fitted dielectric function ε_1 and ε_2 in Figure 31d. We would like to point

out that our fitted dielectric function agrees well with previous experimental values of cinnabar and parameters from DFT calculation[179,183].

Fitting Parameters for θ			**Fitting Parameters for χ**			
i	e_{ti}/eV	e_{ui}/eV	i	e_i/eV	Γ_i/e_i	$a_i/(\frac{10^{-5}}{\Gamma_i})$
1	3.9	0.4	**1**	2.32	0.04	-0.467
2	3.5	0.26	**2**	2.8	0.08	-0.4
3	2.59	0.25	**3**	3.37	0.035	0.8
4	2.26	0.08	**4**	3.81	0.025	-3.2

Table 2. Optimized parameters of (ξ, ε) of α-HgS

We have also presented fitted imaginary and real parts of chiral parameters of HgS in Figure 27. We would like to highlight that our fitted chiral parameters are in the same range of previous literatures[179] . All these agreements together validate our parametric modeling method.

5.4 Modeling and simulation of chiral nanocrystals

5.4.1 Structural model

Figure 32 shows the general method to build a chiral object from an achiral object by a linear twist. The plot shows a right-handed twist (resulting in P morphology). The twisting angle of a selected cross-section plane along the axis is proportional to the

distance between this plane and the bottom plane, d, as $\theta_d = -(d/L)\theta$. For a left-handed twist (resulting in M morphology), the twisting angle is defined to be positive.

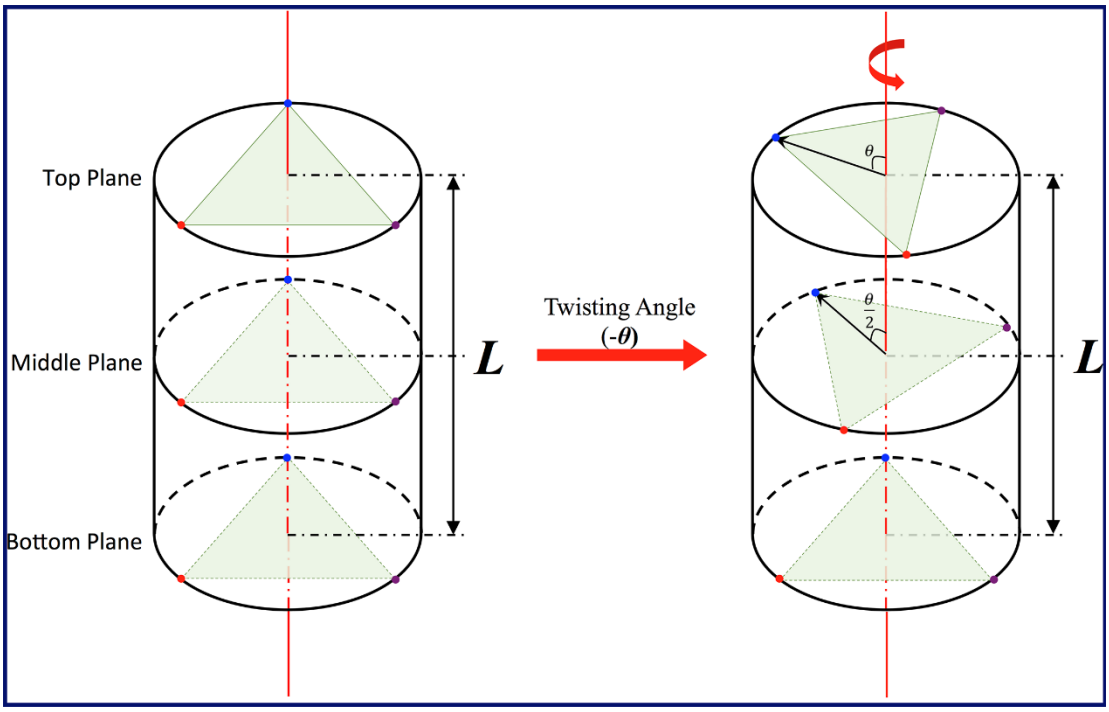

Figure 32. Structural model of twisting. Cylindrical plot of a twisted structure is applied to illustrate definition of twisting and twisting angle, θ in structural modeling.

To study the cooperative chirality, we build up an exemplar 3D model (right in Figure 33 and Figure 34) by twisting explained above in Solidworks. The length of the model is 150 nm and the aspect ratio is 1. No shape chirality (0°), small shape chirality (±10°) and large shape chirality (±80°) are presented. The structural models can be imported into COMSOL for electromagnetic simulation. The detailed CD study on the structure will be discussed in the next section.

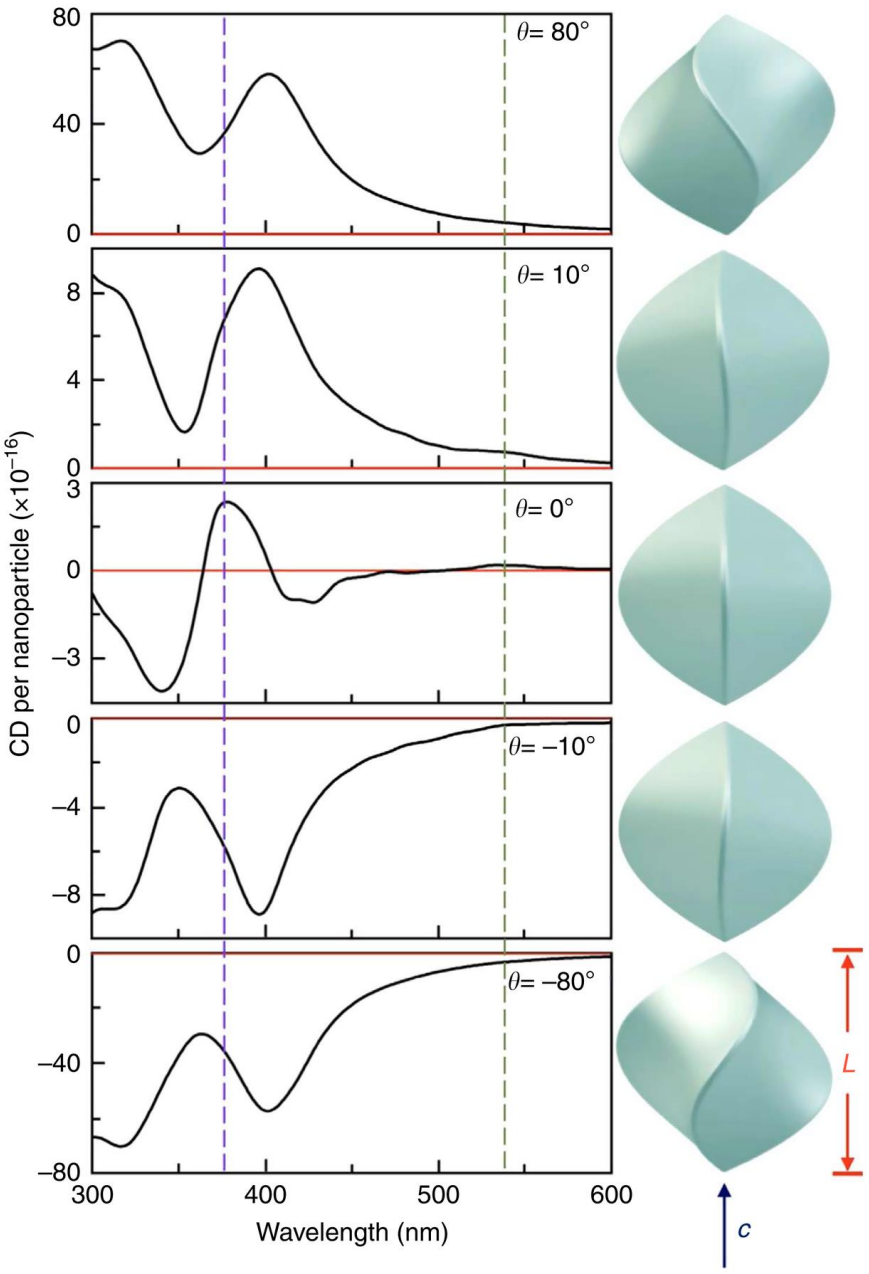

Figure 33. Cooperative chirality in the exemplar model. Computed CD spectra of a twisted triangular bipyramid α-HgS with different twisting angle, while the crystallographic chirality remains unchanged. Corresponding structural model of simulated nanostructures is presented next to its CD spectroscopy. The simulation is performed with an incident wave vector that is 30° relative to the *c*-axis of nanoparticle. Green and purple dashed lines are guides to the eyes for features near 540 nm and 380 nm, respectively. For all simulations, the *L* and aspect ratio of α-HgS nanostructures are set to be 150 nm and 1, respectively.

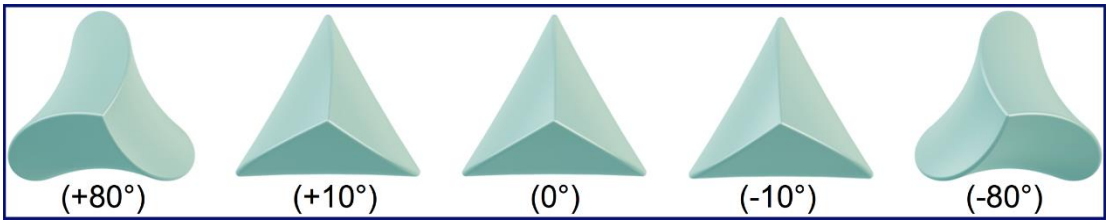

Figure 34. Top- view of triangular bipyramid structures with different twisting θ. These top-view models correspond to structures presented in Figure 33.

In the above model, the length, the aspect ratio (length/waist) and the twisting angle of the particle can also be tuned. We can easily restructure it for the synthesized chiral-shaped α-HgS nanostructures as in Figure 29, which has a length of ~85nm, an aspect ratio of ~2 and a twisting angle of 61°. For the synthesized chiral at different length, the statistical analysis of structural parameters is summarized in Table 3. And all of them are modeled for simulation.

Structure	**Length (nm)**	**Width (nm)**	**Aspect Ratio**	**Twisting Angle (°)**
2	53.6 ± 6.3	26.4 ± 2.5	2.03 ± 0.17	66.7 ± 4.9
3	76.9 ± 5.8	40.6 ± 2.7	1.90 ± 0.15	65.3 ± 3.5
4	85.5 ± 6.4	41.7 ± 2.9	2.05 ± 0.15	61.0 ± 6.0
5	144.8 ± 6.9	74.0 ± 2.6	1.96 ± 0.11	57.0 ± 6.5
6	201.2 ± 6.1	102.8 ± 6.1	1.96 ± 0.14	60.3 ± 6.7
7	271.2 ± 7.1	141.1 ± 10.2	1.93 ± 0.12	59.5 ± 4.5

Table 3. Summary of statistical analysis of structural parameters of epitaxial grown samples. Samples used for this statistical analysis are $(+)_C$-M. We have also observed that for nanoparticles grown from same seed nanoparticles (possessing either $(+)_C$ or $(-)_C$ lattice), their corresponding P and M morphologies show exactly the same structural parameters other than opposite twisting orientation (see also Figure 26d, e, i-n).

5.4.2 Cooperative chirality: exemplar model

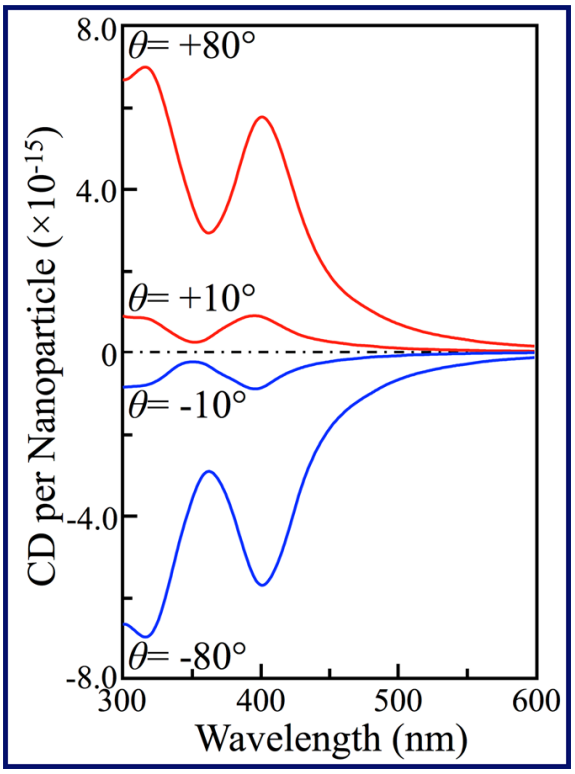

Figure 35. Computed contribution of CD response merely from chiral morphology. In order to evaluate contribution of CD response from morphological effect in Figure 33, CD spectra are computed by setting chiral parameter ξ to be zero, and all other parameters remain the same as those for Figure 33.

To explore cooperative chirality originating from the crystallographic and geometric effects, we have adopted an electromagnetic model to incorporate both crystallographic and geometric chirality in FEM simulation. Briefly, our model and computation of chiroptical response is based on Maxwell's equations with constitutive relations for continuous chiral media. The key parameters describing the property of a chiral media include the dielectric function (ε) and the chiral parameter (ξ), which can be determined via a self-consistent parametric modeling by fitting both experimental CD and

extinction measurements acquired from small sized spherical nanoparticles with corresponding analytical solutions (Figure 31). While chiroptical response induced by either lattice or morphology in an inorganic nanostructure has been separately described in existing theoretical work[85,90,94], our current computational model allows evaluation of cooperative CD features originating from both crystallographic and geometric effects at the different length scales. Figure 33 illustrates cooperative CD spectra in the ultraviolet-visible (UV-Vis) regime by using a twisted triangular bipyramid α-HgS nanostructure as an example to highlight unique opportunity to tailor CD features of inorganic materials at the nanoscale. Our definition of geometric left- (M) and right- (P) handedness of twisted nanostructures follows the convention of helix protein and P/M nomenclature (see also Figure 32 for definition of twisting angle θ)[184,185]. We have computed and compared CD spectra of a series of M and P nanostructures of α-HgS with different θ (see Figure 34 for top view of twisted triangular bipyramid nanostructures), while their size, aspect ratio and crystallographic chirality are kept the same. When the θ= 0 (this corresponds to achiral morphology with no chiral contribution from geometric morphology), our computation shows that the untwisted triangular bipyramid α-HgS nanostructure manifests two major CD resonances at 540 nm and 380 nm, which are consistent with previous observation of α-HgS nanoparticles, and can be attributed to the first and higher excitonic transitions that are determined by the periodic chiral lattice, respectively (see Figure 25)[90]. This also provides a sanity check of our modeling and simulation. By twisting in morphology along *c*-axis, geometric handedness of nanostructure can be introduced at different length scales merely determined by its size. The evolution of cooperative CD

features with θ clearly shows the interplay between the crystallographic and geometric chirality: First, we have evaluated the CD response merely contributed from the geometric morphology (this can be achieved by setting the ξ to be zero to eliminate the contribution from the chiral lattice), and presented the results in Figure 35. The well-defined CD features can be present even with $\xi = 0$; Second, as shown in Figure 35, a larger twisting angle can lead to significantly more pronounced chiral contribution from the morphology. When the θ is increased from 10° to 80° (or decreased from -10° to -80° for the right-handed twisting), the morphology induced CD signal can be enlarged by about eight fold; And last, when the twisting orientation is reversed, its geometric CD contribution is opposite and the CD components induced merely by chiral morphology show a mirror relationship (Figure 35). This is in contrast to the resultant overall CD spectra presented in Figure 32, in which the overall CD spectra computed from two opposite θ are not mirrored spectra after taking into account of both crystallographic and geometric effects. This confirms the cooperative chirality from both chiral lattice and chiral morphology.

5.4.3 Chiral interplay – experiment and simulation

We have performed and compared UV-Vis CD and extinction spectra measurements on samples with different combinations of crystallographic lattice and geometric morphology features that are exemplified in Figure 26 and Figure 27. We have first investigated the CD spectra of α-HgS nanostructures presented in Figure 27 and Figure

36, in which all samples possess the same chiral lattice, $(+)_C$, but different achiral morphologies and aspect ratios, and presented the results in Figure 39 and Figure 40.

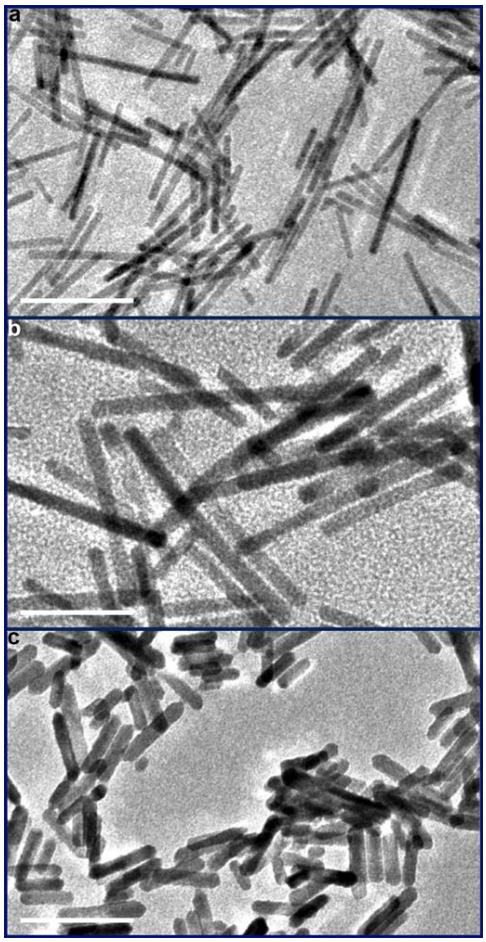

Figure 36. Typical TEM images of α-HgS nanowires ($(+)_C$) with different aspect ratios. (a) 110 nm long nanowires with 10 nm diameter (denoted as "Nanowires 2" in Figure 38a). (b) 110 nm long nanowires with 18 nm diameter (denoted as "Nanowires 3" in Figure 38a). (c) 55 nm long nanowires with 18 nm diameter (denoted as "Nanowires 4" in Figure 38a). Scale bar, 100 nm.

Qualitatively, we have found that all α-HgS nanoparticles with different achiral morphologies possess similar CD features in the UV-Vis wavelength regime. For all nanostructures with achiral morphology, two distinct CD peaks occur at the same wavelengths as those from seed nanoparticles, respectively, and can be assigned to be

associated with different excitonic states in the chiral lattice[90]. For the α-HgS nanostructures with the same achiral morphology, their CD spectra can be reversed by changing the handedness of their lattice (see Figure 37).

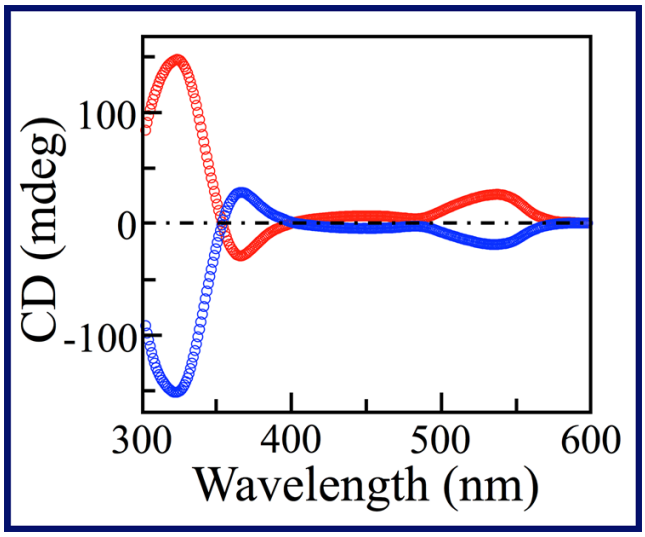

Figure 37. Experimental CD spectra of α-HgS nanocubes possessing different crystallographic handedness. (Red) nanocubes with (+)$_C$-lattice. (Blue) nanocubes with (−)$_C$- lattice.

To gain more quantitative understanding of their chiroptical properties, we have evaluated and compared the dissymmetric factor *g*, among different achiral morphologies with same crystallographic handedness. The dissymmetric factor *g* is defined as the CD spectra normalized by its corresponding extinction[157]. This *g* factor is a dimensionless quantity that represents the chiroptical response per one HgS molecular unit and can be utilized to compare among different chiral nanoparticles with elimination of a few disorder effects of nanoparticles' concentration and size variation[85,90]. Figure 38a summarizes the dissymmetric *g*-factors at different wavelengths for α-HgS nanostructures with different achiral morphologies and aspect

ratios. It can be clearly seen that when the achiral morphology or the structural aspect ratio varies, both magnitude and central wavelength of two CD peaks remain essentially unchanged. This observation further confirms that the observed CD features of α-HgS nanostructures with achiral morphology indeed originate from crystallography rather than other effects, which is also consistent with our definition and understanding of *g* factors of nanoparticle that represent chiroptical response per one HgS molecular unit. We have further computed CD and extinction spectra of $(+)_C$-HgS nanostructures with all different achiral morphology summarized in Figure 27 and Figure 36, and compared them with experimental results (see). Agreement between the experimental and theoretical results confirms negligible contribution from an achiral geometry on overall chirality, and substantiates our understanding of characteristics of *g*-factors in chiral nanostructures with intrinsic crystallographic handedness.

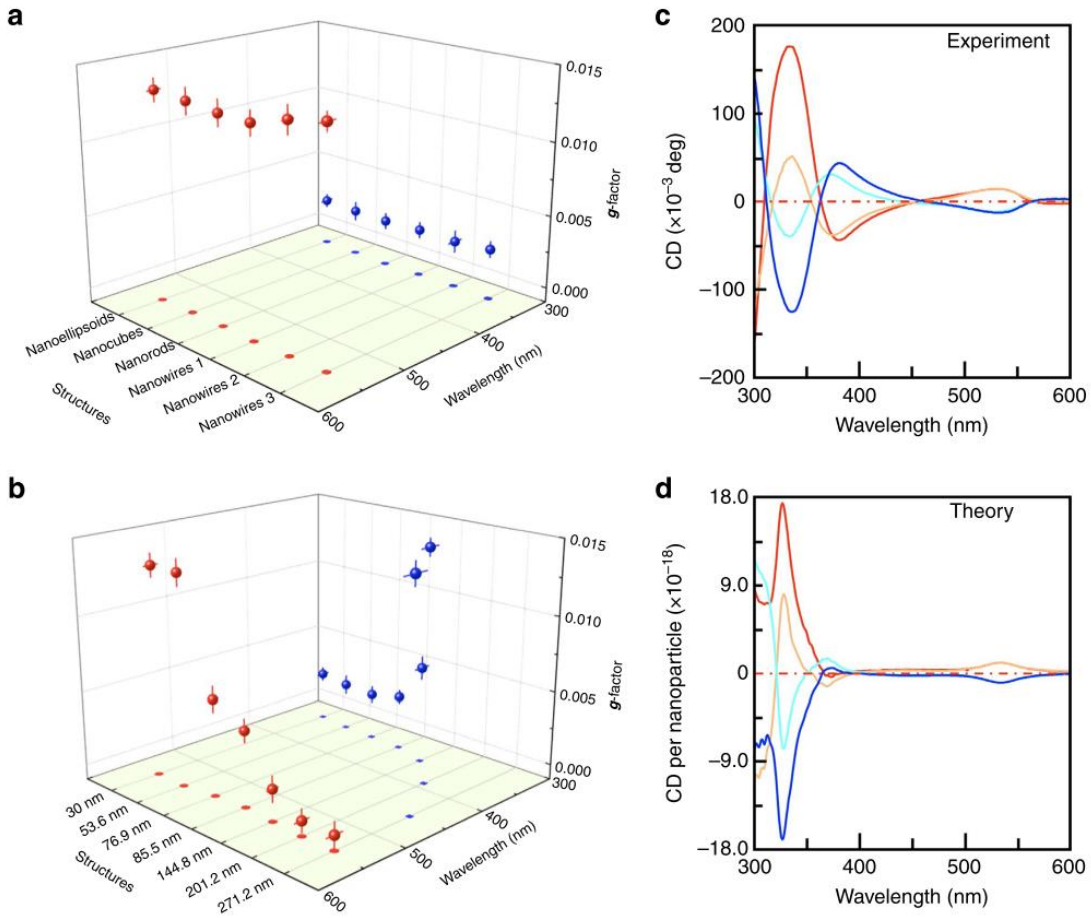

Figure 38. Chiroptical response of α-HgS nanostructures with interplay between crystallographic and geometric handedness. (a) Summary of *g*-factors of α-HgS nanoparticles, possessing chiral $(+)_C$-lattice but different achiral morphology. (b) Wavelength dependent evolution of *g*-factor peaks with size for the $(+)_C$-M twisted triangular bipyramid α-HgS nanoparticles. In a and b, projections of the *g*-factors onto the basal plane are also presented to highlight wavelength shifting of peak position. (c) Comparison of CD spectra of 85 nm long twisted bipyramid α-HgS nanoparticles with different combination of crystallographic and geometric handedness. Red, $(+)_C$-M. Orange, $(+)_C$-P. Cyan, $(-)_C$-M. Blue, $(-)_C$-P. (d) Computed CD spectra to compare with c. Color codes are assigned to be the same as those in c. The experimental dissymmetric *g*-factor and its associated error bar are determined as average and standard deviation of statistical analysis over different sample batches and different runs of measurement, respectively.

We have also performed similar CD measurements on as-synthesized twisted triangular bipyramid α-HgS nanostructures in Figure 26 that possess both

crystallographic and geometric handedness (Figure 41), and summarized the dependence of their corresponding dissymmetric *g*-factors on both wavelength and size of nanostructures (the length *L* of nanostructures along their *c*-axis is used to represent their size in the figure) in Figure 38b. By comparing with Figure 38a, a few prominent features can be immediately identified in Figure 38b: When the size of chiral nanostructures increases, the peak position of the first *g*-factor (red dots) remains almost unchanged, centering at ~ 540 nm. However, the peak position of the second *g*-factor (blue dots) is red-shifted in the spectra. In the meantime, the peak magnitude of the second *g*-factor increases as the size increases, while the peak magnitude of the first *g*-factor peaks manifests the opposite tendency. Distinct variation of the tendency of these two *g*-factors suggests that their physical origins are different. Similar to nanostructures with different achiral morphologies, the *g*-factor at 540 nm can be assigned to crystallographic chirality and is independent on morphology. On the other hand, chiral morphology can induce an additional CD response in the UV-Vis regime, which is qualitatively related to the characteristic length *L* of the twisted shape (Figure 25a). Therefore, the corresponding CD response of such twisted nanostructures in the UV-Vis regime represents competition between crystallographic and geometric handedness. As a result, when the size of nanostructures increases (thus, the *L* increases), the *g*-factor peak in this wavelength regime red-shifts (an additional electromagnetic phase retardation effect can further contribute to the red-shifting of the second *g*-factor in the spectra[178]).

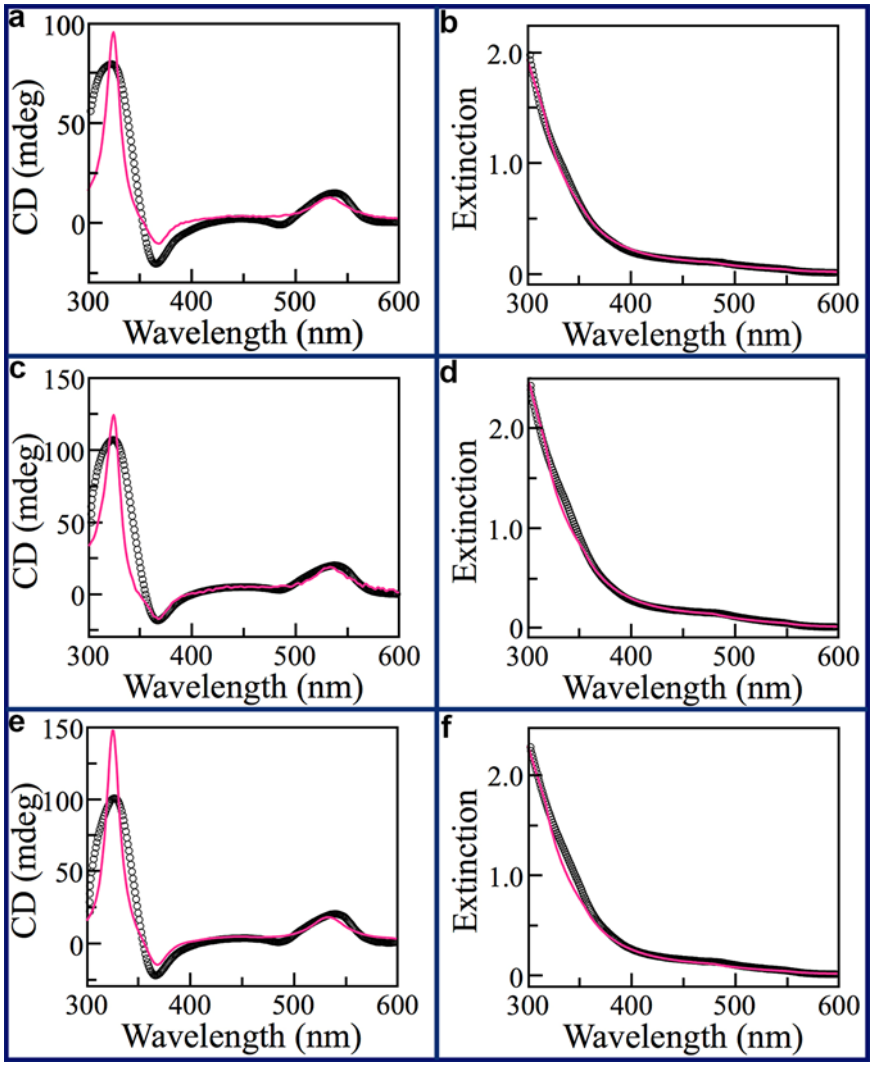

Figure 39. Comparison of experimental and computed CD and extinction spectra of $(+)_C$ HgS nanoparticles with different achiral morphologies. (a, b), (c, d), and (e, f), The CD and extinction spectra of HgS nanoparticles with nanocubic (Figure 27a), nanoellipsoidal (Figure 27d) and nanorod (Figure 27g) morphology, respectively. Black circles, experimental data. Pink curves, computed spectra.

In addition to the variation of central peak position, an increase of the size of nanostructures with chiral morphology can also result in the enhancement of the geometric chiral effect, leading to increased magnitude of the second *g*-factor peak. For example, in Figure 38b the geometric *g*-factor of larger 271 nm HgS nanoparticle is 0.0142, which is one order larger than 0.0013 of smaller 30 nm HgS. It is worth noting

that while the first *g*-factor peak at 540 nm is assigned to the crystallographic chirality and its wavelength is independent of size, the increase and red-shifting of the geometric chiral effect for larger sized nanostructures can modify the envelop of CD response induced by the crystallographic handedness. This can explain the reduced magnitude of the first *g*-factor for larger sized nanostructures, as shown in Figure 38b. In order to corroborate our experimental understanding of the chirality interplay between the crystallographic and geometric effects, we have computed CD spectra of all α-HgS nanostructures in Figure 26 that possess both chiral lattice and chiral morphology, given the structural parameters determined from our sample characterization (Table 3). By comparing the computed CD and extinction spectra with experimental results (Figure 41), our model can fully reproduce the observed chiroptical characteristics of nanostructures by incorporating both crystallographic and geometric chirality, further verifying our understanding of the chirality interplay at different length scales.

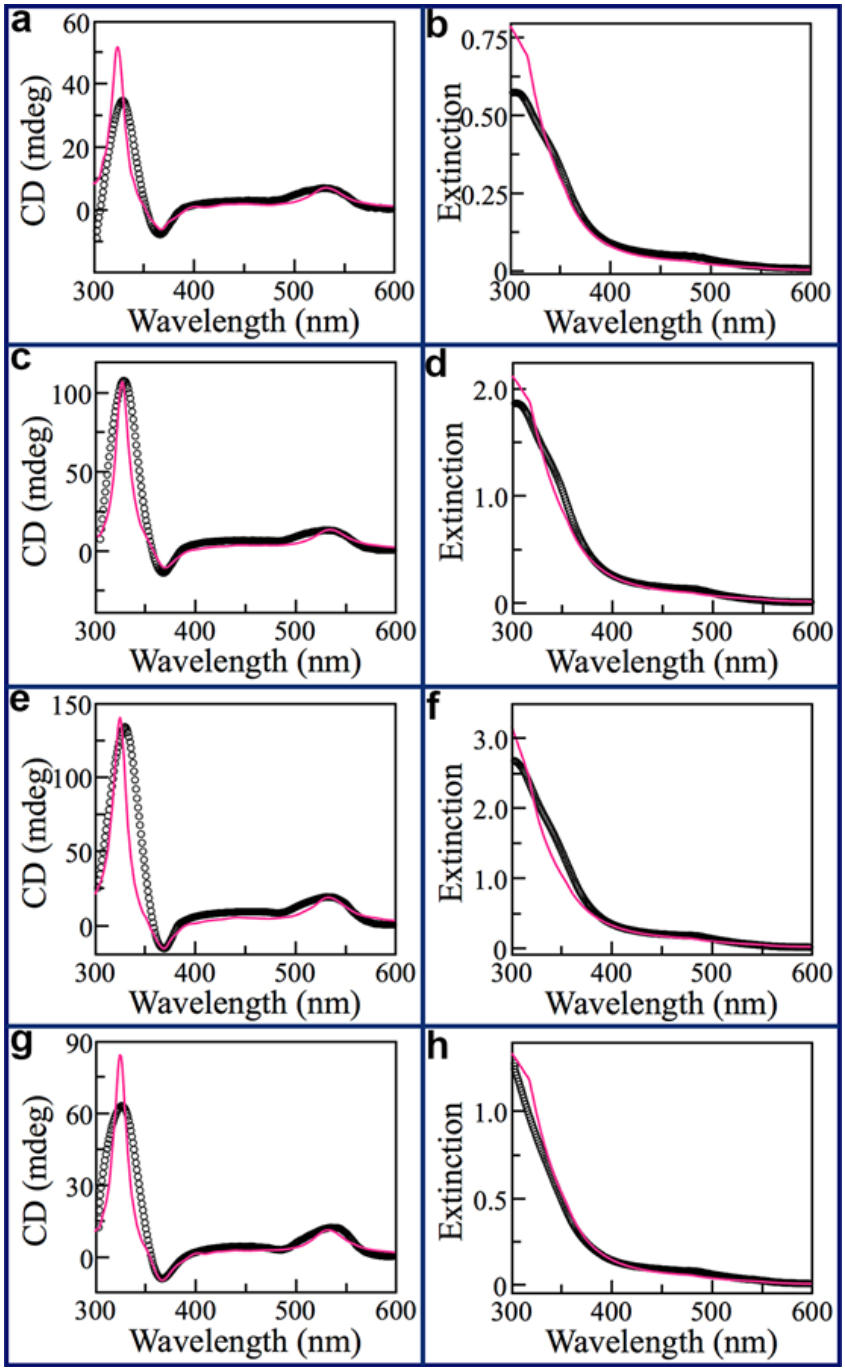

Figure 40. Comparison of experimental and computed CD and extinction spectra of $(+)_C$ HgS nanowires with different aspect ratios. (a, b), (c, d), (e, f) and (g, h), The CD and absorption spectra of α-HgS nanowires presented in Figure 27j-l (Nanowires 1), Figure 36a (Nanowires 2), Figure 36b (Nanowires 3), and Figure 36c (Nanowires 4), respectively. Black circles, experimental data. Pink curves, computed spectra.

Importantly, our synthetic scheme in Figure 26a allows the flexible combination of crystallographic and geometric handedness, which can offer rich tunability of the chiroptical response in well-defined inorganic nanostructures, mimicking enantiomers and diastereomers in organic matters. For example, Figure 38c and d present experimental and computed CD spectra, respectively, of four different combinations of crystallographic and geometric chirality in a twisted triangular bipyramid (with same averaged length of 85 nm): $(+)_C$-M, $(+)_C$-P, $(-)_C$-M, and $(-)_C$-P. We have chosen this medium- size HgS nanostructure as an example to highlight the unique opportunity to finely tailor the nanoscale chiroptical response through the structural engineering shown in Figure 26a. For this medium- size HgS nanostructure, the variation of chiral morphology mainly modulates the CD feature at shorter wavelengths. From the structural point of view, when comparing among these four epitaxially grown HgS nanostructures, only $(+)_C$-M / $(-)_C$-P and $(+)_C$-P / $(-)_C$-M represent two pairs of enantiomers that possess opposite handedness of both lattice and morphology, with a totally mirrored CD spectra, and the rest of the pairs are analogous to diastereomeric chiral molecules with non-mirrored CD characteristics. This observation again is consistent with the chiral effects of crystallographic lattice and geometric morphology elucidated in Figure 38a and b. This result highlights our unique synthetic capability to enable fine tailoring of the chiroptical response at the nanoscale as well as theoretical modeling for describing and predicting chiral phenomena in inorganic nanostructures. By combining a chiral lattice with a chiral morphology, the desired chiroptical response of inorganic nanostructures should be readily achieved.

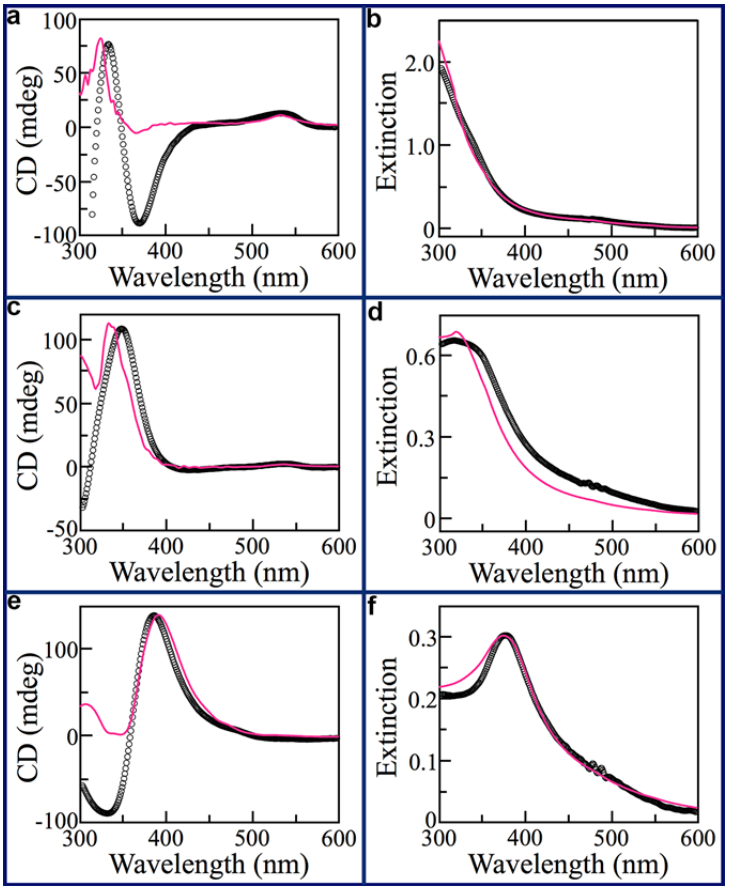

Figure 41. Comparison of experimental and computed CD and extinction spectra of $(+)_C$-M HgS nanoparticles possessing different size. (a, b), (c, d) and (e, f), 54 nm, 145 nm and 201 nm long, respectively. Black circles, experimental data. Pink curves, computed spectra.

5.5 Conclusion

To summarize, we have demonstrated mesoscopic achiral and chiral structures consisting of atomically chiral HgS nanocrystals. The novel material synthesis enables to substantially tune chiroptical responses and the electromagnetic simulation based on the general chiral model agrees well with the experimental results of differently shaped chiral NPs. This work paves the way for designing more complex nanostructures, such as heteostructures comprising metal NPs and chiral nanocrystal[84,85], or chiral

metamaterials[67,174]. Some other methods may also potentially create different kinds of chiral morphology based on chiral crystals, e.g. chiral templating by circularly polarized light[186]. This study also provides a new avenue to demonstrate intriguing new physics, such as lateral optical forces[187,188] and spin selectivity of electron transport[155,189], as well as insights in biochemistry and material science, including novel CD spectrascopy[190], crystallography of chiral materials[191], and asymmetric autocatalysis and chiral amplification[192]. Furthermore, α-HgS is a semiconductor with a bandgap in visible range, implying a potential applications in optoelectronics, some of which are chiral light emitters[193,194] and detectors[195].

Chapter 6: Summary and future research

This dissertation has proposed and developed new methods and results for solving problems in ultrafast optical generation and manipulation of nanoscale phonons, metamaterials for thermal management and cooperative chirality in inorganic nano-systems.

In Chapter 2, we have demonstrated how the phonon characteristics can be tailored through nanoscale interfacial coupling by investigating a well-designed acoustically mismatched core-shell hetero-nanostructures. Unambiguous experimental evidence of phononic coupling between the core and shell constituents through their interface has been achieved for the first time, unveiling unique phononic fingerprint of complex nanostructures. Additional importantly, these observed interfacially coupled phonon modes are optically excited by ultrafast pulses through the fundamental e-ph coupling mechanism, therefore, our materials engineering as well as optical technique further provides an opportunity to understand and even control such fundamental physical process. We have achieved monotonic control over the e-ph coupling constant by tuning configuration and constituent of core-shell nanostructures.

In Chapter 3, we have explored different time-domain pump-control-probe phonon manipulation schemes in both simulation and experiment with a good agreement. In particular, we have employed a Au-Ag core-shell nanoparticle with manifestation of multi-modal phonon vibrational modes as a model system for multimodal phonon manipulation, and demonstrated that simple addition of a femtosecond optical control pulse to an all optical pump-probe phonon measurement allows enhancement or

suppression of fundamental breathing phonon mode of nanoparticles, determined by time delay between the pump and control pulses. More advanced control of higher-order phonon modes and their interplay has also been achieved by utilizing two sequential independently tunable optical control pulses, allowing discriminatory modal manipulation of phonons for the first time. Precise tunability of condensed matter physical processes through nanoscale materials engineering and ultrafast manipulation not only offers fundamental insights into different physical properties of materials, but also facilitates design guideline for emerging phonon management and the next technological revolution with desirable functionality. All this work together represent a significant step towards a deep understanding of phonon-mediated physical and chemical processes as well as development of novel nanoscale materials with desirable functionality and property.

Based on this work, more flexible control scheme is achievable by more control pulses of independently controllable delays, intensities or wavelengths. The coherent control demonstrated here could also be extended to other types and forms of materials, although our high-quality sample enables the phonon multimode probing which is prerequisite for multimode manipulation[23,39,48]. Particularly, coherent manipulation in our work enables an all-optical technique to control or modulate the phononic multimodes at an ultrafast time scale. This provides more insight into fundamental research such as superlattice phononics[196] or phononic resonators[26,44,140], and more potential functionalities for future applications. For instance, ultrafast phonon spectroscopy researchers may find new ideas or solutions from our work since one may extract additional valuable information on the material of interest from multimode

probing and manipulation, which might not be accessible only by monitoring the fundamental mode. Besides, the few-nanometer size of the nanoparticles in our work can fit into an extremely small space as a nanophononic memory[197] or a photothermal heater[132], enabling a miniature phononic component/device or an ultrasensitive probe for a local environment, like in a biological cell[198]. Moreover, selectively harnessing distinct phonon modes in a complex nanostructure by ultrafast control schemes offers a new perspective to understand and even control diverse phonon-mediated physical processes, such as the coupling between acoustic phonons and excitons in quantum emitters[199]. This should provide novel materials design guideline to achieve desirable phonon property and functionality.

In Chapter 4, we have proposed and demonstrated patterned arrays as metamaterials for thermal management. First, we fabricated patterned micropillar arrays with DLW 3D printing. With FTIR spectroscopy and FDTD simulation, we have discovered the structural dependence of the arrays' characteristic resonance and emission properties. And the thermal imaging on the whole series of the patterns exhibits a clear emission tendency as a direct evidence of the structural dependence of thermal radiation, in accord to FTIR analysis. Further based on the idea, we numerically study the carbon-coated fiber arrays to simulate a simplified textile structure. We also find structural dependence of the arrays' characteristic resonance and the arrays' properties will not be significantly compromised even in less ideal configurations.

This study provides new views how we can take advantage of the structural parameters to control the thermal emission properties and potential passive cooling capability, which is interesting for textile applications to human body cooling. When

meta-fibers are arranged to form a yarn, environment-induced expansion or contraction of the yarn leads to regulation of the inter-fiber distance and thus tunable emissivity of the textile to better match the human body's thermal radiation. More specifically, when hot, the meta-fibers inside a yarn are brought closer together, shifting the yarn's emissivity to maximize spectrum overlap with that of the skin to enhance heat exchange. When cold, the yarn responds in a reversed manner to reduce heat dissipation. This bidirectional optical tunability can be designed to synergistically integrate other heat exchange mechanisms (convective, conductive, and evaporative) to allow effective local thermal management and protect body temperature from environmental changes. This kind of dynamic control of thermal emission may be achieved by functionalizing or embedding the fibers with environment-responsive (like thermos-responsive, humidity responsive or phase-changing) materials[151,200-202], which should be explored in future research. This study may lead to dynamically tunable thermal emitters or self-cooling devices.

In Chapter 5, both our experimental and theoretical results have demonstrated that the cooperative chiroptical properties of an inorganic nanostructure can be achieved through finely tailored interplay between crystallographic and geometric chirality. In particular, we have developed a solution phase synthetic scheme that allows the versatile combination of these two different types of handedness, leading to precise chirality engineering at the nanoscale. While various controls of inorganic nanostructures have been extensively studied and achieved, efficient control of chirality at the nanoscale is limited, therefore our current work represents a significant advance in the structural complexity and functionality of inorganic building blocks.

Our study opens up various research fronts, ranging from nature-mimicking chiral nanostructures to a wide range of enabled fundamental explorations and technology applications.

First, while we have employed cinnabar HgS combined with chiral *D*- and *L*-penicillamine molecules in epitaxial synthesis as an example to demonstrate our synthetic scheme and its sophisticated control of nanoscale cooperative chirality, our methodology illustrated in Figure 26a is versatile and should be readily extended to other inorganic chiral materials as well as interacting chiral molecules to allow more dynamic modulation of cooperative chirality. For example, there exist a series of chiral molecules that can effectively interact with metal ions, which might lead to different chiral morphologies with different twisting angles (Figure 25c).

Second, chiroptical properties of inorganic materials are particularly important because they are often associated with other phenomena, including spin-selective chemistry and interactions[189,203-205]. Therefore, the development of new types of inorganic nanostructures possessing unique and tunable crystallographic and geometric chirality might provide test beds for understanding and controlling spin-dependent or topological phenomena. Indeed, recent works on spin selection and spin transport through chiral biomolecules have led to additional insights[206-209].

Third, the colloidal chiral nanostructures achieved in the current work can be used as building blocks for hierarchical assembly of mesoscopic structures and devices. This might enable innovative chiral device concepts by using superchiral fields[210], and further open up alternative avenues to understand and control nanoscale

enantioselective interaction that is currently only observed for bio- and organic- chiral molecules, or to integrate other functional nanoparticles, such as plasmonic metal nanoparticles, to enable potential fundamental coupling and synergistic functionality[211,212]. Last but not least, our theoretical model represents a significant theoretical effort to integrate contributions of both crystallographic chirality and geometric chirality of an inorganic nanostructure. The excellent agreement between experimental and theoretical results in our current work not only validates our chiral modeling of inorganic nanostructures but also offer important design guidelines for nanostructures with desired chiroptical properties.

Bibliography

1 Humphreys, J., Beanland, R. & Goodhew, P. J. *Electron microscopy and analysis*. (CRC Press, 2014).

2 Binnig, G. & Rohrer, H. Scanning tunneling microscopy. *Surface Science* **126**, 236-244 (1983).

3 Binnig, G., Quate, C. F. & Gerber, C. Atomic force microscope. *Physical Review Letters* **56**, 930 (1986).

4 Kroto, H. W., Heath, J. R., O'Brien, S. C., Curl, R. F. & Smalley, R. E. C60: Buckminsterfullerene. *Nature* **318**, 162, doi:10.1038/318162a0 (1985).

5 Iijima, S. Helical microtubules of graphitic carbon. *Nature* **354**, 56, doi:10.1038/354056a0 (1991).

6 Novotny, L. & Hecht, B. *Principles of Nano-optics*. (Cambridge University Press, 2012).

7 Halas, N. J., Lal, S., Chang, W.-S., Link, S. & Nordlander, P. Plasmons in strongly coupled metallic nanostructures. *Chemical Reviews* **111**, 3913-3961 (2011).

8 Maier, S. A. *Plasmonics: fundamentals and applications*. (Springer, 2007).

9 Schuller, J. A. *et al.* Plasmonics for extreme light concentration and manipulation. *Nature Materials* **9**, 193 (2010).

10 Li, N. *et al.* Colloquium: Phononics: Manipulating heat flow with electronic analogs and beyond. *Reviews of Modern Physics* **84**, 1045-1066 (2012).

11 Stroscio, M. A. & Dutta, M. *Phonons in nanostructures*. (Cambridge University Press, 2001).

12 Cahill, D. G. *et al.* Nanoscale thermal transport. II. 2003–2012. *Applied Physics Reviews* **1**, 011305 (2014).

13 Balandin, A. A. & Nika, D. L. Phononics in low-dimensional materials. *Materials Today* **15**, 266-275 (2012).

14 Maldovan, M. Sound and heat revolutions in phononics. *Nature* **503**, 209-217, doi:10.1038/nature12608 (2013).

15 Del Fatti, N., Voisin, C., Chevy, F., Vallee, F. & Flytzanis, C. Coherent acoustic mode oscillation and damping in silver nanoparticles. *The Journal of Chemical Physics* **110**, 11484-11487 (1999).

16 Hodak, J. H., Henglein, A. & Hartland, G. V. Size dependent properties of Au particles: Coherent excitation and dephasing of acoustic vibrational modes. *The Journal of Chemical Physics* **111**, 8613-8621 (1999).

17 Voisin, C., Del Fatti, N., Christofilos, D. & Vallee, F. Ultrafast Electron Dynamics and Optical Nonlinearities in Metal Nanoparticles. *J. Phys. Chem. B* **105**, 2264-2280 (2001).

18 Voisin, C., Christofilos, D., Del Fatti, N. & Vallée, F. Environment effect on the acoustic vibration of metal nanoparticles. *Physica B: Condensed Matter* **316–317**, 89-94 (2002).

19 van Dijk, M. A., Lippitz, M. & Orrit, M. Detection of Acoustic Oscillations of Single Gold Nanospheres by Time-Resolved Interferometry. *Physical Review Letters* **95**, 267406 (2005).

20 Arbouet, A., Del Fatti, N. & Vallee, F. Optical control of the coherent acoustic vibration of metal nanoparticles. *J Chem Phys* **124**, 144701, doi:10.1063/1.2185631 (2006).
21 Dainese, P. *et al.* Stimulated Brillouin scattering from multi-GHz-guided acoustic phonons in nanostructured photonic crystal fibres. *Nature Physics* **2**, 388-392 (2006).
22 Hartland, G. V. Coherent excitation of vibrational modes in metallic nanoparticles. *Annual Review of Physical Chemistry* **57**, 403-430, doi:doi:10.1146/annurev.physchem.57.032905.104533 (2006).
23 Tang, Y. & Ouyang, M. Tailoring properties and functionalities of metal nanoparticles through crystallinity engineering. *Nat Mater* **6**, 754-759, doi:10.1038/nmat1982 (2007).
24 Portales, H. *et al.* Probing atomic ordering and multiple twinning in metal nanocrystals through their vibrations. *Proceedings of the National Academy of Sciences* **105**, 14784-14789, doi:10.1073/pnas.0803748105 (2008).
25 Crut, A., Maioli, P., Fatti, N. D. & Vallee, F. Anisotropy effects on the time-resolved spectroscopy of the acoustic vibrations of nanoobjects. *Physical Chemistry Chemical Physics* **11**, 5882-5888 (2009).
26 Pelton, M. *et al.* Damping of acoustic vibrations in gold nanoparticles. *Nature Nanotechnology* **4**, 492-495 (2009).
27 Juvé, V. *et al.* Probing Elasticity at the Nanoscale: Terahertz Acoustic Vibration of Small Metal Nanoparticles. *Nano Letters* **10**, 1853-1858, doi:10.1021/nl100604r (2010).
28 Tchebotareva, A. L., Ruijgrok, P. V., Zijlstra, P. & Orrit, M. Probing the acoustic vibrations of single metal nanoparticles by ultrashort laser pulses. *Laser & Photonics Reviews* **4**, 581-597 (2010).
29 Clark, J. N. *et al.* Ultrafast Three-Dimensional Imaging of Lattice Dynamics in Individual Gold Nanocrystals. *Science* **341**, 56-59, doi:10.1126/science.1236034 (2013).
30 O'Brien, P. J. *et al.* Bonding-induced thermal conductance enhancement at inorganic heterointerfaces using nanomolecular monolayers. *Nature Materials* **12**, 118-122 (2013).
31 Losego, M. D., Grady, M. E., Sottos, N. R., Cahill, D. G. & Braun, P. V. Effects of chemical bonding on heat transport across interfaces. *Nature Materials* **11**, 502-506 (2012).
32 Yang, J. *et al.* Enhanced and switchable nanoscale thermal conduction due to van der Waals interfaces. *Nature Nanotechnology* **7**, 91-95 (2012).
33 Msall, M., Dietsche, W., Friedland, K. J. & Tong, Q. Y. Images of the phonon propagation across twist-bonded crystals. *Physical Review Letters* **85**, 598 (2000).
34 Balandin, A. A. Nanophononics: Phonon Engineering in Nanostructures and Nanodevices. *Journal of Nanoscience and Nanotechnology* **5**, 1015-1022, doi:10.1166/jnn.2005.175 (2005).
35 Li, J. J. *et al.* Large-scale synthesis of nearly monodisperse CdSe/CdS core/shell nanocrystals using air-stable reagents via successive ion layer

adsorption and reaction. *Journal of the American Chemical Society* **125**, 12567 (2003).

36 Ithurria, S. & Talapin, D. V. Colloidal atomic layer deposition (c-ALD) using self-limiting reactions at nanocrystal surface coupled to phase transfer between polar and nonpolar media. *Journal of the American Chemical Society* **134**, 18585 (2012).

37 Weng, L., Zhang, H., Govorov, A. O. & Ouyang, M. Hierarchical synthesis of non-centrosymmetric hybrid nanostructures and enabled plasmon-driven photocatalysis. *Nat Commun* **5**, 4792, doi:10.1038/ncomms5792 (2014).

38 Zhang, J., Tang, Y., Lee, K. & Ouyang, M. Nonepitaxial growth of hybrid core-shell nanostructures with large lattice mismatches. *Science* **327**, 1634-1638, doi:10.1126/science.1184769 (2010).

39 Zhang, J., Tang, Y., Weng, L. & Ouyang, M. Versatile Strategy for Precisely Tailored Core@Shell Nanostructures with Single Shell Layer Accuracy: The Case of Metallic Shell. *Nano Lett* **9**, 4061-4065 (2009).

40 Bachelard, N. *et al.* Emergence of an enslaved phononic bandgap in a non-equilibrium pseudo-crystal. *Nature Materials* **16**, 808 (2017).

41 Beaud, P. *et al.* A time-dependent order parameter for ultrafast photoinduced phase transitions. *Nature Materials* **13**, 923-927 (2014).

42 Hoogeboom-Pot, K. M. *et al.* A new regime of nanoscale thermal transport: Collective diffusion increases dissipation efficiency. *Proceedings of the National Academy of Sciences* **112**, 4846-4851, doi:10.1073/pnas.1503449112 (2015).

43 Wall, S. *et al.* Ultrafast changes in lattice symmetry probed by coherent phonons. *Nat Commun* **3**, 721 (2012).

44 Okamoto, H. *et al.* Coherent phonon manipulation in coupled mechanical resonators. *Nature Physics* **9**, 480-484 (2013).

45 Benyamini, A., Hamo, A., Kusminskiy, S. V., von Oppen, F. & Ilani, S. Real-space tailoring of the electron-phonon coupling in ultraclean nanotube mechanical resonators. *Nature Physics* **10**, 151-156 (2014).

46 Chang, C., Okawa, D., Majumdar, A. & Zettl, A. Solid-state thermal rectifier. *Science* **314**, 1121-1124 (2006).

47 Crut, A., Maioli, P., Del Fatti, N. & Vallée, F. Acoustic vibrations of metal nano-objects: Time-domain investigations. *Physics Reports* **549**, 1-49 (2015).

48 Yu, S., Zhang, J., Tang, Y. & Ouyang, M. Engineering Acoustic Phonons and Electron–Phonon Coupling by the Nanoscale Interface. *Nano Letters* **15**, 6282-6288, doi:10.1021/acs.nanolett.5b03227 (2015).

49 Soukoulis, C. M. & Wegener, M. Past achievements and future challenges in the development of three-dimensional photonic metamaterials. *Nature Photonics* **5**, 523-530, doi:10.1038/nphoton.2011.154 (2011).

50 Zheludev, N. I. & Kivshar, Y. S. From metamaterials to metadevices. *Nature Materials* **11**, 917-924, doi:10.1038/nmat3431 (2012).

51 Khorasaninejad, M. *et al.* Metalenses at visible wavelengths: Diffraction-limited focusing and subwavelength resolution imaging. *Science* **352**, 1190-1194 (2016).

52 Nicolaou, Z. G. & Motter, A. E. Mechanical metamaterials with negative compressibility transitions. *Nature Materials* **11**, 608 (2012).
53 Ni, X., Wong, Z. J., Mrejen, M., Wang, Y. & Zhang, X. An ultrathin invisibility skin cloak for visible light. *Science* **349**, 1310-1314 (2015).
54 Hsu, P.-C. *et al.* Radiative human body cooling by nanoporous polyethylene textile. *Science* **353**, 1019-1023 (2016).
55 Raman, A. P., Anoma, M. A., Zhu, L., Rephaeli, E. & Fan, S. Passive radiative cooling below ambient air temperature under direct sunlight. *Nature* **515**, 540-544, doi:10.1038/nature13883 (2014).
56 Shi, N. N. *et al.* Keeping cool: Enhanced optical reflection and radiative heat dissipation in Saharan silver ants. *Science* **349**, 298-301, doi:10.1126/science.aab3564 (2015).
57 Zhai, Y. *et al.* Scalable-manufactured randomized glass-polymer hybrid metamaterial for daytime radiative cooling. *Science* **355**, 1062-1066, doi:10.1126/science.aai7899 (2017).
58 Liu, X. *et al.* Taming the blackbody with infrared metamaterials as selective thermal emitters. *Physical Review Letters* **107**, 045901-045901, doi:10.1103/PhysRevLett.107.045901 (2011).
59 Hossain, M. M., Jia, B. & Gu, M. A Metamaterial Emitter for Highly Efficient Radiative Cooling. *Advanced Optical Materials* **3**, 1047-1051, doi:10.1002/adom.201500119 (2015).
60 Liu, X. & Padilla, W. J. Reconfigurable room temperature metamaterial infrared emitter. *Optica* **4**, 430-433, doi:10.1364/OPTICA.4.000430 (2017).
61 Guerrero-Martínez, A., Alonso-Gómez, J. L., Auguié, B., Cid, M. M. & Liz-Marzán, L. M. From individual to collective chirality in metal nanoparticles. *Nano Today* **6**, 381-400, doi:10.1016/j.nantod.2011.06.003 (2011).
62 Milton, F. P., Govan, J., Mukhina, M. V. & Gun'ko, Y. K. The chiral nano-world: chiroptically active quantum nanostructures. *Nanoscale Horizons* **1**, 14-26, doi:10.1039/C5NH00072F (2016).
63 Wang, Y., Xu, J., Wang, Y. & Chen, H. Emerging chirality in nanoscience. *Chemical Society Reviews* **42**, 2930-2962, doi:10.1039/c2cs35332f (2013).
64 Xia, Y., Zhou, Y. & Tang, Z. Chiral inorganic nanoparticles : origin, optical properties and bioapplications. *Nanoscale* **3**, 1374-1382, doi:10.1039/C0NR00903B (2011).
65 Ben-Moshe, A., Maoz, B. M., Govorov, A. O. & Markovich, G. Chirality and chiroptical effects in inorganic nanocrystal systems with plasmon and exciton resonances. *Chemical Society reviews* **42**, 7028-7041, doi:10.1039/c3cs60139k (2013).
66 Govorov, A. O. *et al.* Chiral nanoparticle assemblies: circular dichroism, plasmonic interactions, and exciton effects. *Journal of Materials Chemistry* **21**, 16806-16818, doi:10.1039/C1JM12345A (2011).
67 Valev, V. K., Baumberg, J. J., Sibilia, C. & Verbiest, T. Chirality and chiroptical effects in plasmonic nanostructures: fundamentals, recent progress, and outlook. *Advanced Materials* **25**, 2517-2534, doi:10.1002/adma.201205178 (2013).

68 Berova, N., Polavarapu, P. L., Nakanishi, K. & Woody, R. W. *Comprehensive chiroptical spectroscopy*. (John Wiley & Sons, 2012).
69 Li, Z. *et al.* Reversible plasmonic circular dichroism of Au nanorod and DNA assemblies. *Journal of the American Chemical Society* **134**, 3322-3325 (2012).
70 Moloney, M. P., Gun'ko, Y. K. & Kelly, J. M. Chiral highly luminescent CdS quantum dots. *Chemical Communications*, 3900-3902 (2007).
71 Nakashima, T., Kobayashi, Y. & Kawai, T. Optical activity and chiral memory of thiol-capped CdTe nanocrystals. *Journal of the American Chemical Society* **131**, 10342-10343 (2009).
72 Slocik, J. M., Govorov, A. O. & Naik, R. R. Plasmonic circular dichroism of peptide-functionalized gold nanoparticles. *Nano letters* **11**, 701-705 (2011).
73 Tohgha, U. *et al.* Ligand induced circular dichroism and circularly polarized luminescence in CdSe quantum dots. *ACS Nano* **7**, 11094-11102 (2013).
74 Tohgha, U., Varga, K. & Balaz, M. Achiral CdSe quantum dots exhibit optical activity in the visible region upon post-synthetic ligand exchange with D-or L-cysteine. *Chemical Communications* **49**, 1844-1846 (2013).
75 Gansel, J. K. *et al.* Gold helix photonic metamaterial as broadband circular polarizer. *Science* **325**, 1513-1515 (2009).
76 Abdulrahman, N. A. *et al.* Induced Chirality through Electromagnetic Coupling between Chiral Molecular Layers and Plasmonic Nanostructures. *Nano Letters* **12**, 977-983, doi:10.1021/nl204055r (2012).
77 Schäferling, M., Dregely, D., Hentschel, M. & Giessen, H. Tailoring Enhanced Optical Chirality: Design Principles for Chiral Plasmonic Nanostructures. *Physical Review X* **2**, 031010-031010, doi:10.1103/PhysRevX.2.031010 (2012).
78 Zhu, Y. *et al.* Chiral Gold Nanowires with Boerdijk–Coxeter–Bernal Structure. *Journal of the American Chemical Society* **136**, 12746-12752 (2014).
79 Yan, W. *et al.* Self-Assembly of Chiral Nanoparticle Pyramids with Strong R/S Optical Activity. *Journal of the American Chemical Society* **134**, 15114-15121, doi:10.1021/ja3066336 (2012).
80 Schreiber, R. *et al.* Hierarchical assembly of metal nanoparticles, quantum dots and organic dyes using DNA origami scaffolds. *Nature Nanotechnology* **9**, 74-78, doi:10.1038/nnano.2013.253 (2014).
81 Kuzyk, A. *et al.* Reconfigurable 3D plasmonic metamolecules. *Nature Materials* **13**, 862-866, doi:10.1038/nmat4031 (2014).
82 Kuzyk, A. *et al.* DNA-based self-assembly of chiral plasmonic nanostructures with tailored optical response. *Nature* **483**, 311-314, doi:10.1038/nature10889 (2012).
83 Kim, Y. *et al.* Reconfigurable chiroptical nanocomposites with chirality transfer from the macro-to the nanoscale. *Nature Materials* **15**, 461 (2016).
84 Govorov, A. O., Fan, Z., Hernandez, P., Slocik, J. M. & Naik, R. R. Theory of Circular Dichroism of Nanomaterials Comprising Chiral Molecules and Nanocrystals: Plasmon Enhancement, Dipole Interactions, and Dielectric Effects. *Nano Letters* **10**, 1374-1382, doi:10.1021/nl100010v (2010).

85 Govorov, A. O. & Fan, Z. Theory of chiral plasmonic nanostructures comprising metal nanocrystals and chiral molecular media. *ChemPhysChem* **13**, 2551-2560, doi:10.1002/cphc.201100958 (2012).
86 Fan, Z. & Govorov, A. O. Chiral nanocrystals: plasmonic spectra and circular dichroism. *Nano letters* **12**, 3283-3289, doi:10.1073/pnas.0703993104 (2012).
87 Fan, Z. & Govorov, A. O. Plasmonic Circular Dichroism of Chiral Metal Nanoparticle Assemblies. *Nano Letters* **10**, 2580-2587, doi:10.1021/nl101231b (2010).
88 Boriskina, S. & Zheludev, N. I. *Singular and Chiral Nanoplasmonics*. (CRC Press, 2014).
89 Elliott, S. D., Moloney, M. c. l. P. & Gun'ko, Y. K. Chiral shells and achiral cores in CdS quantum dots. *Nano letters* **8**, 2452-2457 (2008).
90 Ben‐Moshe, A., Govorov, A. O. & Markovich, G. Enantioselective synthesis of intrinsically chiral mercury sulfide nanocrystals. *Angewandte Chemie International Edition* **52**, 1275-1279 (2013).
91 Mukhina, M. V. *et al.* Intrinsic Chirality of CdSe/ZnS Quantum Dots and Quantum Rods. *Nano Letters* **15**, 2844-2851, doi:10.1021/nl504439w (2015).
92 Liu, M., Zhang, L. & Wang, T. Supramolecular chirality in self-assembled systems. *Chemical Reviews* **115**, 7304-7397 (2015).
93 Decker, M., Zhao, R., Soukoulis, C., Linden, S. & Wegener, M. Twisted split-ring-resonator photonic metamaterial with huge optical activity. *Optics letters* **35**, 1593-1595 (2010).
94 Ben-Moshe, A. *et al.* Enantioselective control of lattice and shape chirality in inorganic nanostructures using chiral biomolecules. *Nature Communications* **5**, 4302 (2014).
95 Weiner, A. *Ultrafast optics*. Vol. 72 (John Wiley & Sons, 2011).
96 Kirilyuk, A., Kimel, A. V. & Rasing, T. Ultrafast optical manipulation of magnetic order. *Reviews of Modern Physics* **82**, 2731-2784 (2010).
97 Rossi, F. & Kuhn, T. Theory of ultrafast phenomena in photoexcited semiconductors. *Reviews of Modern Physics* **74**, 895-950 (2002).
98 Kumpulainen, T., Lang, B., Rosspeintner, A. & Vauthey, E. Ultrafast Elementary Photochemical Processes of Organic Molecules in Liquid Solution. *Chemical Reviews* **117**, 10826-10939, doi:10.1021/acs.chemrev.6b00491 (2017).
99 Berera, R., van Grondelle, R. & Kennis, J. T. Ultrafast transient absorption spectroscopy: principles and application to photosynthetic systems. *Photosynthesis Research* **101**, 105-118 (2009).
100 Zhang, Z., Piatkowski, L., Bakker, H. J. & Bonn, M. Ultrafast vibrational energy transfer at the water/air interface revealed by two-dimensional surface vibrational spectroscopy. *Nature Chemistry* **3**, 888 (2011).
101 Fischer, J. & Wegener, M. Three‐dimensional optical laser lithography beyond the diffraction limit. *Laser & Photonics Reviews* **7**, 22-44 (2013).
102 Rill, M. S. *et al.* Photonic metamaterials by direct laser writing and silver chemical vapour deposition. *Nature Materials* **7**, 543, doi:10.1038/nmat2197 (2008).

103 Schaedler, T. A. *et al.* Ultralight metallic microlattices. *Science* **334**, 962-965 (2011).
104 Jackson, J. D. *Classical Electrodynamics, 3rd Edition*. (John Wiley & Sons, 1998).
105 Jin, J.-M. *The finite element method in electromagnetics*. (John Wiley & Sons, 2015).
106 Taflove, A. & Hagness, S. C. *Computational electrodynamics: the finite-difference time-domain method*. (Artech House, 2005).
107 Zhao, J. *et al.* Methods for Describing the Electromagnetic Properties of Silver and Gold Nanoparticles. *Accounts of Chemical Research* **41**, 1710-1720, doi:10.1021/ar800028j (2008).
108 Gallinet, B., Butet, J. & Martin, O. J. Numerical methods for nanophotonics: standard problems and future challenges. *Laser & Photonics Reviews* **9**, 577-603 (2015).
109 Kutz, J. N. *Data-driven modeling & scientific computation: methods for complex systems & big data*. (Oxford University Press, 2013).
110 Yee, K. Numerical solution of initial boundary value problems involving Maxwell's equations in isotropic media. *IEEE Transactions on antennas and propagation* **14**, 302-307 (1966).
111 Yu, S.-J. & Ouyang, M. Coherent Discriminatory Modal Manipulation of Acoustic Phonons at the Nanoscale. *Nano Letters* **18**, 1124-1129, doi:10.1021/acs.nanolett.7b04662 (2018).
112 Wang, P.-p., Yu, S.-J., Govorov, A. O. & Ouyang, M. Cooperative expression of atomic chirality in inorganic nanostructures. *Nature Communications* **8**, 14312 (2017).
113 Li, D., Huxtable, S. T., Abramson, A. R. & Majumdar, A. Thermal Transport in Nanostructured Solid-State Cooling Devices. *Journal of Heat Transfer* **127**, 108, doi:10.1115/1.1839588 (2005).
114 Levy, M., Bass, H. & Stern, R. *Handbook of Elastic Properties of Solids, Liquids and Gases* (Academic Press, 2000).
115 Hodak, J. H., Henglein, A. & Hartland, G. V. Tuning the spectral and temporal response in PtAu core–shell nanoparticles. *The Journal of Chemical Physics* **114**, 2760-2765, doi:10.1063/1.1339266 (2001).
116 Lin, Z., Zhigilei, L. & Celli, V. Electron-phonon coupling and electron heat capacity of metals under conditions of strong electron-phonon nonequilibrium. *Physical Review B* **77**, doi:10.1103/PhysRevB.77.075133 (2008).
117 Hodak, J. H., Henglein, A. & Hartland, G. V. Coherent Excitation of Acoustic Breathing Modes in Bimetallic Core−Shell Nanoparticles. *The Journal of Physical Chemistry B* **104**, 5053-5055, doi:10.1021/jp000578v (2000).
118 Guillon, C. *et al.* Coherent Acoustic Vibration of Metal Nanoshells. *Nano Letters* **7**, 138-142, doi:10.1021/nl062380d (2007).
119 Wang, L., Kiya, A., Okuno, Y., Niidome, Y. & Tamai, N. Ultrafast spectroscopy and coherent acoustic phonons of Au–Ag core–shell nanorods. *The Journal of Chemical Physics* **134**, 054501 (2011).
120 Yu, K. *et al.* Probing Silver Deposition on Single Gold Nanorods by Their Acoustic Vibrations. *Nano Letters* **14**, 915-922, doi:10.1021/nl404304h (2014).

121 Stoll, T. *et al.* Ultrafast Acoustic Vibrations of Bimetallic Nanoparticles. *The Journal of Physical Chemistry C* **119**, 1591-1599, doi:10.1021/jp511070h (2015).
122 Mongin, D. *et al.* Acoustic Vibrations of Metal-Dielectric Core–Shell Nanoparticles. *Nano Letters* **11**, 3016-3021, doi:10.1021/nl201672k (2011).
123 Crut, A. *et al.* Vibrations of spherical core-shell nanoparticles. *Physical Review B* **83**, 205430 (2011).
124 Kirakosyan, A. S. & Shahbazyan, T. V. Vibrational modes of metal nanoshells and bimetallic core-shell nanoparticles. *The Journal of Chemical Physics* **129**, 034708-034707 (2008).
125 Nelet, A. *et al.* Acoustic vibrations of metal nanoparticles: high order radial mode detection. *Applied Surface Science* **226**, 209-215 (2004).
126 McCarthy, E. K., Bellew, A. T., Sader, J. E. & Boland, J. J. Poisson's ratio of individual metal nanowires. *Nature communications* **5**, 4336, doi:10.1038/ncomms5336 (2014).
127 Cherian, R., Gerard, C., Mahadevan, P., Cuong, N. T. & Maezono, R. Size dependence of the bulk modulus of semiconductor nanocrystals from first-principles calculations. *Physical Review B* **82**, 235321, doi:10.1103/PhysRevB.82.235321 (2010).
128 Buffat, P. & Borel, J. P. Size effect on the melting temperature of gold particles. *Physical Review A* **13**, 2287-2298 (1976).
129 Luan, B. & Robbins, M. O. The breakdown of continuum models for mechanical contacts. *Nature* **435**, 929-932 (2005).
130 Combe, N. & Saviot, L. Acoustic modes in metallic nanoparticles: Atomistic versus elasticity modeling. *Physical Review B* **80**, 035411 (2009).
131 Diels, J.-C. & Rudolph, W. *Ultrashort laser pulse phenomena*. (Academic Press, 2006).
132 West, J. L. & Halas, N. J. Engineered nanomaterials for biophotonics applications: improving sensing, imaging, and therapeutics. *Annual review of biomedical engineering* **5**, 285-292, doi:10.1146/annurev.bioeng.5.011303.120723 (2003).
133 Fuller, F. D. *et al.* Vibronic coherence in oxygenic photosynthesis. *Nature Chemistry* **6**, 706-711 (2014).
134 Tamayo, J., Kosaka, P. M., Ruz, J. J., San Paulo, Á. & Calleja, M. Biosensors based on nanomechanical systems. *Chemical Society Reviews* **42**, 1287-1311 (2013).
135 Tang, Y., Goncharov, A. F., Struzhkin, V. V., Hemley, R. J. & Ouyang, M. Spin of Semiconductor Quantum Dots under Hydrostatic Pressure. *Nano Letters* **10**, 358-362, doi:10.1021/nl9037399 (2010).
136 Li, Y. *et al.* Interplay of bias-driven charging and the vibrational stark effect in molecular junctions. *Nano letters* **16**, 1104-1109 (2016).
137 Frimmer, M., Gieseler, J. & Novotny, L. Cooling mechanical oscillators by coherent control. *Physical review letters* **117**, 163601 (2016).
138 Yampolsky, S. *et al.* Seeing a single molecule vibrate through time-resolved coherent anti-Stokes Raman scattering. *Nature Photonics* **8**, 650-656 (2014).

139 Ahmed, A., Pelton, M. & Guest, J. R. Understanding How Acoustic Vibrations Modulate the Optical Response of Plasmonic Metal Nanoparticles. *ACS Nano* **11**, 9360-9369, doi:10.1021/acsnano.7b04789 (2017).
140 O'Brien, K. *et al.* Ultrafast acousto-plasmonic control and sensing in complex nanostructures. *Nature Communications* **5**, 4042 (2014).
141 Hartland, G. V. Optical Studies of Dynamics in Noble Metal Nanostructures. *Chemical Reviews* **111**, 3858-3887, doi:10.1021/cr1002547 (2011).
142 Kim, J.-W., Vomir, M. & Bigot, J.-Y. Controlling the spins angular momentum in ferromagnets with sequences of picosecond acoustic pulses. *Scientific reports* **5** (2015).
143 Cammarata, M. *et al.* Sequential Activation of Molecular Breathing and Bending during Spin-Crossover Photoswitching Revealed by Femtosecond Optical and X-Ray Absorption Spectroscopy. *Physical Review Letters* **113**, 227402 (2014).
144 Borri, P. *et al.* Exciton dephasing via phonon interactions in InAs quantum dots: Dependence on quantum confinement. *Physical Review B* **71**, 115328 (2005).
145 Shah, J. *Ultrafast spectroscopy of semiconductors and semiconductor nanostructures*. Vol. 115 (Springer, 1999).
146 Law, T. *The Future of Thermal Comfort in an Energy-Constrained World*. (Springer Science & Business Media, 2013).
147 Hossain, M. & Gu, M. Radiative cooling: Principles, progress, and potentials. *Advanced Science* **3** (2016).
148 Hu, J., Meng, H., Li, G. & Ibekwe, S. I. A review of stimuli-responsive polymers for smart textile applications. *Smart Materials and Structures* **21**, 053001 (2012).
149 Hagemann, H. J., Gudat, W. & Kunz, C. Optical constants from the far infrared to the x-ray region: Mg, Al, Cu, Ag, Au, Bi, C, and Al2O3. *J. Opt. Soc. Am.* **65**, 742-744, doi:10.1364/JOSA.65.000742 (1975).
150 Olmon, R. L. *et al.* Optical dielectric function of gold. *Physical Review B* **86**, 235147 (2012).
151 Jafar-Zanjani, S., Salary, M. M. & Mosallaei, H. Metafabrics for Thermoregulation and Energy-Harvesting Applications. *ACS Photonics* **4**, 915-927, doi:10.1021/acsphotonics.6b01005 (2017).
152 Tong, J. K. *et al.* Infrared-Transparent Visible-Opaque Fabrics for Wearable Personal Thermal Management. *ACS Photonics* **2**, 769-778, doi:10.1021/acsphotonics.5b00140 (2015).
153 Amabilino, D. B. *Chirality at the nanoscale: nanoparticles, surfaces, materials and more*. (John Wiley & Sons, 2009).
154 Wagnière, G. H. *On chirality and the universal asymmetry: reflections on image and mirror image*. (John Wiley & Sons, 2008).
155 Naaman, R. & Waldeck, D. H. Spintronics and Chirality: Spin Selectivity in Electron Transport Through Chiral Molecules. *Annual Review of Physical Chemistry* **66**, 263-281, doi:10.1146/annurev-physchem-040214-121554 (2015).
156 Barron, L. D. *Biochirality: Origins, Evolution and Molecular Recognition*. (Springer, 2013).

157 Nandi, N. *Chirality in biological nanospaces: reactions in active sites*. (CRC Press, 2011).
158 Nandi, N. Chiral discrimination in the confined environment of biological nanospace: reactions and interactions involving amino acids and peptides. *International Reviews in Physical Chemistry* **28**, 111-167 (2009).
159 Baletto, F. & Ferrando, R. Structural properties of nanoclusters: Energetic, thermodynamic, and kinetic effects. *Reviews of Modern Physics* **77**, 371 (2005).
160 Nomura, K. Optical activity in tellurium. *Physical Review Letters* **5**, 500 (1960).
161 Glazer, A. & Stadnicka, K. On the origin of optical activity in crystal structures. *Journal of Applied Crystallography* **19**, 108-122 (1986).
162 Flack, H. D. Chiral and achiral crystal structures. *Helvetica Chimica Acta* **86**, 905-921 (2003).
163 Ben-Moshe, A., Maoz, B. M., Govorov, A. O. & Markovich, G. Chirality and chiroptical effects in inorganic nanocrystal systems with plasmon and exciton resonances. *Chemical Society Reviews* **42**, 7028-7041 (2013).
164 Wang, Y., Xu, J., Wang, Y. & Chen, H. Emerging chirality in nanoscience. *Chemical Society Reviews* **42**, 2930-2962 (2013).
165 Aurivillius, K. L. On the crystal structure of cinnabar. . *Acta Chemica Scandinavica* **4**, 1413–1436 (1950).
166 Kuzyk, A. *et al.* DNA-based self-assembly of chiral plasmonic nanostructures with tailored optical response. *Nature* **483**, 311 (2012).
167 Yan, W. *et al.* Self-assembly of chiral nanoparticle pyramids with strong R/S optical activity. *Journal of the American Chemical Society* **134**, 15114-15121 (2012).
168 Schreiber, R. *et al.* Hierarchical assembly of metal nanoparticles, quantum dots and organic dyes using DNA origami scaffolds. *Nature Nanotechnology* **9**, 74 (2014).
169 Li, J. J. *et al.* Large-scale synthesis of nearly monodisperse CdSe/CdS core/shell nanocrystals using air-stable reagents via successive ion layer adsorption and reaction. *Journal of the American Chemical Society* **125**, 12567-12575 (2003).
170 Milton, F. P., Govan, J., Mukhina, M. V. & Gun'ko, Y. K. The chiral nano-world: Chiroptically active quantum nanostructures. *Nanoscale Horizons* **1**, 14-26 (2016).
171 Guerrero-Martínez, A., Alonso-Gómez, J. L., Auguié, B., Cid, M. M. & Liz-Marzán, L. M. From individual to collective chirality in metal nanoparticles. *Nano Today* **6**, 381-400 (2011).
172 Govorov, A. O. *et al.* Chiral nanoparticle assemblies: circular dichroism, plasmonic interactions, and exciton effects. *Journal of Materials Chemistry* **21**, 16806-16818 (2011).
173 Valev, V. *et al.* Plasmonic ratchet wheels: switching circular dichroism by arranging chiral nanostructures. *Nano letters* **9**, 3945-3948 (2009).
174 Wang, B., Zhou, J., Koschny, T., Kafesaki, M. & Soukoulis, C. M. Chiral metamaterials: simulations and experiments. *Journal of Optics A Pure & Applied Optics* **11**, 114003 (2009).

175 Lekner, J. Optical properties of isotropic chiral media. *Pure and Applied Optics: Journal of the European Optical Society Part A* **5**, 417-443, doi:10.1088/0963-9659/5/4/008 (1996).
176 Ougier, S., Chenerie, I., Sihvola, A. & Priou, A. Propagation in bi-isotropic media: effect of different formalisms on the propagation analysis. *Progress In Electromagnetics Research* **9**, 19-30 (1994).
177 Ben-Moshe, A. *et al.* Enantioselective control of lattice and shape chirality in inorganic nanostructures using chiral biomolecules. *Nature Communications* **5**, 4302-4302, doi:10.1038/ncomms5302 (2014).
178 Bohren, C. F. & Huffman, D. R. *Absorption and Scattering of Light by Small Particles*. (Wiley-VCH, 2004).
179 Ben-Moshe, A., Govorov, A. O. & Markovich, G. Enantioselective synthesis of intrinsically chiral mercury sulfide nanocrystals. *Angewandte Chemie - International Edition* **52**, 1275-1279, doi:10.1002/anie.201207489 (2013).
180 Jellison Jr, G. E. & Modine, F. A. Parameterization of the optical functions of amorphous materials in the interband region. *Appl. Phys. Lett.* **69**, 371-373 (1996).
181 Ferlauto, A. S. *et al.* Analytical model for the optical functions of amorphous semi-conductors from the near-infrared to ultraviolet: Applications in thin film photo-voltaics. *J. Appl. Phys.* **92**, 2424-2436 (2002).
182 Fujiwara, H. *Spectroscopic Ellipsometry: Principles And Applications*. (John Wiley & Sons, 2007).
183 Cardona, M. *et al.* Electronic and phononic properties of cinnabar: Ab initio calculations and some experimental results. *Phys. Rev. B* **82**, 085210 (2010).
184 Meistermann, I. *et al.* Intramolecular DNA coiling mediated by metallo-supramolecular cylinders: differential binding of P and M helical enantiomers. *Proceedings of the National Academy of Sciences* **99**, 5069-5074 (2002).
185 Schulz, G. E. & Schirmer, R. H. *Principles of protein structure*. (Springer, 1979).
186 Yeom, J. *et al.* Chiral templating of self-assembling nanostructures by circularly polarized light. *Nature Materials* **14**, 66-72, doi:10.1038/nmat4125 (2014).
187 Hayat, A., Mueller, J. B. & Capasso, F. Lateral chirality-sorting optical forces. *Proceedings of the National Academy of Sciences* **112**, 13190-13194 (2015).
188 Wang, S. B. & Chan, C. T. Lateral optical force on chiral particles near a surface. *Nature Communications* **5**, 3307 (2014).
189 Göhler, B. *et al.* Spin selectivity in electron transmission through self-assembled monolayers of double-stranded DNA. *Science* **331**, 894-897 (2011).
190 García-Etxarri, A. & Dionne, J. A. Surface-enhanced circular dichroism spectroscopy mediated by nonchiral nanoantennas. *Physical Review B* **87**, 235409 (2013).
191 Weissbuch, I. & Lahav, M. Crystalline architectures as templates of relevance to the origins of homochirality. *Chemical Reviews* **111**, 3236-3267, doi:10.1021/cr1002479 (2011).

192 Shindo, H. *et al.* Asymmetric autocatalysis induced by cinnabar: observation of the enantioselective adsorption of a 5‐pyrimidyl alkanol on the crystal surface. *Angewandte Chemie International Edition* **52**, 9135-9138 (2013).
193 Konishi, K. *et al.* Circularly Polarized Light Emission from Semiconductor Planar Chiral Nanostructures. *Physical Review Letters* **106**, 057402 (2011).
194 Zhang, Y., Oka, T., Suzuki, R., Ye, J. & Iwasa, Y. Electrically switchable chiral light-emitting transistor. *Science* **344**, 725-728 (2014).
195 Li, W. *et al.* Circularly polarized light detection with hot electrons in chiral plasmonic metamaterials. *Nature Communications* **6**, 8379 (2015).
196 Luckyanova, M. N. *et al.* Coherent Phonon Heat Conduction in Superlattices. *Science* **338**, 936-939, doi:10.1126/science.1225549 (2012).
197 Lanzillotti-Kimura, N. D., Fainstein, A., Lemaitre, A., Jusserand, B. & Perrin, B. Coherent control of sub-terahertz confined acoustic nanowaves: Theory and experiments. *Physical Review B* **84**, 115453 (2011).
198 Kneipp, K. *et al.* Surface-Enhanced Raman Spectroscopy in Single Living Cells Using Gold Nanoparticles. *Appl. Spectrosc.* **56**, 150-154 (2002).
199 Werschler, F. *et al.* Coupling of excitons and discrete acoustic phonons in vibrationally isolated quantum emitters. *Nano letters* **16**, 5861-5865 (2016).
200 Du, K.-K. *et al.* Control over emissivity of zero-static-power thermal emitters based on phase-changing material GST. *Light: Science & Applications* **6**, e16194 (2017).
201 Liu, X. & Padilla Willie, J. Thermochromic Infrared Metamaterials. *Advanced Materials* **28**, 871-875, doi:10.1002/adma.201504525 (2016).
202 Liu, X. & Padilla, W. J. Reconfigurable room temperature metamaterial infrared emitter. *Optica* **4**, 430-433, doi:10.1364/OPTICA.4.000430 (2017).
203 Ray, K., Ananthavel, S., Waldeck, D. & Naaman, R. Asymmetric scattering of polarized electrons by organized organic films of chiral molecules. *Science* **283**, 814-816 (1999).
204 Vager, D. & Vager, Z. Spin order without magnetism–a new phase of spontaneously broken symmetry in condensed matter. *Physics Letters A* **376**, 1895-1897 (2012).
205 Guo, A.-M. & Sun, Q.-f. Spin-selective transport of electrons in DNA double helix. *Physical Review Letters* **108**, 218102 (2012).
206 Dor, O. B., Yochelis, S., Mathew, S. P., Naaman, R. & Paltiel, Y. A chiral-based magnetic memory device without a permanent magnet. *Nature Communications* **4**, 2256 (2013).
207 Scheer, E. Visions for a molecular future. *Nature Nanotechnology* **8**, 386 (2013).
208 Einati, H., Mishra, D., Friedman, N., Sheves, M. & Naaman, R. Light-controlled spin filtering in bacteriorhodopsin. *Nano Letters* **15**, 1052-1056 (2015).
209 Migliore, A., Naaman, R. & Beratan, D. N. Sensing of molecules using quantum dynamics. *Proceedings of the National Academy of Sciences* **112**, E2419-E2428 (2015).
210 Hendry, E. *et al.* Ultrasensitive detection and characterization of biomolecules using superchiral fields. *Nature Nanotechnology* **5**, 783 (2010).

211 Yoon, T. P. & Jacobsen, E. N. Privileged chiral catalysts. *Science* **299**, 1691-1693 (2003).
212 Rosenberg, R. A., Mishra, D. & Naaman, R. Chiral selective chemistry induced by natural selection of spin-polarized electrons. *Angewandte Chemie International Edition* **54**, 7295-7298 (2015).